Lawrence Berkeley National Laboratory
Recent Work

Title

Hydrologic Characterization of Fractured Rocks - An Interdisciplinary Methodology

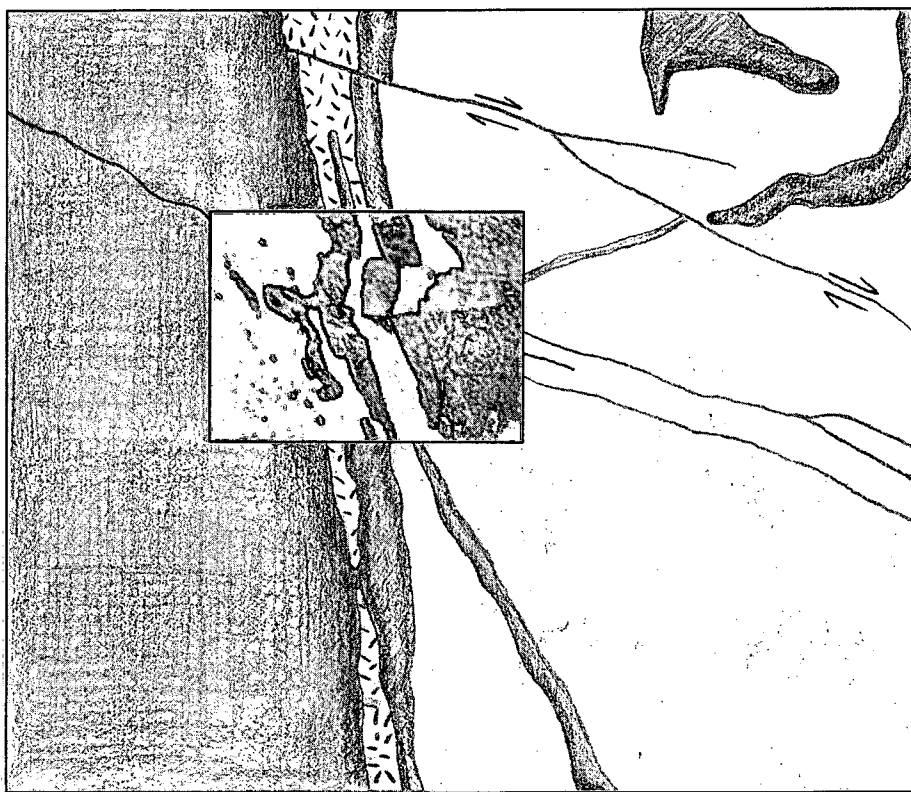**Permalink**

Authors

Long, J.C.S.
Majer, E.L.
Martel, S.J.
et al.

Publication Date

1990-11-01

NAGRA -DOE
COOPERATIVE
PROJECT REPORT

Hydrologic Characterization of Fractured Rocks—An Interdisciplinary Methodology

Jane C. S. Long, Ernest L. Majer, Stephen J. Martel, Kenzi Karasaki, John E. Peterson Jr., Amy Davey, and Kevin Hestir

November 1990

Swiss National Cooperative for
the Storage of Nuclear Waste
NAGRA
CH-5401 Baden, Switzerland

Earth Sciences Division
Lawrence Berkeley Laboratory
University of California
Berkeley, California 94720, USA

DISCLAIMER

Hydrologic Characterization of Fractured Rocks—

An Interdisciplinary Methodology

Jane C.S. Long, Ernest L. Majer, Stephen J. Martel, Kenzi Karasaki,
John E. Peterson Jr., Amy Davey, and Kevin Hestir

Earth Sciences Division
Lawrence Berkeley Laboratory
University of California
Berkeley, California 94720

November 1990

Preface

This report is one of a series documenting the results of the Nagra-DOE Cooperative (NDC-I) research program in which the cooperating scientists explore the geological, geophysical, hydrological, geochemical, and structural effects anticipated from the use of a rock mass as a geologic repository for nuclear waste. This program was sponsored by the U. S. Department of Energy (DOE) through the Lawrence Berkeley Laboratory (LBL) and the Swiss Nationale Genossenschaft für die Lagerung radioaktiver Abfälla (Nagra) and concluded in September 1989. The principal investigators are Jane C. S. Long, Ernest L. Majer, Karsten Pruess, Kenzi Karasaki, Chalon Carnahan and Chin-Fu Tsang for LBL and Piet Zuidema, Peter Blümling, Peter Hufschmied and Stratis Vomvoris for Nagra. Other participants will appear as authors of the individual reports. Technical reports in this series are listed below.

1. Determination of Fracture Inflow Parameters with a Borehole Fluid Conductivity Logging Method by Chin-Fu Tsang, Peter Hufschmied, and Frank V. Hale (NDC-1, LBL-24752).

2. A Code to Compute Borehole Fluid Conductivity Profiles with Multiple Feed Points by Frank V. Hale and Chin-Fu Tsang (NDC-2, LBL-24928; also NTB 88-21).

3. Numerical Simulation of Alteration of Sodium Bentonite by Diffusion of Ionic Groundwater Components by Janet S. Jacobsen and Chalon L. Carnahan (NDC-3, LBL-24494).

4. P-Wave Imaging of the FRI and BK Zones at the Grimsel Rock Laboratory by Ernest L. Majer, John E. Peterson Jr., Peter Blümling, and Gerd Sattel (NDC-4, LBL-28807).

5. Numerical Modeling of Gas Migration at a Proposed Repository for Low and Intermediate Level Nuclear Wastes at Oberbauenstock, Switzerland by Karsten Pruess (NDC-5, LBL-25413).

6. Analysis of Well Test Data from Selected Intervals in Leuggern Deep Borehole — Verification and Application of PTST Method by Kenzi Karasaki (NDC-6, LBL-27914).

7. Shear Wave Experiments at the U. S. Site at the Grimsel Laboratory by Ernest L. Majer, John E. Peterson Jr., Peter Blümling, and Gerd Sattel (NDC-7 LBL-28808).

8. The Application of Moment Methods to the Analysis of Fluid Electrical Conductivity Logs in Boreholes by Simon Loew, Chin-Fu Tsang, Frank V. Hale, and Peter Hufschmied (NDC-8, LBL-28809).

9. Numerical Simulation of Cesium and Strontium Migration through Sodium Bentonite Altered by Cation Exchange with Groundwater Components by Janet S. Jacobsen and Chalon L. Carnahan (NDC-9, LBL-26395).

10. Theory and Calculation of Water Distribution in Bentonite in a Thermal Field by Chalon L. Carnahan (NDC-10, LBL-26058).

11. Prematurely Terminated Slug Tests by Kenzi Karasaki (NDC-11, LBL-27528).

12. Hydrologic Characterization of Fractured Rocks — An Interdisciplinary Methodology by Jane C. S. Long, Ernest L. Majer, Stephen J. Martel, Kenzi Karasaki, John E. Peterson Jr., Amy Davey, and Kevin Hestir, (NDC-12, LBL-27863).

13. Exploratory Simulations of Multiphase Effects in Gas Injection and Ventilation Tests in an Underground Rock Laboratory by Stefan Finsterle, Erika Schlueter, and Karsten Pruess (NDC-13, LBL-28810).

14. Joint Seismic, Hydrogeological, and Geomechanical Investigations of a Fracture Zone in the Grimsel Rock Laboratory, Switzerland by Ernest L. Majer, Larry R. Myer, John E. Peterson Jr., Kenzi Karasaki, Jane C. S. Long, Stephen J. Martel, Peter Blümling, and Stratis Vomvoris (NDC-14, LBL-27913).

15. Analysis of Hydraulic Data from the MI Fracture Zone at the Grimsel Rock Laboratory, Switzerland by Amy Davey, Kenzi Karasaki, Jane C.S. Long, Martin Landsfeld, Antoine Mensch, and Stephen J. Martel (NDC-15, LBL-27864).

16. Use of Integrated Geologic and Geophysical Information for Characterizing the Structure of Fracture Systems at the US/BK Site, Grimsel Laboratory, Switzerland by Stephen J. Martel and John E. Peterson Jr. (NDC-16, LBL-27912).

Table of Contents

List of Figures

List of Tables

Abstract

The characterization of fractured rock is a critical problem in the development of a nuclear waste repositories in geologic media. A good methodology for characterizing these systems should be focussed on the large important features first and concentrate on building numerical models which can reproduce the observed hydrologic behavior of the fracture system. In many rocks, fracture zones dominate the behavior. These can be described using the tools of geology and geomechanics in order to understand what kind of features might be important hydrologically and to qualitatively describe the way flow might occur in the rock. Geophysics can then be employed to locate these features between boreholes. Then well testing can be used to see if the identified features are in fact important. Given this information, a conceptual model of the system can be developed which honors the geologic description, the tomographic data and the evidence of high permeability. Such a model can then be modified through an inverse process, such as simulated annealing, until it reproduces the cross-hole well test behavior which has been observed *insitu*. Other possible inversion techniques might take advantage of self similar structure. Once a model is constructed, we need to see how well the model makes predictions. We can use a cross-validation technique which sequentially puts aside parts of the data and uses the model to predict that part in order to calculate the prediction error. This approach combines many types of information in a methodology which can be modified to fit a particular field site.

Acknowledgements

1.0. INTRODUCTION

In many rocks fluid flows preferentially in the fractures. The prediction of flow through these rocks becomes a problem when the fractures which carry flow are not ubiquitously interconnected. In these cases, flow paths are controlled by the fracture geometry and may be erratic and highly localized. In contrast, porous materials often exhibit smoothly varying flow fields which are amenable to being treated as equivalent continua. The chaotic nature of flow in fractured materials means that the well developed and long-used techniques for modeling flow in porous media can not be successfully applied to fractured rock.

The problem of characterizing this type of fractured rock for fluid flow analysis comes down to defining a geometric basis for fluid flow. This fact has led to the development of models which incorporate the individual fractures explicitly (Hudson and La Pointe, 1980; Long et al., 1982; Robinson, 1984; Dershowitz, 1984; among others). These models represent the fractures as conductive segments of lines or planes. These are placed in space either deterministically or according to some stochastic process (as in Figure 1.1, for example). Fluid flow can then be modeled on the resulting network. Examples run with these models can be structured to examine the validity of the continuum assumption (Long et al. 1982). These have shown clearly that finite fractures can only be considered as an equivalent continuum under very restricted conditions when they are statistically homogeneous, sufficiently well connected and a large enough sample is used.

Application of these models to real field sites implies that one measure the details of the actual fracture geometry and produce models which reproduce the observed statistics of geometry of the fracture network. This involves determining a stochastic rule for locating fractures, determining their orientation, extent and conductivity. Then a network can be defined and flow patterns calculated. This approach to model building can be called stochastic simulation. What
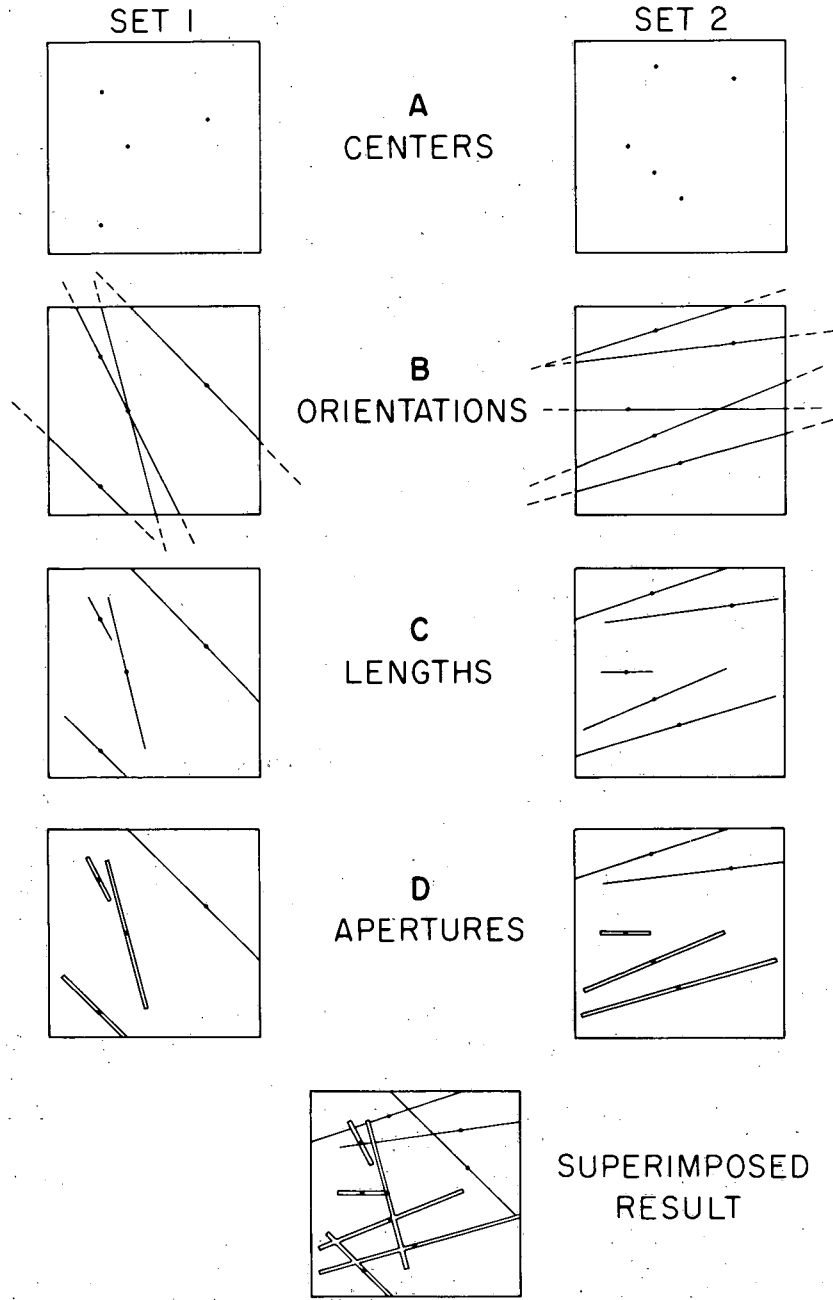
Figure 1.1. An example of a scheme for generating fracture networks as a Poisson distribution of line segments.

makes the characterization process difficult is that the fractures occur simultaneously on many scales and not all of the fractures are important for fluid flow. Some are filled and some are not connected to the hydraulic network. Furthermore, the interior of the geologic medium is not visible to us and we are forced to make this characterization solely through remote sensing and limited sampling from boreholes, outcrops and underground excavations.

Such an interpretation was made of the data at the Fanay-Augères mine in France (Billaux et al. 1989). Data used included fracture trace maps and logs and single hole packer tests. The analysis was based on assuming the fractures were disc-shaped and uniformly permeable in their plane. Data on trace lengths, orientation and fracture frequency were used to create a model of fractures in a 100m cube. The drift data indicated that fractures occurred in swarms, so the scheme for locating fractures in space consisted of generating locations for fracture clusters (parents) and then generating clusters of fractures (daughters) around the parents. The spatial statistics of the models were sampled in the same way that they were sampled by the field data. Then the model parameters were adjusted until the spatial statistics of the model and the field data were the same.

Conclusions from this effort were very striking. First we found that the use of one- and two-dimensional data to infer three-dimensional geometry is an impossible task. Many three-dimensional geometries can account for the same one- and two-dimensional data. Motivated by this observation, Davey and Long (1990) derived a linear programming algorithm for deriving any member of the infinite set of possible three-dimensional fracture statistics that will account for the same one- and two-dimensional data. Second, no matter how the three-dimensional geometry was determined, there were far too many fractures to account for the lack of connectivity evidenced in cross-hole hydrologic and tracer test results. If all the fractures were present and hydrologically active the medium would have behaved like an equivalent continuum but this was definitely not the case. We need somehow to constrain the three-dimensional geometry and more importantly we need to find some way to limit the model to those parts of the fracture system which actually do conduct water.

Fanay-Augères offered one other key fact in this regard. Two drifts were mapped in this mine: one wet, one dry. For both drifts the fracture geometry analysis seemed to indicate highly connected fracture networks. However, a major fault ran through the block of rock surrounding the wet portion of the drift. It seems that the hydrology of the site is controlled by major features i.e., fracture zones. This observation is certainly not confined to Fanay-Augères. In an example from the Stripa Mine in Sweden, Olsson et al. (1988a) state that 94% of the hydraulic transmissivity is found in 4% of a particular block of rock. Similar evidence exists at the Underground Research Laboratory (URL) in Canada (Martin et al., 1990). Localized fracture and fault zone control is often observed at geothermal sites (Halfman et al., 1984; Bodvarsson et al., 1985; Laky et al., 1989; Beall and Box, 1989; for examples) and in tunneling and mining the sudden encounter of large fluid inflows is a very common occurrence. In these cases the hydrology of the fractured rocks is controlled by a finite number of major conductors.

Creating a fracture hydrology model by counting and characterizing all the discrete fractures is a Herculean task almost equivalent to solving the Navier-Stokes equations in the pores of a porous medium instead of using Darcy's Law. Such detailed models require more data than can reasonably be obtained for practical applications. More importantly, the details are usually not important; only a few of the fractures conduct most of the water. Where does this leave us?

We think the answer may lie in accepting the discontinuous nature of the problem, and not losing the forest for the trees. First, recent work by Hestir and Long (1990) has shown how the behavior of complex Poisson networks of fractures can be reproduced on partially filled regular lattices. Thus, fracture networks are expected to exhibit the universal behavior that has been extensively studied through percolation and equivalent media theory (Kesten, 1982; Kesten, 1987; Kirkpatrick, 1973; Orbach, 1986; Pike and Seeger, 1974; Robinson, 1984; Stauffer, 1985; Zallen, 1983; among others). This work implies that it is possible to find simple lattice networks that behave like the complex fracture systems we have observed in the field. We call such a simplified network an "equivalent discontinuum." It is an equivalent model because it replaces the actual details of the physical system with an equivalent lattice. The equivalent model is a

discontinuum because parts of the lattice may be disconnected from other parts. The equivalent discontinuum is to fractured media what the equivalent continuum is to porous media.

Second, the focus of a characterization effort should be to find the most important features first. In a fractured rock, the big fracture zones often dominate the behavior. In this case, it is more useful to identify and characterize the major zones that are the primary conductors in the system than it is to collect data on detailed statistics of the geometry of the individual fractures.

In conclusion, our experience so far has indicated that focusing on the details of fracture geometry statistics is equivalent to "not seeing the forest for the trees." If fracture zones control the hydrology, then efforts should first be aimed directly at locating and characterizing fracture zones. We expect that the zones are not continuous and that the permeability structure within the zones is complex. One should concentrate on matching the hydrologic behavior of the zones, not the details of the fracture geometry. A model should be built from the large scale down, rather than from the details up and should focus on behavior instead of detailed geometry.

To make an equivalent discontinuum model, we characterize the features which control the first order behavior first, second order behavior second etc. In this way we can hopefully avoid the need for saturating the field with a huge number of detailed measurements. We try to include only as much detail as we need to make the prediction we need to make. Finally, we represent the details of the system with an equivalent discontinuum such that we reproduce the hydraulic behavior that was observed in the field. Such a philosophy requires that we can:

(1) Identify the types of feature that control the hydrology,

(2) Locate these features in the field, and

(3) Conceptualize the hydraulic system

(4) Test the hydrologic behavior of the system

(5) Develop an inverse technique to find an equivalent simplified lattice which has the same hydraulic behavior observed in the field.

This effort is inherently interdisciplinary in nature. Any one discipline, applied without

respect to information gained from other types of investigations, will generate information that is unconstrained and therefore largely uninterpretable. If we only used hydraulic data, we would have a very non-unique characterization: many flow systems could account for the same hydraulic behavior. To narrow down the possible explanations we need to have an accurate conceptual model for the flow system. Geologic tools give us much we want to know about what theoretically controls the flow, but geologic tools do not "see" into rock. Geophysics can see into the rock, but geophysical techniques do not directly measure hydrologic properties. Geophysics can provide critical information about where water might be, it does not necessarily show us where the permeability is. The most power is gained by combining all these techniques into a unified approach.

This report gives an overview of interdisciplinary hydrologic characterization. It draws from experiences at a variety of field sites in fractured rock in an attempt to show the major constituents of a complete site characterization effort. Every site is different, but this approach and its tools are flexible and can be applied at a variety of sites with some modification. The fundamental philosophy behind the approach is very general and is applicable to the characterization of many types of geologic media. In the examples given here, the hydrology is dominated by flow in fracture zones. One could easily modify the methodology given here for sites where the fracture zones are not very distinct. In such cases one might wish to develop a stochastic generator to reproduce the fracture network and allow some of the parameters of the generator to be optimized in an inverse technique. One should consider the work presented here as a "box of tools" which would not be applied the same way at every site.

There is no one example where all the components of our characterization methodology have been applied. So, in order to present the ideas we have structured the report as follows. The format of the each chapter is to discuss a component of characterization in general and then provide illustrative examples. Many of the examples are discussed in more detail in other reports of this series (Majer et al., 1990; Davey et al., 1990; Martel and Peterson, 1990). Consequently, this report may appear to be somewhat repetitious, but the intent is to gather a complete set of exam-

ples in one place.

For an understanding of what features are important and why, we turn to geology and geomechanics (Section 2.0). For understanding what makes these features visible, we rely heavily on the recent advances in geophysics and geomechanics that have allowed fractures zones to be imaged (Section 3.0). We interpret the location of the features using a combination of geologic mapping and geophysical interpretation (Section 4.0). Well tests are designed to test the hydrologic role of these features (Section 5.0). Based on these, we build a hydrologic conceptual model of the the rock which we call a template (Section 6.0). The template should contain all the likely major conductors as the basis for fluid flow calculation. In this template we include as much as possible of the qualitative hydrologic attributes of the zones identified through geology and geomechanics. Finally, we arrange conductors in a manner that conditions the model to observed well test behavior. In other words, within the template we identify patterns of conductance that can explain the observed hydraulic behavior. We use a new inverse technique called simulated annealing to arrange the conductances such that they explain observed distributions of head, observed fluxes, or observed tracer test results (Section 7.0). Some alternatives to simulated annealing are discussed (Section 8.0) which incorporate the fractal-like nature of fracture networks. Finally, we must be concerned with the validation of these models (Section 9.0).

2.0. GEOLOGIC AND GEOMECHANICAL IDENTIFICATION OF HYDROLOGICALLY IMPORTANT STRUCTURES

The purpose of the geologic/geomechanical approach is to gather information bearing on how fluid is likely to flow within a fractured rock mass. As discussed above, it is common to observe that major fracture zones carry most of the water in a fractured rock mass. The tools of geology and geomechanics have traditionally been used to study the history and morphology of these features. However, it is less common to see these tools used to infer hydrologic behavior. Detailed geologic mapping at the surface and in the subsurface provide information on the general structural characteristics of the major features and suggest how these features might behave hydrologically.

This section discusses idealized fracture zones and then cites specific examples from the Grimsel Rock Laboratory in Switzerland. For a detailed description of the geology refer to Keusen et al. (1989), Martel and Peterson (1990), and Bossart and Martel (1990). The idealizations in Section 2.1 can be thought of as "themes" which are very commonly observed. These themes reflect common mechanisms for fracture formation which result in common fracture patterns. In a great number of cases, one can describe fractures at specific sites as "variations" on these themes. Some of the fracture zones at Grimsel closely resemble the simple idealizations. Others reflect relatively complex and varied fracture-forming mechanisms, but even for these cases, recurring fracture pattern elements and growth processes can be identified.

2.1. Fracture Zone Patterns and Growth Mechanics

Three classes of relatively planar structures are common in a variety of rock types and geologic settings: fracture zones, shear zones, and igneous dikes (Figure 2.1). The fracture patterns which commonly develop in or along these structures reflect the control that the stress state and the presence of pre-existing weaknesses exert on fracture growth.
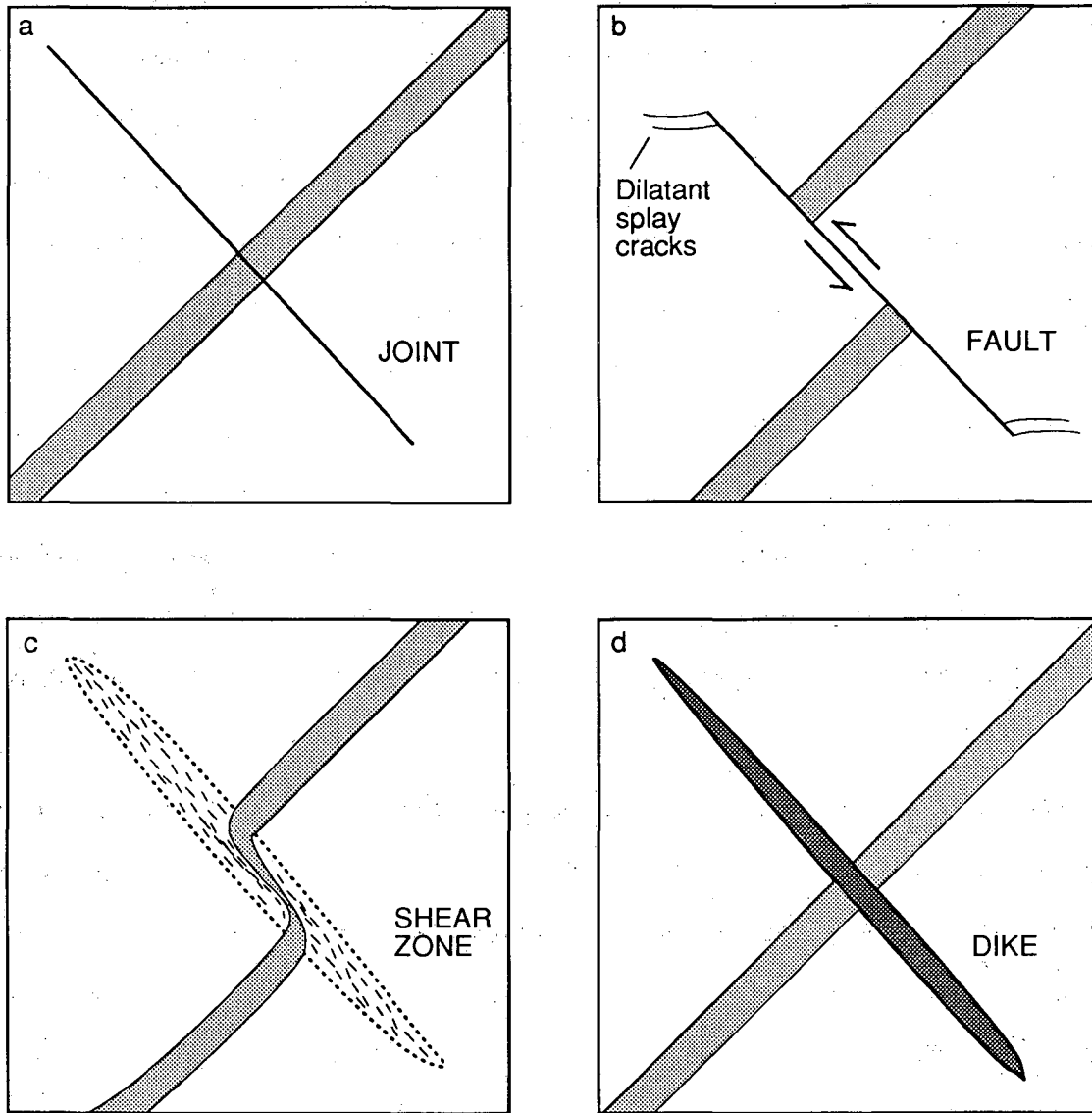
Figure 2.1. Four examples of common planar geologic structures. The feature in light grey
is an arbitrary marker: (a) joint, (b) fault, (c) shear zone, and (d) dike.

Fractures are structural discontinuities; a feature cut by a fracture cannot be traced continuously across it. There are two major kinds of fractures, joints or dilatant fractures (Figure 2.1a) and faults (Figure 2.1b). The relative displacement of the opposing walls of a joint is predominantly perpendicular to the joint; relative displacement parallel to the joint is minimal. Joint walls may dilate in response to either a remote tensile stress or an internal pressure (such as from a fluid) that exceeds the compressive stress perpendicular to the joint (Pollard and Segall, 1987). The relative displacement of the opposing walls of a fault is predominantly parallel to the fault. Shear zones (Figure 2.1c), like faults, accommodate shear deformation, but unlike faults, deformation across shear zones is continuous. The mineral grains in a shear zone characteristically are preferentially oriented subparallel to the zone, so the rock in shear zones is anisotropic. Ductile shear zones presumably form under higher temperature/pressure conditions or lower strain rates than fractured fault zones. Still, many fault zones are probably rooted in ductile shear zones (e.g. Sibson, 1977) or develop from them. Igneous dikes (Figure 2.1d) can either intrude preexisting fractures or form their own (Delaney et al., 1986). Many dikes have a maximum thickness greater than a meter, whereas most joints have a maximum thickness of less than a centimeter. It is not uncommon for dikes to serve as nuclei for shear zones (Lisle, 1989) or for deformation of dikes to cause fracturing in the adjacent rock.

For these types of planar features, we describe the mechanisms which can explain the observed fracture patterns. Qualitative descriptions of these patterns can in turn be used to describe the qualitative hydrologic behavior. Thus, understanding the mechanisms which cause fracture patterns provides a tool for predicting hydrologic behavior where fracture patterns cannot be observed directly.

There has been significant recent progress in our understanding of fracture-forming mechanisms. Traditionally, fractures in the earth have been considered to be a product of shear failure in response to remote loads. As a result, the growth of joints and dikes and some aspects of the fracturing along faults have been difficult to account for. More satisfying explanations for fracture formation can be found by considering fractures from the standpoint of fracture mechan-

ics, which deals with the remote stresses and the stress concentrations near a fracture tip. Theoretically, the near-tip stress field will be very heterogeneous, with large shear, compressive, and tensile stresses occurring; tensile near-tip stresses can arise no matter how large the regional compressive principal stresses are (Lawn and Wilshaw, 1975). Rock properties together with the local stress state will govern whether fracture growth occurs by shear or tensile failure.

2.1.1. Joints

Joints probably are the most common type of rock fracture. In relatively isotropic rocks like massive sandstone or granite, an isolated joint typically will be very nearly planar. This probably reflects a remote stress state that is symmetric with respect to the joint, the least compressive stress being perpendicular to the joint. The theoretical near-tip tensile stress concentration is symmetric about the tip of a isolated, slowly-growing, dilatant fracture, but the shear stress concentration is asymmetric (Lawn and Wilshaw, 1975). Accordingly, in-plane growth would be favored if a joint grew due to tensile failure at its tip, and out-of-plane growth would be favored if it grew due to shear failure at the tip. The planar shape of a joint and the style of relative displacement across a joint indicates that joints propagate in response to localized tensile failure at their tips and not shear failure.

Joints usually occur in sets of nearly planar subparallel joints (Figure 2.2a). These observations are consistent with the hypothesis that the regional stresses strongly control the orientation of the joints, with the maximum compressive stress being significantly different in magnitude from the least compressive stress (Olson and Pollard, 1989). Without a strong contrast in the remote stresses, the stress perturbations caused by the presence of the joints themselves would cause the joints to have highly curved shapes (Olson and Pollard, 1989). Elastic analyses demonstrate that the growth of a given joint would diminish the stress driving the growth of most nearby joints; this shielding effect is most strongly exerted by the longest joints. As a result, the growth of the longer joints should be favored, and the resulting fracture pattern should contain many short joints and fewer long ones (Segall and Pollard, 1983a). This is precisely one of the patterns most commonly observed.
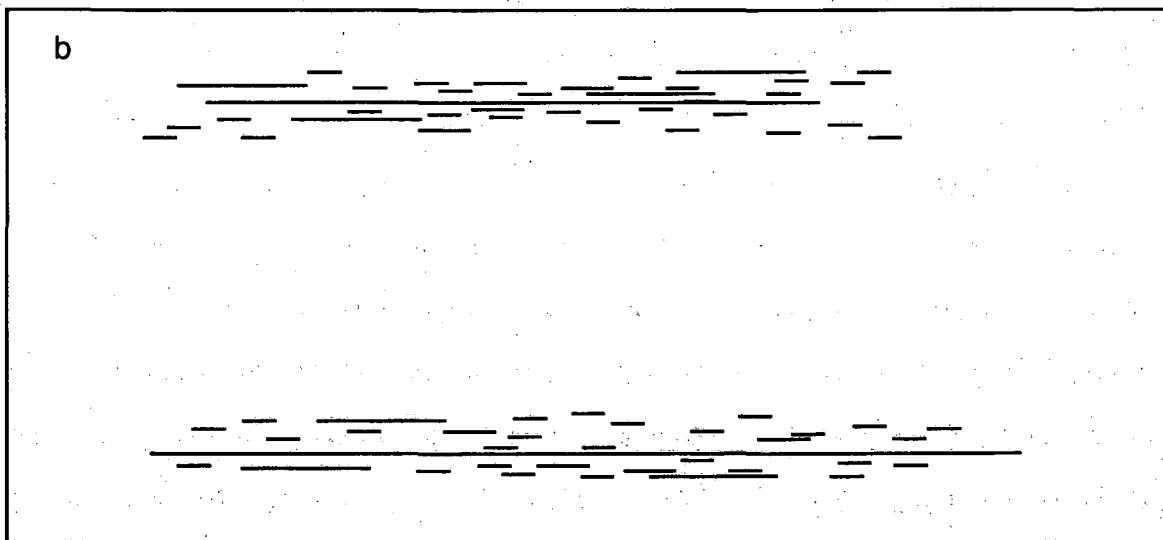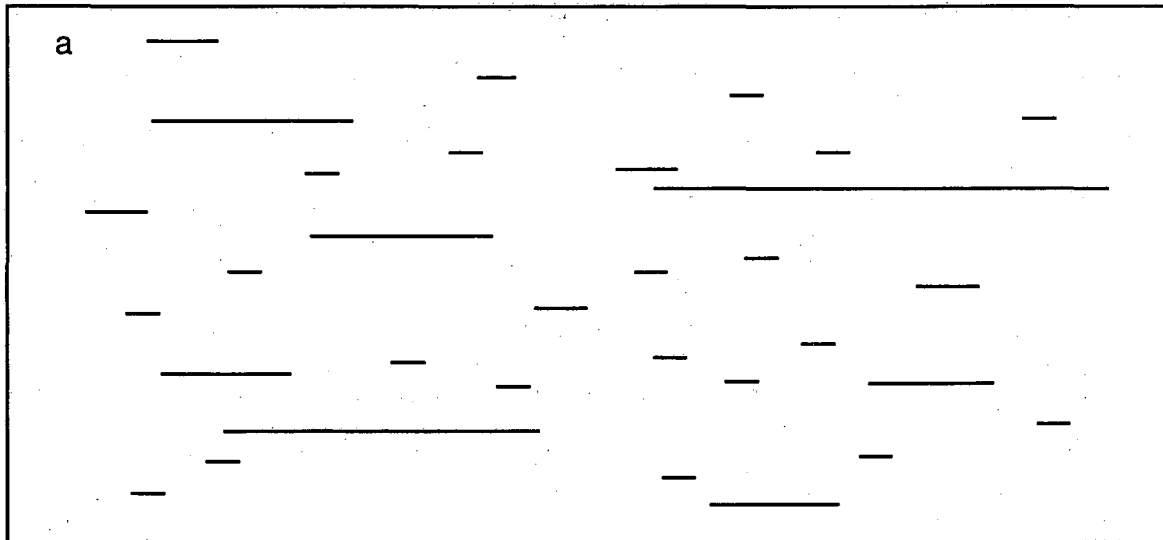
XBL 905-1674

Figure 2.2. Examples of joint patterns: (a) joint set and (b) two joint zones. In the upper zone, joints have formed in front of the longest joint. In the lower zone, the longest joint has propagated past previously-formed flanking joints.

Joint zones (Figure 2.2b) consist of clustered, overlapping, subparallel joints (Dyer, 1983) and form one kind of fracture zone. The spacing between joint zones is large relative to the spacing of joints within a zone. Both the zones and the joints in them are nearly planar. Joint zones resemble clusters of joints along some dikes, and both the zones and the clusters may form by a similar process. Some dike-parallel joints are inferred to open in response to the tensile stress concentration at the tip of a propagating dike (Delaney et al., 1986) and then be left in the wake of the dike tip as it advances. By analogy, a joint zone may form in response to the stress concentration at the tip of a particularly large joint. Such patterns are likely to create conductive pathways parallel to a dike (or large joint), but not necessarily any conductance across the feature. The resulting pattern would conduct fluid parallel to the dike (or large joint) much more readily than across it.

2.1.2. Faults

Faults, the second major class of fractures, have traditionally been considered not only to accommodate shear displacement but also to *originate* as shear fractures (e.g. Sylvester, 1988). This perspective has developed largely as a result of shear fractures being formed in numerous laboratory compression tests on small rock samples. However, in recent years this view has come under increasing scrutiny. Detailed examinations of isotropic test specimens consistently show that shear fractures are not primary features. Instead, arrays of dilatant fractures first form parallel to the maximum compressive stress; only if deformation proceeds far enough do these fractures link up to form shear fractures (e.g. Peng and Johnson, 1972). Furthermore, attempts to propagate fractures in isotropic rocks under shear loads usually result in dilatant fractures propagating out-of plane from the fracture tips (Ingraffea, 1981). In laboratory compression tests on anisotropic rock, shear fractures develop parallel to the anisotropy in the rock (Donath, 1961); these shear fractures may be primary structures. The laboratory compression tests thus imply that faults rarely originate as shear fractures in isotropic rock masses and that preexisting dilatant fractures and rock anisotropy would strongly influence fault growth.

Field observations consistently show that faults of substantial size exploit pre-existing weaknesses as they develop (e.g. Muehlberger, 1986). In fact, we are aware of few examples (e.g. Aydin and Johnson, 1978) to the contrary. Faults and fault zones can originate from pre-existing joints (Segall and Pollard, 1983b; Martel et al., 1988). Faults can also develop from pre-existing shear zones; shear zones in turn can develop from joints (Segall and Simpson, 1986) and dikes (Lisle, 1989). Systems of dilatant features (i.e. joints and dikes) can have lengths of many kilometers and can provide long planar flaws for long planar faults to develop from.

Fault zones can develop as originally discontinuous faults that become linked together (Figure 2.3). Dilatant fractures that form as a result of fault slip can serve as links (Segall and Pollard, 1983; Martel et al., 1988) as may shear fractures (Sibson, 1986a). The secondary linking fractures occur in predictable locations. Elastic analyses indicate that secondary fractures are likely to form where extensional strains are high along faults. High strains would be expected at the ends of faults and at geometric irregularities along them, and numerous dilatant fractures do occur in those places (Sibson, 1986a; Martel et al., 1988; Martel and Peterson, 1989). Hydrothermal mineralization is common in regions such as these (Sibson, 1981) and provides direct evidence for pronounced fluid flow there. Secondary dilatant fractures also occur where geometric irregularities are not pronounced (Martel et al., 1988), presumably as a result of transient stress concentrations arising from slip along the fault zones (Martel and Pollard, 1989). Both kinds of secondary dilatant fractures tend to be aligned perpendicular to the least compressive remote stress. Because the remote principal stresses would be oriented oblique to an activated fault zone, many of the fractures in fault zones can have orientations that are systematically oblique to the zones as a whole.

The laboratory compression tests on anisotropic rocks suggest that anisotropy in the earth may control the development of many fault zones. Swanson (1988) has documented aligned faults that developed along layering in metamorphosed sedimentary rocks. Anisotropy may also enhance the ability for aligned sets of fractures to subsequently form in shear zones. The fabric in ductile shear zones commonly has an anastamosing or braided form (Berthe et al., 1979), and
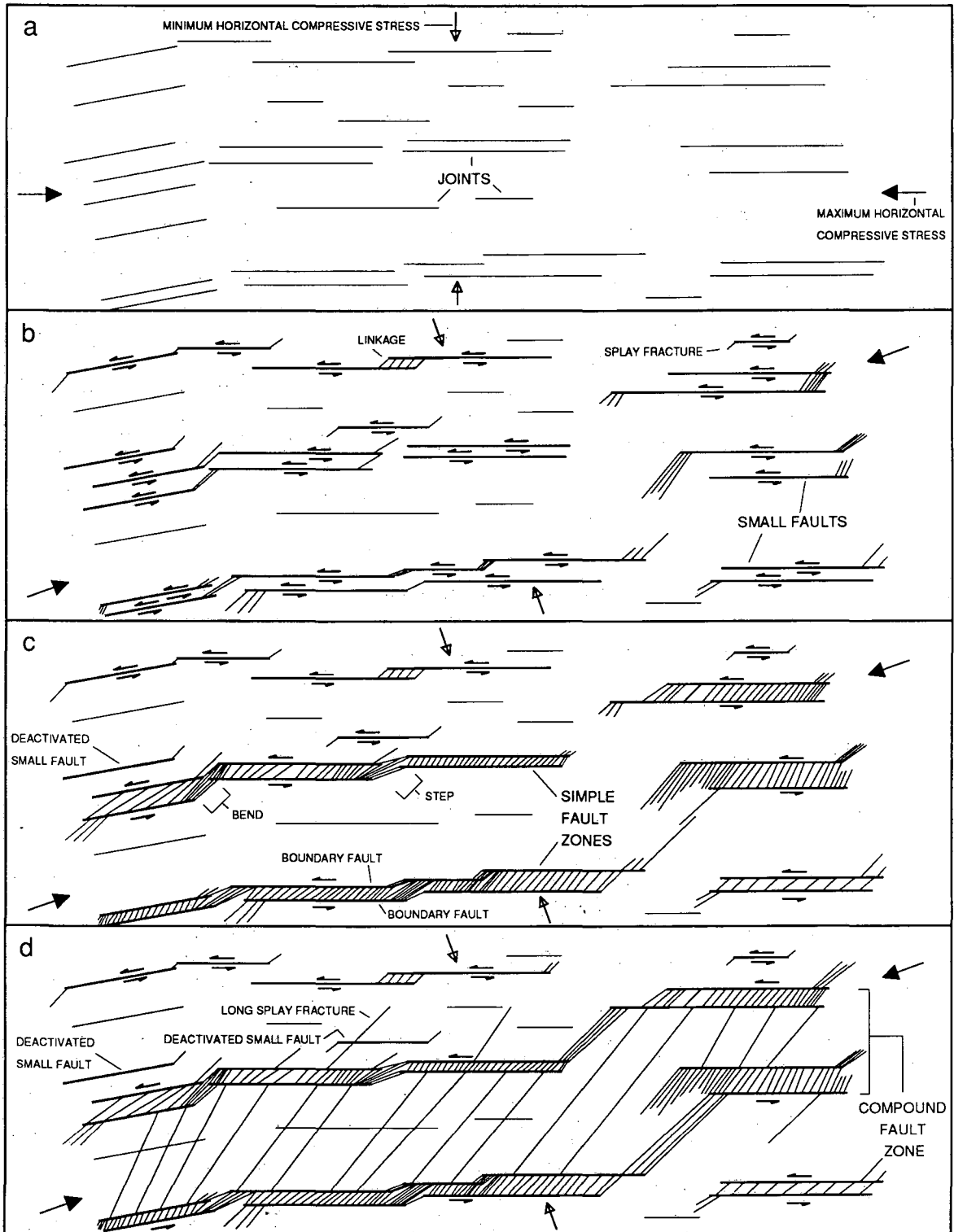
Figure 2.3. Growth of fault zones from a joint set: (a) opening of joints, (b) development
of faults, (c) development of simple fault zones, and (d) formation of
compound fault zones (from Martel, 1990).

XBL 905-1675

anastamosing fractures are common in fault zones (Wallace and Morris, 1986). The braided fractures in many of the shear zones at Grimsel follow the foliation (Figure 2.4).

Many fault zones have been reactivated under different stress regimes and different environmental conditions (Muehlberger, 1986; Sibson, 1986b). Some of the key factors influencing the growth of fractures in fault zones, such as the magnitude and orientation of the regional principal stresses, the mechanical behavior of the rock, and the fluid pressure, can change with time. Thus, many generations and orientations of internal fractures may form. As fractures become more numerous, the stress state in a fault zone is likely to become increasingly heterogeneous. Because of the varying conditions under which fracturing would occur, the fracture patterns that develop in many ancient reactivated fault zones are likely to be quite chaotic. In such cases, fractures of almost any orientation can occur and the current state of stress may determine which of these fractures are likely to be most open and thus most conductive.

2.2. An Example Analysis of Major Geologic Structures from Grimsel

In order to explain how this type of analysis is applied to a site, we turn to examples from the Grimsel Underground Rock Laboratory. The host rock at Grimsel consists of foliated granite and granodiorite. We refer to these collectively as granite. The granite has been multiply deformed and is strongly foliated. The major geologic structures at Grimsel are fracture zones which in some cases developed along shear zones and metamorphosed lamprophyre dikes. Two sets of steeply-dipping fracture zones are prominent, NW-striking K-zones and NE-striking S-zones. The lamprophyres dip steeply and generally strike northwest. Observations and measurements of fluid flow into the laboratory indicate these structures and associated fractures account for nearly all of the fluid circulation at Grimsel (Keusen, et al., 1987). The granite most likely has been deformed more than once as evidenced by the macrostructure.

2.2.1. K-zones

A 100-m-long section of an exceptionally well-exposed K-zone (Figure 2.5) was mapped at the surface about one kilometer from the laboratory. This zone strikes NW, nearly at right angles
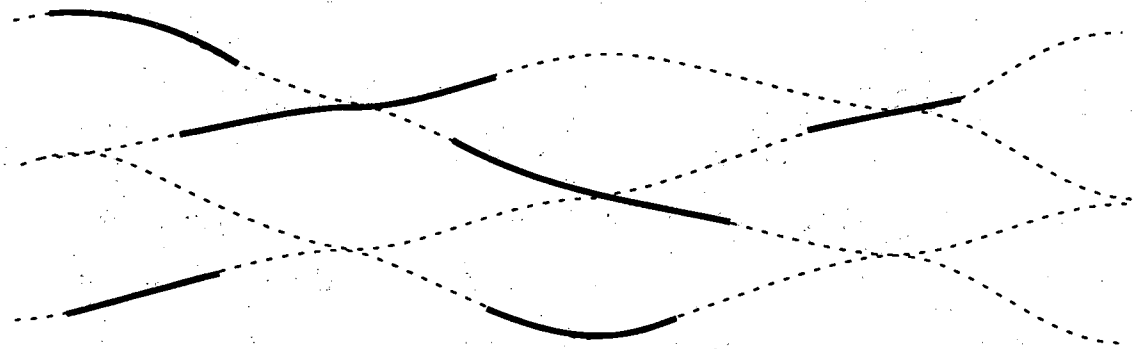
XBL 905-1676

Figure 2.4. Formation of fractures (heavy lines) in a shear zone. Light lines represent aligned
minerals defining the foliation within the shear zone.

Continuation
of Fault Zone

Prominent Internal Fractures Strike N85E; Subvertical Dip

Sheared QTZ Vein

Thin Shear
Zone at Edge

Lamprophyre
with abundant quartz

East edge of
lamprophyre is sheared

Lamprophyre with
Little QTZ

Thin zone of intense shearing

Lamprophyre + quartz

Lamprophyre + quartz

Fault Zone

Left-lateral
splay cracks

Lamprophyre Dike

N

0   50 meters

Thin quartz veins

XBL 898-7695

Figure 2.5. Map of part of a K-zone and a lamprophyre dike exposed at the surface near the
Grimsel Rock Laboratory.

to the foliation. The zone appears to offset a steeply-dipping lamprophyre dike left-laterally by about 20 m. The zone contains a series of NW-striking faults that are linked by smaller fractures that strike ENE. Both kinds of fractures dip steeply. Structurally, this zone resembles some left-lateral fault zones in the Sierra Nevada of California that developed from fault-parallel joints (Martel et al., 1988; Martel, 1990), and we suspect that it developed the same way.

The K-zone is not a uniform, planar structure. It has a nonlinear trace, with subparallel segments joining at echelon steps, and varies in width from about one to ten meters. The relative abundance of the internal ENE-striking fractures varies markedly along strike. They are most abundant and the zone is the widest in the NW corner of Figure 2.5, at the left echelon step between two faults. The orientation of the internal fractures suggests that the K-zone slipped left-laterally when the axis of maximum horizontal compression was oriented ENE or east. Both the K-zone as a whole and its most prominent internal fractures developed at a fairly high angle to the foliation in the rock.

2.2.2. S-zones

In contrast to the K-zones, the S-zones display a braided fracture structure. This pattern is exposed both at the surface (Figure 2.6) and in the subsurface. The braided structure is present in plan view and in cross section (Figure 2.7) but is most pronounced in plan view. The structure of the S-zones is clearly tied to the foliation of the granitic host rocks. At a macroscopic scale the S-zones parallel the foliation in the rock. Many of the fractures border mylonite bands that, in part, define the foliation. The macroscopic fracture structure of the S-zones also mimics the microscopic arrangement of the biotites, which largely define the foliation. The S-zone fractures parallel the biotites and are particularly well developed where biotite is concentrated. In plan view the biotites form a braided pattern as they wrap around feldspar and quartz grains in the rock, analogous to the braided pattern formed by the S-zone fractures. The feldspars tend to be elongated parallel to the dip of the foliation, so in cross sections perpendicular to foliation strike the braided pattern is more drawn out; this too is analogous to the pattern formed by the S-zone fractures.

Figure 2.6. Photograph of the edge of an S-zone, ruler for scale. Note the braided fracture structure.
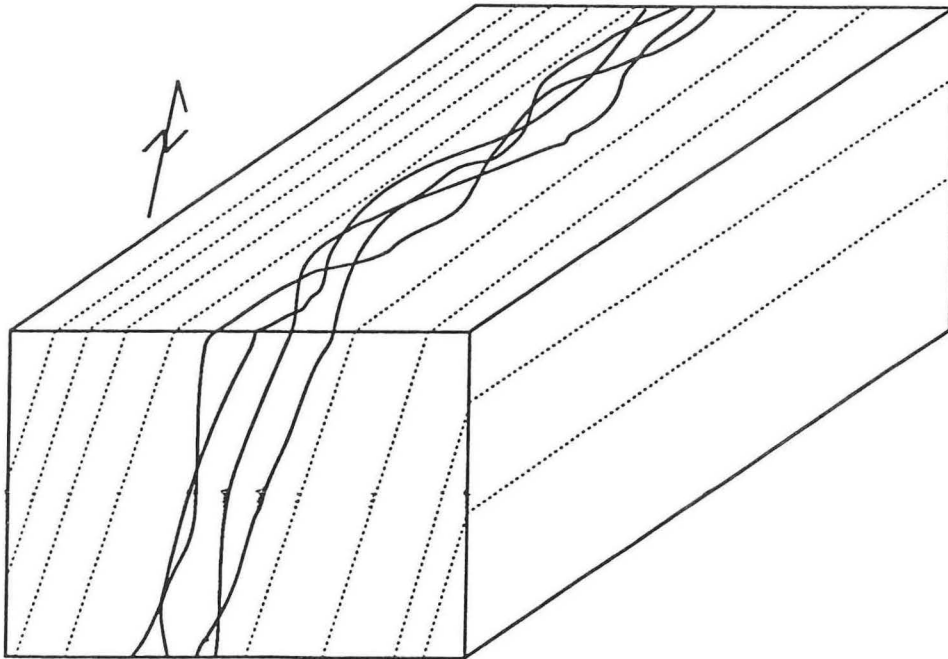
XBL 8910-3867

Figure 2.7. Block diagram showing braided structure of S-zones. Braided structure is more pronounced in plan view than in cross section. The solid lines represent fractures. Dashed lines mark foliation of rock.
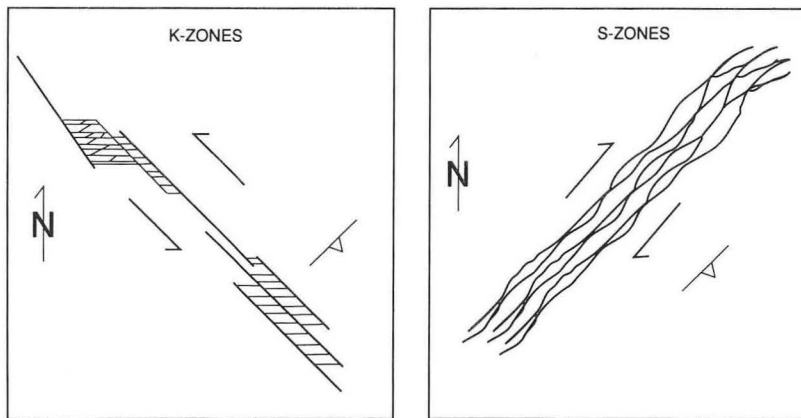
XBL 903-783

Figure 2.8. Comparison of K- and S- Zones. The rock foliation dips steeply to the southeast.

The distinctly different structures of the K- and S-zones (Figure 2.8) appear to reflect differences in the flaws from which the zones developed. The K-zones apparently developed from an irregular distribution of preexisting west or northwest-striking fractures, which, at least locally, have in turn developed on older ductile structures, whereas the S-zones developed upon the foliation in the rock. The K- and S- zones are excellent examples of the patterns illustrated in Figures 2.3 and 2.4 respectively.

2.2.3. Lamprophyres

Lamprophyre dikes are superbly exposed at several places in the Grimsel laboratory tunnels. Most of the dikes strike northwest (oblique to the foliation of the granite) and dip steeply. The lamprophyres typically can not be traced as continuous structures along strike for more than several meters. These dikes exhibit a variety of spectacular deformational features. The fracture pattern associated with the dikes dominantly reflects the effects of dike deformation rather than dike emplacement. The resulting fracture pattern is decidedly more complex than the idealized case of dike-parallel jointing shown in Figure 2.2. As will be shown, the deformation of the lamprophyres and the associated fracturing clearly reflect the rheologic contrast between the dike rock and granite at the time of deformation.

Two of the most spectacular deformational features associated with the northwest-striking lamprophyres are horizontal Alpine tension fissures (Zerrklufte) and vertical mullions (Figure 2.9). Many of the fissures exposed in the Grimsel tunnels extend from closeby lamprophyres; some are more that a meter tall and extend several meters from the lamprophyres. The mullions are exposed as a series of periodic cusps at the dike edges and indicate the lamprophyres were less viscous than the granite during deformation (Ramsay, 1967; Smith, 1975, 1977). The horizontal fissures and vertical mullions appear consistent with the dikes being extended vertically and shortened approximately along strike, respectively. The asymmetry of the cusps indicates the axis of maximum shortening diverged slightly from the strike of the lamprophyres (i.e. deformation was not perfectly symmetric with respect to the dikes).

MULLIONS

MULLIONS

LAMPROPHYRE

ALPINE
TENSION
FISSURES
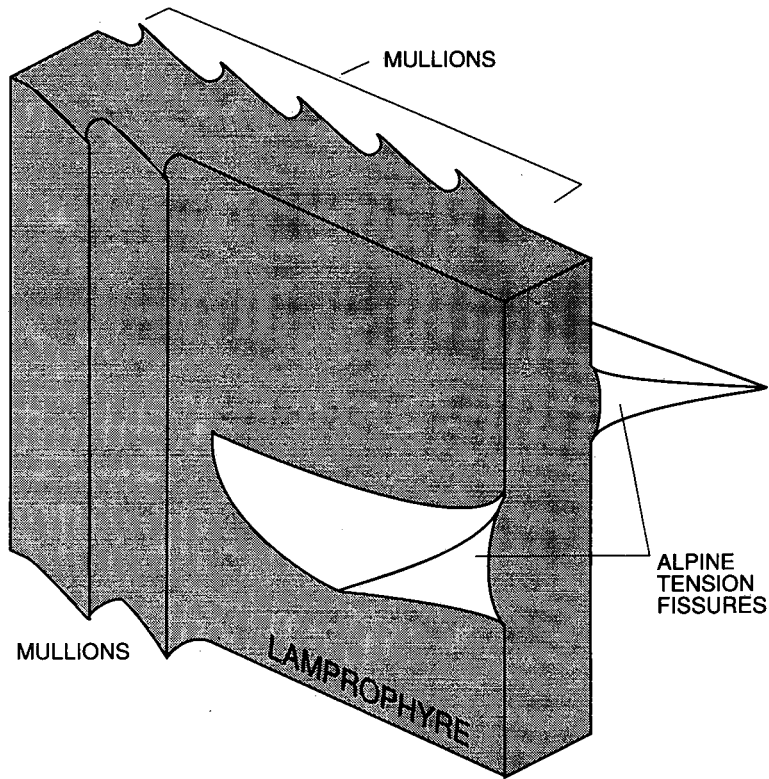
XBL 905-1671

Figure 2.9. Block diagram showing vertical mullions and mineral-filled, horizontal Alpine
tension fissures extending from a vertical lamprophyre.

The lamprophyres are also internally foliated and commonly have splay fractures near their ends. These features are less-spectacular than the fissures and mullions but may be quite significant hydrologically. The dike rock contains abundant mica, and the alignment of the mica defines the foliation of the dikes. This internal foliation strikes oblique to the foliation of the host rock and reflects the rheologic contrast between the dikes and the granite. The dike foliation has a sigmoidal trace in plan view, striking east-west near the dike centers and paralleling the highly sheared dike margins. The lamprophyre-end splay cracks dip steeply and strike to the north (Figure 2.10) indicating right-lateral strike-slip displacement across a lamprophyre (Pollard and Segall, 1987). The ability of the lamprophyres to serve as faults is consistent with inferences drawn from the mullions that the lamprophyres were less viscous than the granite and were loaded in a non-axisymmetric manner.

2.2.4. Hydrologic Implications

The K- and S-zones have markedly different structures and probably have markedly different fracture flow characteristics. The K-zones appear structurally more heterogeneous than the S-zones and therefore fluid flow may be more heterogeneous along the K-zones than the S-zones. Flow in the K-zones is most likely to be localized at steps, where the fracturing is most extensive. In three dimensions, these steps might act as nearly vertical pipes. The principal fractures in the S-zones strike subparallel to the zones, so the permeability would probably be greater along these zones rather than across them. Because S-zone fractures appear more tortuous in plan view than in vertical cross section, we suspect that the average vertical permeability of the S-zones would be greater than the horizontal permeability.

If the lamprophyres were undeformed, one might expect little flow to occur along or across them. However, water does seep from the lamprophyres and the deformation of the lamprophyres provides a variety of paths for concentrated fluid flow. The best flow paths probably occur at the dike margins, where sheared rock could allow for enhanced flow and large-aperture tension fissures could serve as particularly significant horizontal conduits. The splay cracks near the ends of some lamprophyres can act as channels for vertical flow. In addition, although the micaceous
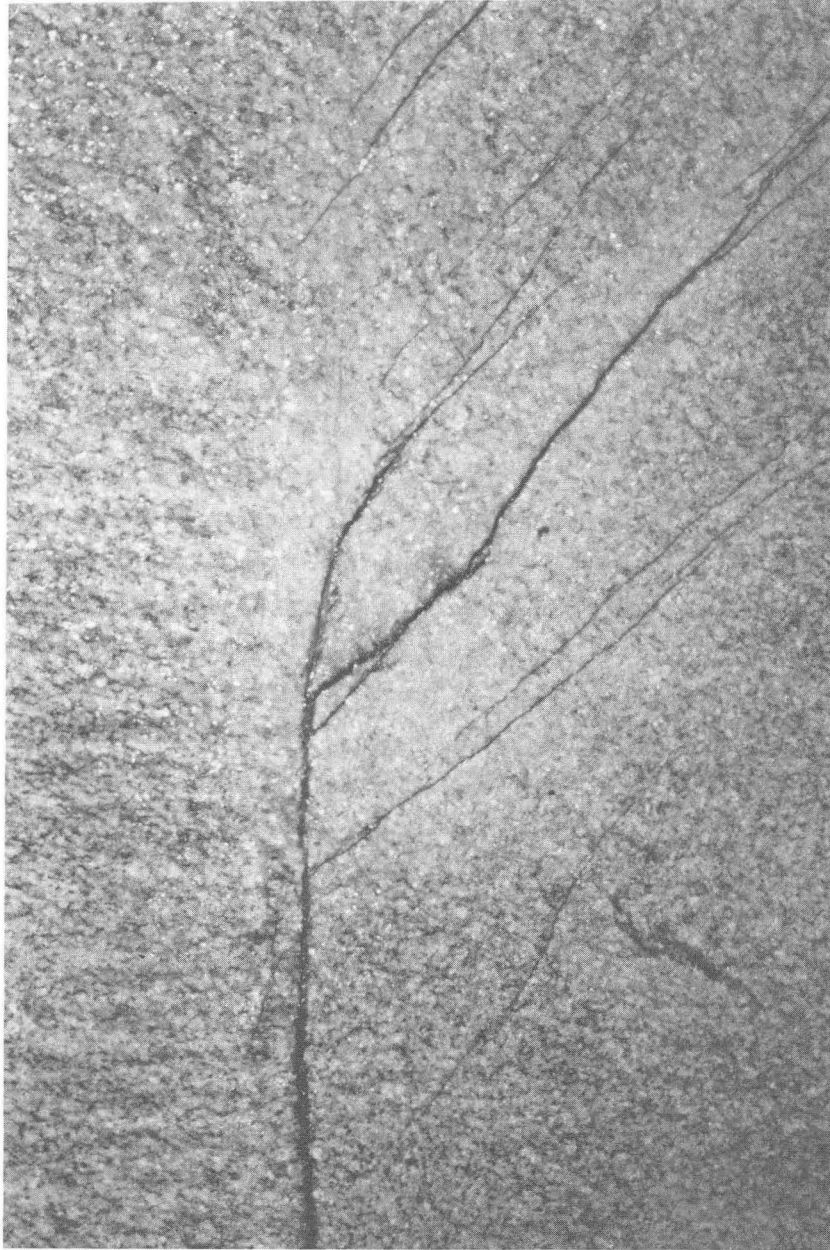
CBB 890-9971

Figure 2.10. Photograph of splay cracks near the end of a lamprophyre in the heater test tunnel. Stains along splay cracks indicate enhanced permeability.

dike rock might be expected to swell and impede fluid flow across the lamprophyres, the oblique internal foliation of the lamprophyres provides potential flow paths across the dikes. Finally, because individual lamprophyres are discontinuous one might expect the hydrologic characteristics along a cluster of dikes to vary.

The nature of the intersections between the major structural features is an important factor in the hydrology at Grimsel. The S-zones intersect both K-zones and lamprophyres; the K-zones and lamprophyres are nearly parallel. In some cases S-zones extend across lamprophyres, whereas in other cases an S-zone will terminate in a lamprophyre. Lamprophyres may or may not impede flow along the trend of an S-zone. Detailed mapping (Bossart and Martel, 1990) suggests that fracturing may be particularly extensive where S-zones and K-zones intersect, so S-zones and K-zones probably would be well connected hydrologically.

3.0. GEOPHYSICAL IMAGING OF FRACTURES

Once hydrologically important features have been identified, the next step is to locate these features within the rock mass. In so far as possible, we wish to do this in a deterministic way; where it is not possible, we must rely on stochastic methods. The tools of geologic mapping can be used to project the features into the rock mass where there is direct access to fracture zones in outcrops, drifts or boreholes. Geophysical techniques are offering more and more promise for extrapolating these maps into regions that are not exposed. In this section, we describe how geophysics can be used to find fracture zones. In Section 4.0, we demonstrate how the geophysical and geological information can be combined.

Rock fractures have several properties that may distinguish them from the surrounding matrix rock. For our purposes, these properties can easily be divided into two major categories: electrical properties and mechanical properties. Consequently, we can probe the rock with either electromagnetic waves or seismic waves to find the fractures.

Electrical methods can be further subdivided into DC and AC methods. DC methods are currently a topic of research and will not be discussed here, but AC methods in the form of radar and low frequency electromagnetics have been extensively used in several rock types. The DC or zero frequency methods are usually used to determine the bulk resistivity of the rock. Radar is discussed briefly below, but the reader is referred to Olsson et al. (1988b) for a more complete discussion of the theory behind the use of radar and for an example application to the Stripa site in Sweden.

Seismic signals are sensitive to the elastic properties of the rock which are in turn influenced by rock density, porosity, water content as well as fracture stiffness and orientation. Seismic methods can be divided into acoustic or P-wave methods, and those also employing the

shear component of the wave. P-wave analysis has been in common use for some time, but the use of S-waves is a fairly recent endeavor. Beyond these two topics, there are some very new ideas for using the full wave form in diffraction analysis. The seismic methods can be further divided into the active and passive methods. The passive methods involve "listening" to seismic energy being created by stress changes or natural seismicity such as microearthquakes or acoustic emissions (AE) near the underground openings. Active methods involve introducing energy into the ground and observing how the seismic waveforms change due to inhomogeneities or aniso-tropy in the rock. These topics are the subject of intensive research at LBL which are discussed below.

3.1. Radar Methods

Radar signals are used to locate fracture zones in rock through both reflection and tomo-graphic techniques. In granitic rock, it is assumed that most rock matrix properties are relatively constant so that hydrologic features such as fracture zones, increased porosity, and water content will dominate. However, in general, non-fluid conducting porosity cannot be distinguished from conducting porosity.

Radar signals are sensitive to changes in dielectric constant and electrical conductivity (Sen, et al. 1981). Radar velocity equals $c/\sqrt{\mu/\varepsilon}$, where c is the electromagnetic wave velocity in a vacuum, ε is the dielectric constant and μ is the magnetic permeability. The amplitude is a function of $(\sigma/2)\sqrt{\mu/\varepsilon}$, where σ is the electrical conductivity. The magnetic permeability, μ, is, for all practical purposes, a constant. Slowness, therefore depends only on the dielectric constant, ε, and attenuation depends on both the dielectric and electrical conductivity, ε and σ.

Both the electrical conductivity, σ, and dielectric constant, ε, increase with the water content. Based on the functions given above, the slowness tomogram should give the most direct correlation with fluid paths in the medium because it depends only on contrasts in ε. However, there is more contrast between values of σ than between values of ε. As a result, the attenuation tomograms can be more useful for imaging differences in rock properties.

Radar reflection techniques can be used along with the crosshole tomography to provide additional independent information about the fracture zones. Single-hole reflection data are used to determine reflectors in the same manner as common surface reflection surveys. It is possible to determine where the reflectors intersect the borehole and their orientation relative to the boreholes. The locus of possible reflectors is then a cone passing through this intersection. Use of a directional antenna makes it possible to determine the actual orientation of the feature. The cross-hole reflection technique is similar to the single-hole method, and can, in principle, uniquely determine the orientation of the reflector. However, the analysis is more difficult.

An integrated analysis of the radar data is then used to identify major features in the rock to make certain each feature is consistent with the data sets (Olsson et al., 1988a,b). The features are normally assumed to be planar fracture zones. Normally, a feature is first identified in the tomo-grams and the intersections between the feature and the boreholes are estimated. These intersec-tions can usually be corroborated with a reflector from the single-hole reflection analysis. The possible orientations from the reflection data are displayed in a Wulff polar diagram. A pair of possible planes are determined by the two possible orientations which lie on the locus of possible reflectors which also lie in the plane of the tomogram. If the feature is visible in different tomo-graphic planes, then there is a further three-dimensional check on the geometry. In a similar manner, the crosshole reflection data is checked to see if it is consistent with the location and orientation of the zone.

As with most geophysical techniques, radar is most powerful when it is asked to detect changes in the system. For this reason, radar tomography has been used both before and after the injection of saline water into the rock. The saline increases the electrical conductivity of the hydrologically conductive features and as a result the difference tomogram highlights these features dramatically.

3.2. Seismic Methods

The transmission and attenuation of seismic waves through rock depends upon the elastic parameters of the rock which depend on the rock type, density, porosity, state of stress and strain,

temperature, and fluid saturation. As recent research shows (Pyrak-Nolte et al. 1990), high-frequency seismic wave propagation is also very sensitive to fractures in the rock. Seismic tomography can, therefore, be used to detect changes in the condition of the intact rock mass, to locate major preexisting and new fractures as well as to infer overall changes in the character of these fractures. The methods that can be used for these studies use either sources on the surface and detectors in a borehole (referred to as Vertical Seismic Profiling, VSP), or in cross-hole configuration with both sources and receivers in boreholes.

The greatest effort by far in imaging the solid earth using seismic techniques has been exerted by the petroleum industry. Literally, billions of dollars have been spent in developing and applying the surface seismic reflection profiling method and the more recently developed techniques for Vertical Seismic Profiling (VSP). In both of these methods, an energy source at the surface of the earth transmits seismic waves into the earth, and the resulting elastic wavefield is measured at the surface, or, for VSP, by sensors in a borehole. The image resolution of these techniques is limited by the amplitude and frequency content of the seismic waves, and by the level and complexity of the ambient and signal-generated noise fields. With surface sources, the heterogeneous, weathered surface layer, tens of meters thick, severely limits the high frequency content and coherence of the input signal. VSP solves this problem in part, by placing the receivers beneath the highly attenuating and variable surface, such that the signal does not have to pass through the surface layer twice. Also in VSP the wavefield is recorded with a vertical array in the borehole, so that upgoing and downgoing waves can be identified and separated. Another limitation of the surface-based techniques is the inability to surround the target with sources and receivers, as is done in the case of medical tomographic imaging. Given these fundamental problems, enhanced resolution has come mainly from improved signal processing techniques and data acquisition methods. A good review of these techniques can be found in Robertson and Fisher, 1988.

Fundamental imaging limitations can be addressed by incorporating the properties of the secondary (S) and the converted waves (P to S, S to P) that are generated in the earth. This

approach is particularly well suited for VSP applications where the primary (P), secondary (S), and converted waves can be examined directly. In recent years the use of S-waves has become common, particularly in defining anisotropy and fracture content of rock. Fracture detection using P- and S-waves with VSP methods (Stewart et al., 1981), is increasingly demonstrating that the full potential of VSP requires 3-component data (Majer et al., 1988a and 1988b). Douma (1988) gives an excellent review of crack-induced anisotropy and its effect on seismic waves. Crampin (1978, 1981, 1984a, 1984b, 1985) also stresses the importance of 3-component data in VSP work. Others have investigated the phenomenon of shear wave splitting due to S-wave anisotropy (Leary and Henyey, 1985).

The usual approach to modelling shear wave splitting is to express seismic wave propagation in terms of effective moduli. In this way, the analysis is independent of frequency and without loss, unless the moduli include imaginary terms. An alternative approach is to treat fracture interfaces as a boundary conditions in the seismic wave equation, across which seismic stress is continuous but seismic particle displacements are discontinuous (Schoenberg 1980, 1983). The ratio of the stress to displacement across the interface is the specific stiffness which defines the elastic properties of the fracture. For a completely elastic system, this stiffness theory results in frequency-dependent reflection and transmission coefficients for each interface as well as a frequency-dependent group time delay. Using multiple, parallel displacement discontinuities and ignoring converted and reflected waves, expressions derived for transmitted wave amplitudes and group velocities show that these depend on frequency, angle of incidence, and polarization in the case of shear waves (Pyrak-Nolte et al., 1990). In the stiffness theory, the thickness of a fracture is assumed to be zero, so the fracture thickness can be much less than the seismic wavelength and still have a detectable frequency-dependent effect on the seismic wave. On the other hand, the lateral extent of a fracture would still affect seismic resolution.

Water has a significant effect on the propagation of seismic waves. As a rock is saturated, or dried, velocity changes of 20 to 30 percent are seen in relatively unconfined samples. A theoretical example of this is shown in Figure 3.1, taken from the work of Mochizuki (1982). There is lit-
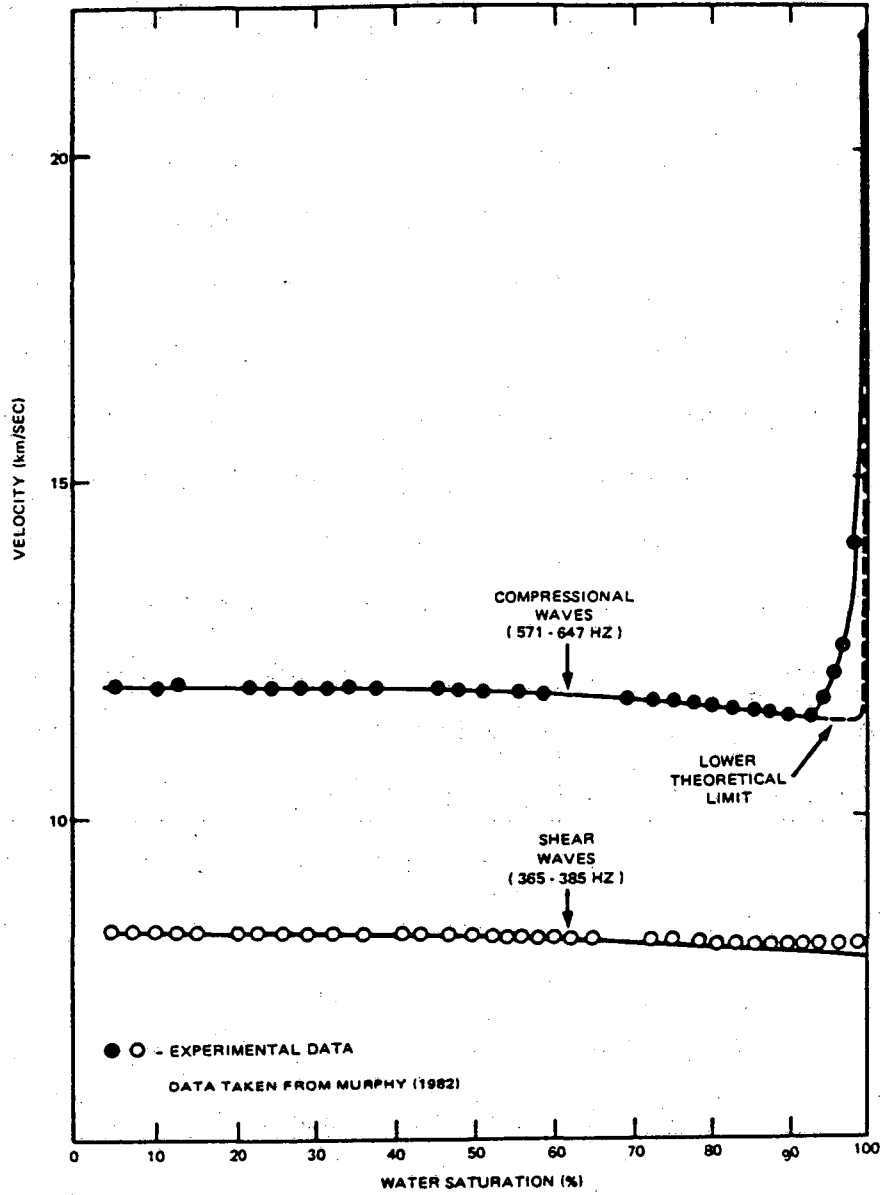
XBL 8910-3853

Figure 3.1. Velocity changes as a function of saturation.

tle dependence on saturation up to about 90% and then a dramatic rise in compressional wave velocity occurs during the very last stages of saturation. This is in marked contrast to the effect of saturation on electrical conductivity where there is a dramatic decrease in resistivity from zero to about 50% saturation and not much change after that. The attenuation of both compressional and shear waves is strongly affected by saturation as shown in Figure 3.2. These results, reported by Ito et al. (1979) show attenuation, here characterized by the inverse of the quality factor, Q, for dry, partially saturated, and fully saturated rock. The attenuation is most pronounced at low confining stress. There is a very different relationship between Q and saturation than between velocity and saturation. This illustrates the need to study attenuation as well as velocity in any seismic experiment to determine the fluid content in a rock mass. Also, water plays a crucial role in the generation of pore pressure changes which will significantly affect the rate and generation of acoustic emissions microseismic events, especially in the presence of thermal loading.

This overview would be incomplete without a brief mention of the use of natural or induced sources in seismic imaging. Natural acoustic emissions and microearthquakes can be very useful for defining subsurface properties. The location of the seismic energy release is often diagnostic of faults, or fluid injection processes. With enough activity, the sources can also be used to image the structure. Numerous examples exist of imaging the earth using earthquakes, from whole-earth scale to kilometer scale.

Beyond VSP lies the emerging crosshole technique. It offers the most promise for increasing resolution significantly. The advantages gained by placing the source in a borehole are the additional spatial coverage obtained for image construction as well as the elimination of the attenuating surface layer from the source receiver path.

3.2.1. Seismic Tomography

With the advancement of medical transmission tomography (Slaney and Kak, 1985, Huesman et al., 1977, Mersereau and Oppenheim, 1974, etc.), applications spread quickly to geophysics, spawning work in seismic ray transmission tomography. Diffraction tomography in acoustic media and electromagnetic ray tomography in a electrically resistive media have followed
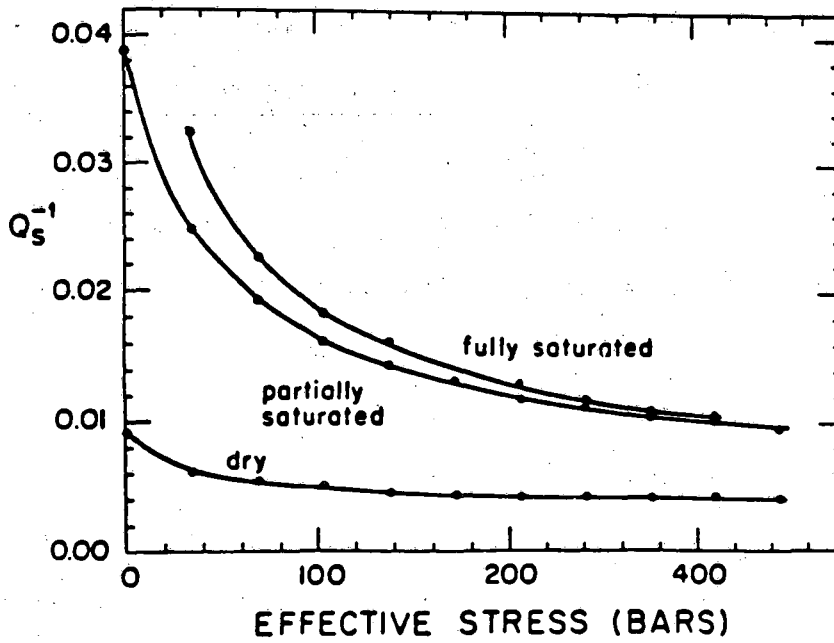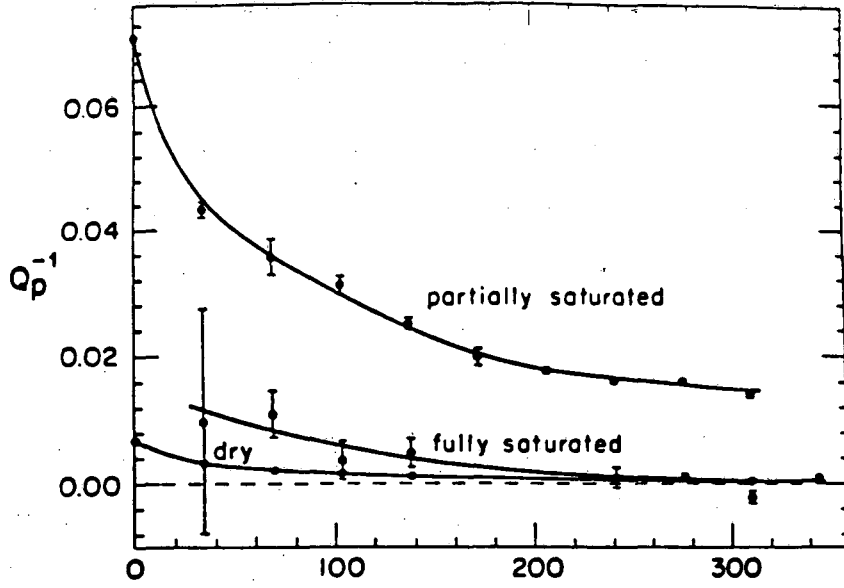
XBL 8910-3854

Figure 3.2. Attenuation as a function of saturation.

(Peterson, 1986, Bois, et. al., 1972, Dines and Lytle, 1979, etc.). Experience in VSP, microearthquake studies and tomographic surveys (Daley et al. 1988a, Daley et al. 1988b, Majer et al., 1988a, Majer et al. 1988b, Majer et al. 1988c, Foxall and McEvilly, 1988) has led us to conclude that a significant advance in imaging technology must combine new data manipulation capabilities and tomographic imaging methods, using new borehole sources and receivers.

Transmission tomography uses only the travel times and amplitudes of P-and S-waves. Either of these data sets are inverted to obtain the spatial distribution of medium slowness and attenuation. The data in a cross-hole survey are obtained as shown in Figure 3.3. The usual method of inversion is some form of iterative algebraic reconstruction algorithm, based on a back-projection method. The section of earth to be imaged is divided into many pixels of constant physical properties. As the waves pass through each of the pixels, the amplitudes and velocities are dependent on the pixel properties and we assume that the contribution of each pixel can be deduced by back-projecting the rays as indicated in Figure 3.3. It follows that a data set consisting of many rays crossing at all angles may be jointly back-projected to yield an estimate of the distribution of velocities in each pixel needed to produce the observed travel times. The attenuation properties of each pixel may be determined in a similar manner, using the amplitude information.

Algebraic reconstruction techniques (ART), developed for this problem, work well only in media that have small contrasts. These techniques are iterative in nature, where one equation, i.e. one ray, is analyzed at a time and the pixel values are continually updated. ART algorithms give exact solutions if the ray coverage is adequate, the ray lengths consistent, the ray paths determined exactly, and with no measurement errors. This is never the case. Ray coverage is usually 2-sided, 3-sided at best, with the bounds determined by the rectangular area defined by the boreholes and the surface, and with the surface measurements often of much poorer quality than the borehole data. This geometry results in incomplete coverage and ray lengths. True ray paths are curved, and they may be determined iteratively along with the pixel values, but straight ray paths are usually assumed. Measurement errors remain a source of inversion uncertainty.
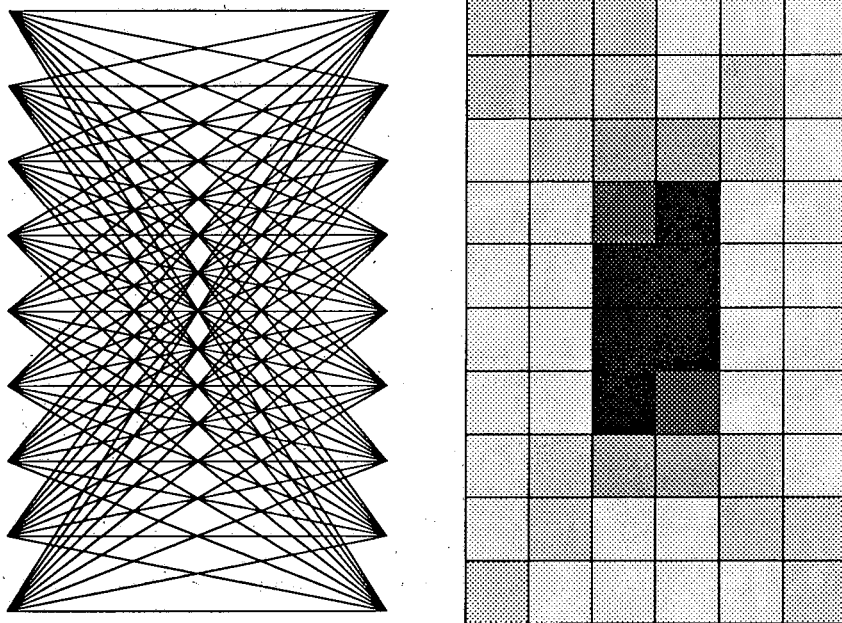
ESD-9101-0084

Figure 3.3. Back projection of rays to obtain the contribution of each pixel.

Increased resolution will come primarily through the elimination of inversion artifacts such as smearing, and from the use of more realistic 3-D ray paths. Smearing is caused by a number of problems, including inadequate angular coverage and sampling, assuming straight rays (or any improper ray path), and errors in travel time and station location.

Diffraction tomography for seismic applications is discussed by Devaney (1984) and Wu and Toksoz (1987), and diffusion tomography for the electromagnetic case is being developed at LBL (Zhou and Morrison, 1988). Diffraction tomography (acoustic case) and diffusion tomography (audio frequency electromagnetic case) differ from ray tomography in that they use the full wavefield rather than the high-frequency approximation to the wavefield, and we refer to these methods as full-wavefield tomography. Each method has distinct advantages, and we believe the optimal approach in a particular application will always be a combined use of techniques. The applications of full-waveform diffraction tomography are not as extensive as for ray tomography, but the potential developments may prove more valuable than for ray tomography. In diffraction tomography, less spatial coverage of sources and receivers is needed to obtain resolution equivalent to ray tomography, because reflected and scattered waves are used in forming the image.

Figure 3.4 shows a numerical example of diffraction tomography using data generated by a computer program that calculates the exact 2-D response of a model, in this case a fracture zone in a 2-D medium (Tura, 1990). The inversion is done at 25 frequencies from 2440 to 5490 Hz with 122 Hz intervals, and the results are averaged. The background velocity is 5500 m/sec; the velocity of the inhomogeneity is 4500 m/sec. Forty sources and forty receivers are used with a 0.5 m separation. The area between the boreholes is discretized into 20 by 40 pixels. While the back-propagation algorithm for diffraction tomography is computationally efficient and easy to implement, the inverse Laplace-Fourier transform representation of the object function for the diffusion case gives the convenience in studying array arrangements, and the constrainted least-squares reconstruction provides the necessary stability.

The original theory for diffraction tomography was developed for the 2-D acoustic case.
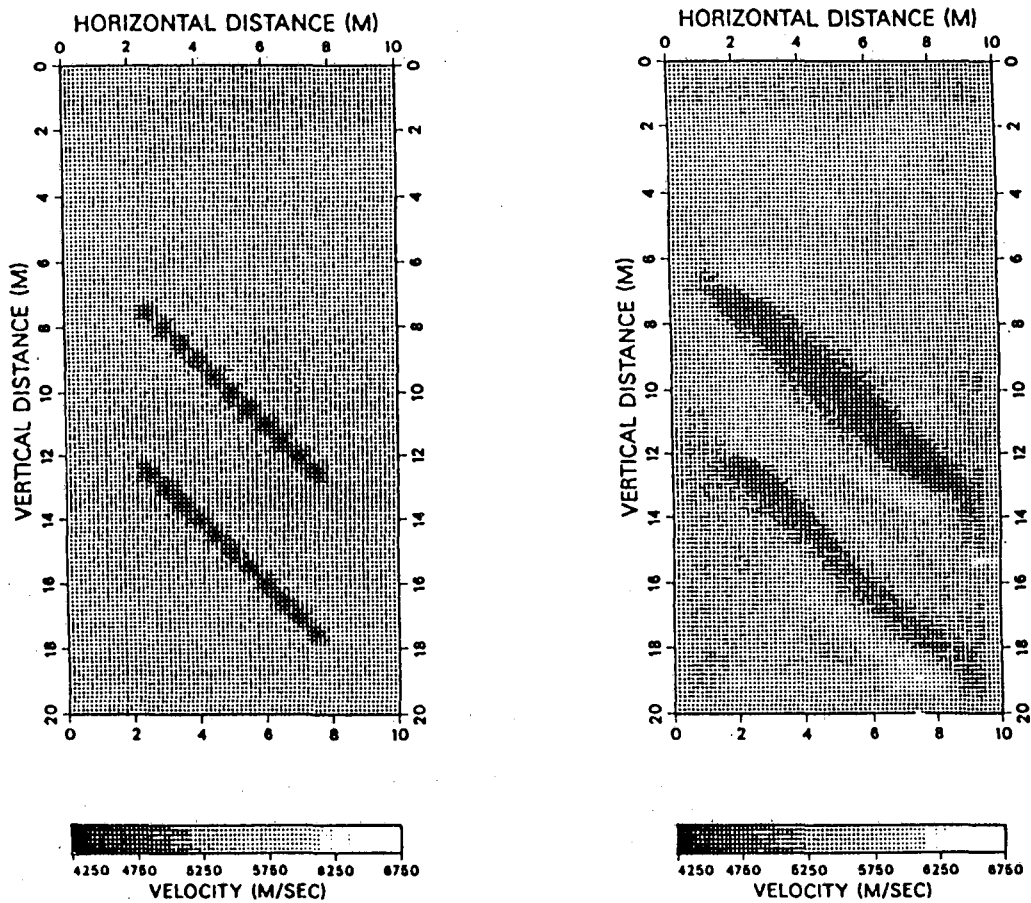
Figure 3.4. (a) Numerical example of seismic response. (b) The input model used to generate the wave form data which is inverted to obtain the image.

The method also uses the Born approximation for the necessary Green functions. Making use of synthetic simulations, we have investigated this type of solution rather extensively and have developed an understanding of how the results are influenced by various factors such as geometry, noise, separation of primary waves, and free surface effects. The results of these simulations have all been quite positive, leading to the general conclusion that basic diffraction tomography is a powerful robust method, however, questions remain regarding the practical implementation of the method in a field situation.

3.3. Example of Fracture Imaging from FRI Using Seismic Transmission Tomography

During the past three years LBL, as part of the USDOE cooperation with NAGRA has been carrying out the Fracture Research Investigation (FRI) in the Grimsel Rock Laboratory (Majer et al., 1990). The motivation for the FRI project at the Grimsel Rock Laboratory was to improve our abilities to use seismic imaging as a tool for characterizing fractured rock, particularly for the purpose of hydrologic analysis. We chose a fracture zone which was clearly present, hydrologically active, and accessible so that we could test, calibrate, and improve our abilities to image and characterize such a feature with seismic tomography.

Four other studies were conducted by LBL in association with the seismic experiments (Majer et al., 1990). A detailed geologic investigation provided the appropriate background and insight for interpretation of the tomograms. Geomechanical studies allowed controlled measurement of the rock and fracture properties. A limited number of hydrologic tests were used to check the visual observation that the fracture zone was hydrologically active and to see if other features marked by seismic anomalies might also conduct fluid. Finally, we tried to modify the fracture zone properties by inflating the fracture, measuring the stiffness and permeability change *in situ*, and seeing if we could simultaneously detect any change in the seismic response.

Figure 3.5 shows schematics of the FRI site. Two 21 m long, parallel boreholes 10 m apart connect two parallel drifts in the laboratory, the access drift and the laboratory tunnel. The two drifts and boreholes form a 10 by 21 m area. The objective of the FRI experiment was to investigate fundamental properties of seismic wave propagation in a fractured rock with known
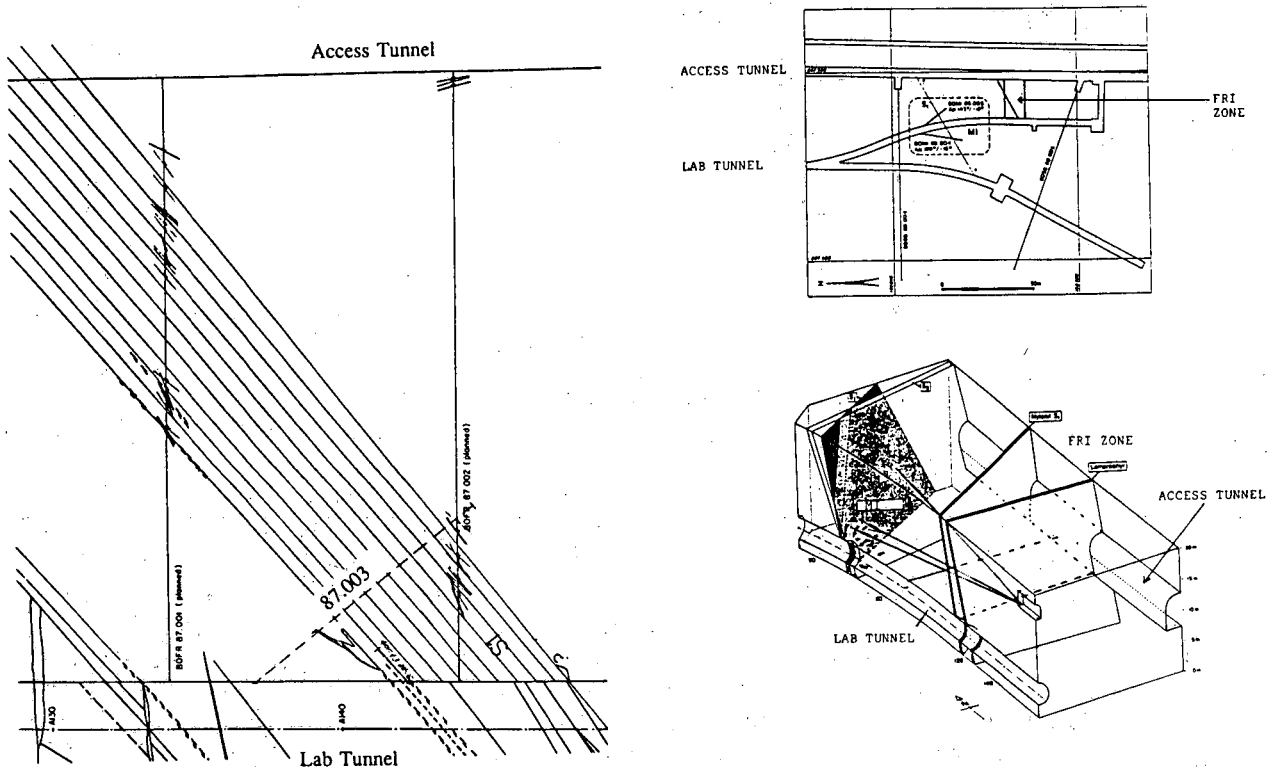
Figure 3.5. (a) Geologic plan view of FRI site. (b) Schematic of FRI zone and Grimsel Test Facility. (c) Perspective drawing of the FRI site.

characteristics in order to improve and develop imaging of fractured rock.

The dominant feature in the FRI site is a densely fractured mylonitic shear zone crossing the experimental area. The boreholes were drilled to intersect this fracture zone as well as other structural features as shown in Figures 3.5a and b. Boreholes 87.001 and 87.002 are 86-mm holes drilled from the lab tunnel to the access tunnel to provide a means of performing crosshole seismic work, core of the fracture zone, and for carrying out hydrologic experiments. Borehole 87.003 is a 127-mm hole drilled through the fracture zone for obtaining large core for laboratory analysis and also for hydrologic testing (Majer et al., 1990). In addition to these holes, 76 shallow holes were drilled into the lab and access tunnel walls between boreholes 87.001 and 87.002 at 0.25-m spacing to allow the placement of the seismic sources and receivers.

The object of the experiments was to gather high quality P- and S-wave data across the fracture zone to determine the seismic visibility of fractures. Seismic sources were placed in the holes (boreholes 87.001, 87.002, and the shallow holes in the sides of the tunnel) and activated. The data from a three component accelerometer package was recorded at 0.5-m spacing in boreholes 87.001 and 87.002. The receiver package was also placed in the shallow holes to give complete four-sided coverage. Nearly 60,000 ray paths (X, Y and Z components) were collected in the FRI zone, at distances from 1/2 m to nearly 23 m. The peak energy transmitted in the rock was 5,000 to 10,000 Hz, thus yielding a wavelength of approximately 1 to 0.5 meters in the 5.0 km/sec velocity rock. Two surveys were completed, one in 1987 and one in 1988. The 1987 and 1988 experiments were essentially similar, but an improved source and different clamping was used in 1988 which resulted in a higher received frequency content in 1988.

After the data were collected and acceptable first arrival time-values were obtained, the travel times were inverted using an algebraic reconstruction technique (ART). A pixel size of 0.25 m, was chosen because this was the size of the smallest anomaly we expect to see given the wavelength of 0.7 m and station spacing of 0.5 m. Figure 3.6 shows the results of inverting the 1987 data without correcting for anisotropy. In some cases, correcting for anisotropy has little effect on the final image, however, in this case we knew that the severe foliation of the rock could

produce seismic anisotropy. Therefore, we also made a correction for anisotropy in both the 1987 and 1988 data.

The main features identified in the 1987 results without anisotropy corrections are the low velocity zones adjacent to the tunnels, assumed to be damaged zones, and the large shear zone (Feature A) extending from the middle of borehole 87.001 to the AU borehole 87.002 intersection (Figure 3.6). Feature B (an anomaly roughly orthogonal to Feature A) and Feature C in the south of the area are also visible. Figure 3.7 is an image that was produced using almost the entire 1988 data set without anisotropy corrections. The differences between the 1987 and 1988 results are:

(1)   There is little evidence of the extensive 1987 damaged zones in the velocity tomograms of the 1988 data. Also, the average velocity values in the 1988 field are higher.

(2)   The prominent shear zone observed in 1987 (Feature A) is shown as a single strong low velocity zone about two meters wide. The corresponding zone in the 1988 results consists of two or three very thin (<0.5 m thick) zones which become discontinuous at about four or five meters from the laboratory tunnel.

(3)   Feature B was partially masked by the low velocity zone on the edges in the 1987 result is very prominent in the 1988 case. This feature extends from near the intersection of the access tunnel and borehole 87.002 intersection to the middle of 87.001 and is, in fact, the dominant feature of the 1988 results.

(4)   Feature C was more prominent in 1987 than in 1988.

As mentioned earlier, experience at Grimsel has shown us that the Grimsel granite may be highly anisotropic. Image improvement may be achieved by removing the background anisotropy from the travel times (Johnson and Peterson, 1987). The P-wave anisotropy may be approximately represented as

$$V_p^2 = A + B\sin(2\phi) + C\cos(2\phi) + D\sin(4\phi) + E\cos(4\phi)$$

where ϕ is the angle of direction of propagation. A function of this form is fitted to the data
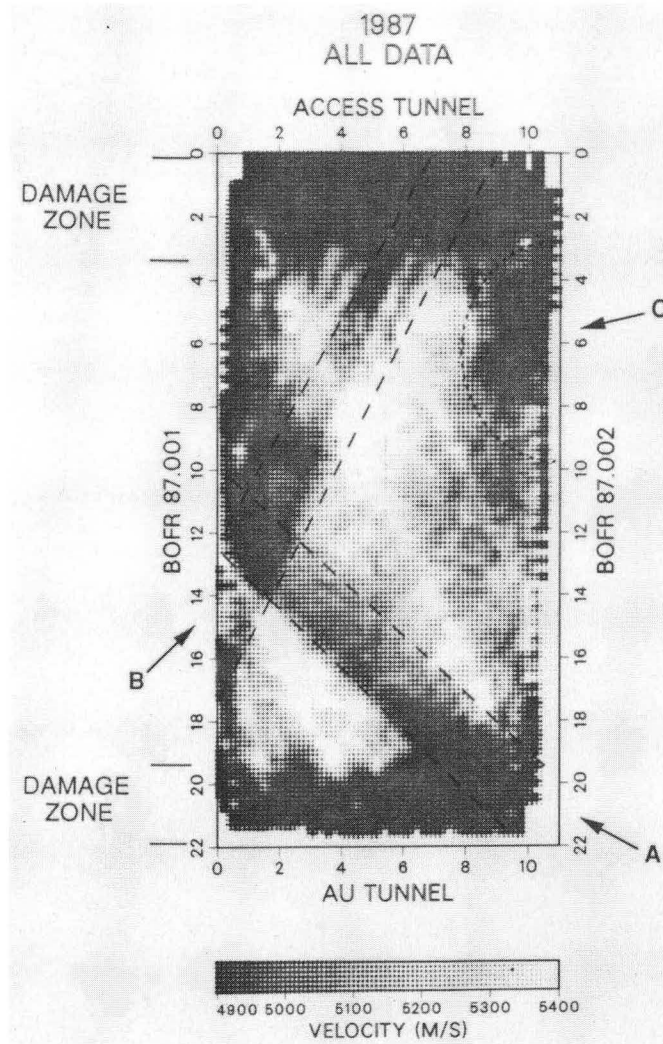
Figure 3.6. Tomographic image of FRI from 1987 survey, no anisotropic correction.
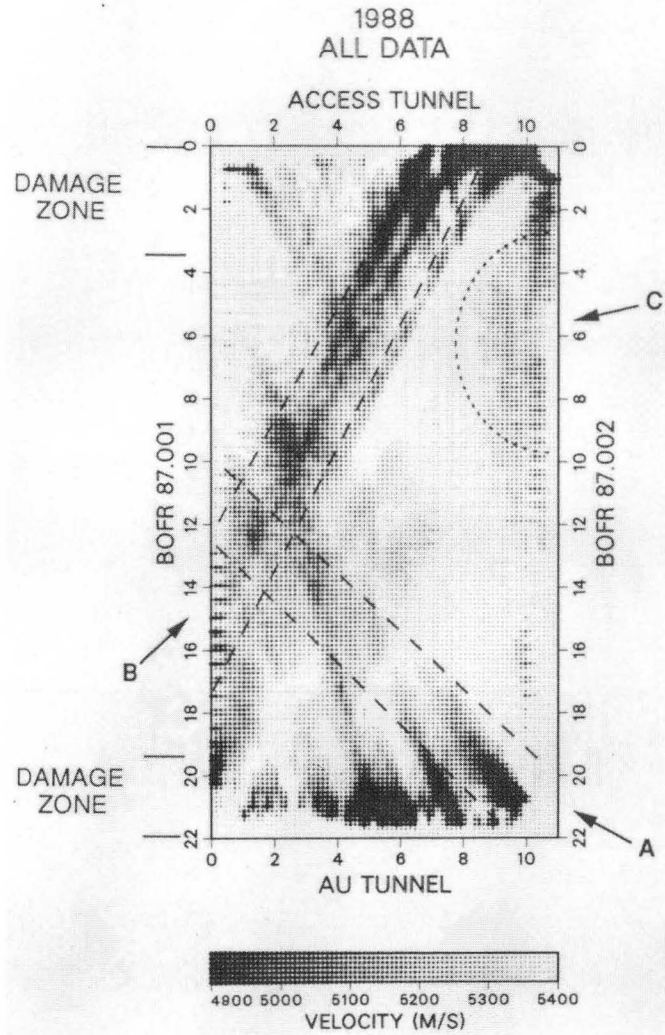
Figure 3.7. Tomographic image of FRI from 1988 survey, no anisotropic correction.

XBB 907-6029a

represented as ϕ vs average velocity. The coefficients A, B, C, D and E represent the strength of the anisotropy. These values may be determined in the laboratory or in the field. Because of limited sampling inherent in small samples, the laboratory values are difficult to determine and may not adequately represent the in-situ anisotropy. In the field, the same travel times gathered for the tomography may be used to determine the coefficients, or a separate test may be set up in a more homogeneous (though not more isotropic) area. In this experiment, the tomographic travel time data was initially used to obtain the coefficients for this calculation, but two problems were encountered. First, the existence of the fracture zone itself may create an apparent anisotropy even in an isotropic medium. Removing this anisotropy may be equivalent to removing the anomaly. Second, the existence of any low velocity zone associated with the tunnels or boreholes will distort the anisotropy. The damaged zones associated with the tunnels at FRI are such that the rays with high incidence angles will always pass through this zone, while the shallow angled rays will primarily travel across the borehole, through less fractured rock. This will create a false anisotropy centered with maximum value along the horizontal (parallel to the tunnels). Therefore, removing the anisotropy using the tomographic data would probably not be beneficial.

These problems were overcome by taking measurements between two boreholes on either side of relatively homogeneous material 15 m away from the experimental area. The anisotropy coefficients calculated from these values show almost 10% anisotropy in rock matrix velocity in the direction of the main FRI fracture zone which is also the orientation of the foliation. The contribution of this anisotropy was calculated and removed from the observed travel times. This consists of calculating the difference between the travel time calculated with coefficients A-E and the travel time calculated with only coefficient A, and then subtracting this value from the measured travel time (see Majer et al., 1990, for details).

The corrected travel times were inverted using the same technique as applied to the uncorrected data. When the same anisotropy corrections are used for correcting the 1987 data, interesting changes appear (Figure 3.8). The most obvious change is that the main shear zone (Feature A) is no longer a continuous feature, but instead consists of a couple of large features,
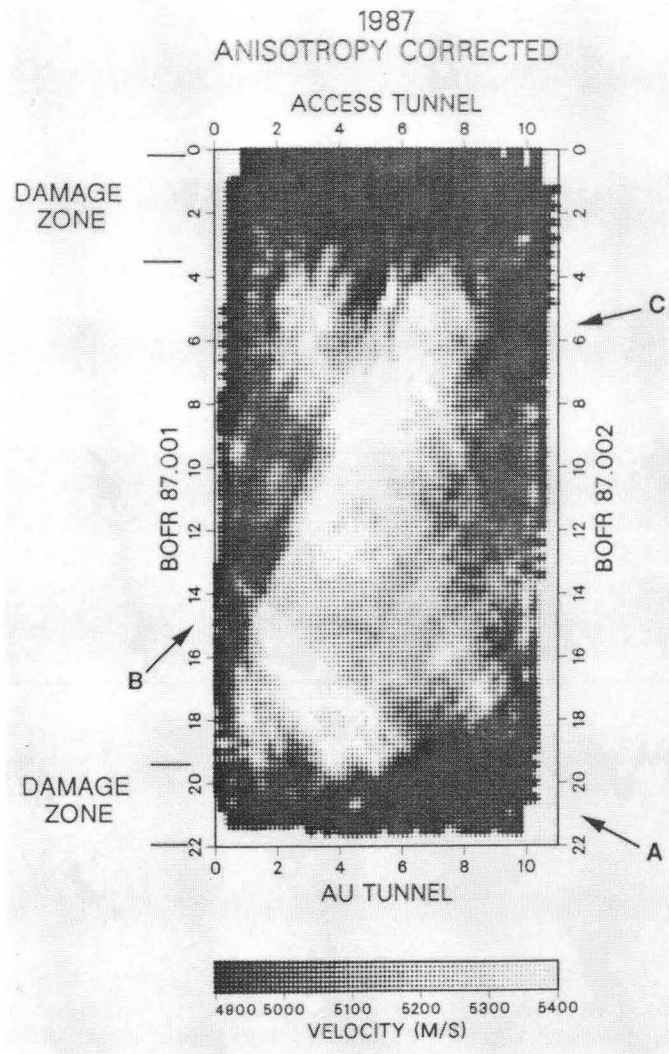
Figure 3.8. Tomographic image of FRI from 1987 survey after anisotropy corrections.

the largest corresponding with a similar feature seen in the 1988 results. On the other hand, the feature extending from the access tunnel (Feature B) to the center of 87.001 is more continuous. Also, the large low velocity feature adjacent to borehole 87.002 is more extensive.

The result of applying the anisotropy corrections to the 1988 data (Figure 3.9) is a smoother image where the anomalous zones appear to be more distinct. The inversion also appears to remove some artifacts that are produced in the original inversion. The smearing seen in the upper left of Figure 3.7 is removed, as is a strong, thin low velocity feature extending from the middle of the laboratory tunnel to the dark zone in the middle-left of the plot. The ''secondary'' fracture which parallels the main shear fracture is also eliminated.

Although not immediately obvious, after anisotropy corrections, the 1987 and the 1988 results show essentially the same features. We will first discuss how the two results compare, then analyze the best image in terms of what is known of the geology at the FRI site.

An obvious difference between the two results is the disappearance of the low velocity features near the tunnel in the 1988 results (Figures 3.7 and 3.9). The data quality was much better in 1988 than 1987. The reduced data quality in 1987 prevented the ''proper'' first arrival travel times to be picked in 1987. In some cases the first arrival was attenuated and the value picked was a pulse or two later than the time picked in 1988. This is especially true where the attenuation is greater, e.g., the damaged zones adjacent to the tunnel and in the main shear zone. The entire 1987 travel time data for sources or receivers along the tunnels are probably picked consistently late, producing a velocity reconstruction which shows consistently lower velocities near the tunnels and resulting in a lower average velocity. This means that the 1987 tomogram was essentially a mixed velocity-attenuation tomogram.

Another difference in the results is that the shear zone (Feature A, Figures 3.7 and 3.9) becomes discontinuous and less dominant in 1988. This result is of great interest because this is the zone that we were initially trying to image. Also, Feature C is less obvious in the 1988 results, again a target of the hydrologic tests. In 1987, we had assumed that we had imaged Feature A satisfactorily as a several meter wide low velocity zone. However, the 1988 inversion does not
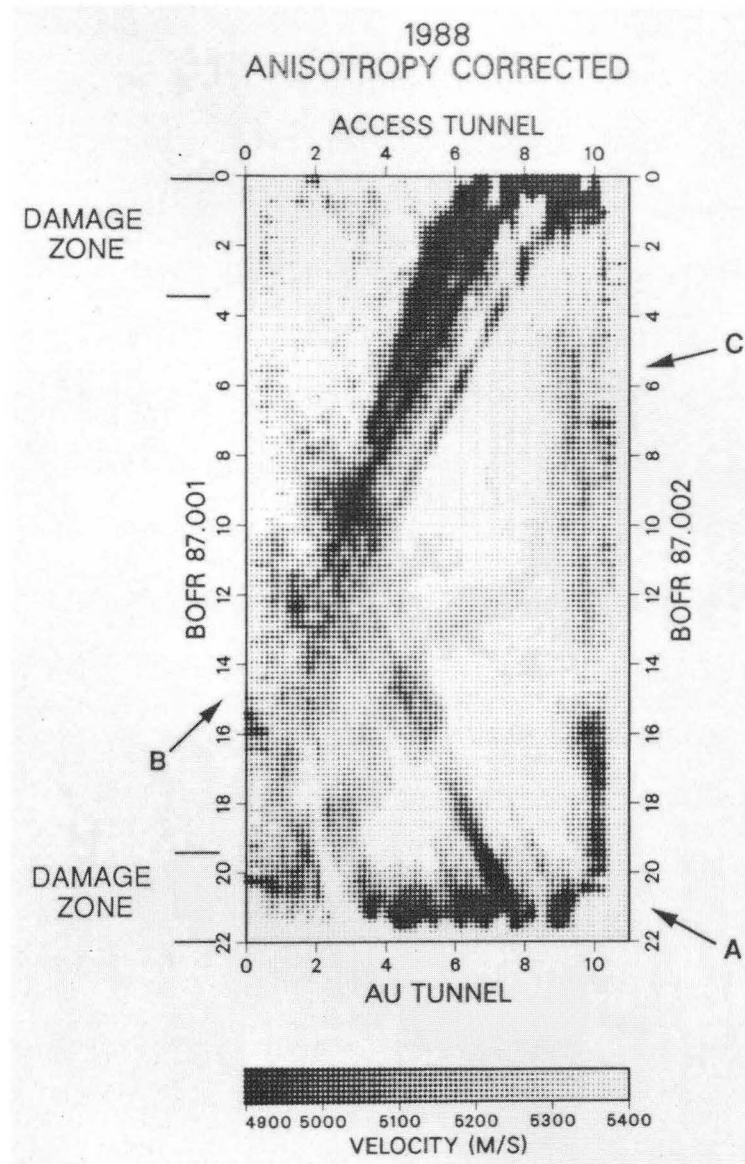
Figure 3.9. Tomographic image of FRI from 1988 survey after anisotropy corrections.

show such an extensive feature, but a thinner zone which extends to about 4 m from the laboratory tunnel. The zone dies out for a meter, then recurs as a more massive feature with variable velocity. To show the actual difference in the results, the 1988 image (Figure 3.9) is subtracted from the 1987 image (Figure 3.8) pixel by pixel (Figure 3.10). (An inversion using the differences in travel times could not be performed because slightly different stations were used for a few of the sweeps). As can be seen from Figure 3.10, there is little difference between the two images except at the tunnels, suggesting that the 1987 low velocity zone in the region of the shear zone and Feature C exists in the 1988 result, but has a slightly different form and magnitude.

Both 1987 and 1988 images show a lower velocity near the intersection of the AU tunnel and the shear zone where the excavation of the tunnel may have "loosened" the fractures. The large low velocity features toward borehole BOFR 87.001 on strike with the shear zone are also comparably imaged in the 1987 and 1988 results.

The most unexpected result from the 1988 inversion is the dominance of the low velocity feature (Feature B), which extends from the intersection of the access tunnel and BOFR 87.002 intersection to the large low velocity feature near BOFR 87.001. Extensive efforts through careful examination of the data were made to determine whether this is an actual zone of low velocity material or an artifact of the inversion process or some other kind of error. The 1987 result does show a hint of this feature protruding from the large low velocity zone adjacent to the access tunnel. However, it is not a dominant continuous feature and is obscured by the extensive damaged zone. Checking the plots of the difference between the 1987 and 1988 data, Figure 3.10, we see again that the difference is not significant. This indicates that the anomaly actually exists in the 1987 results, but it is overshadowed by the effect of the damaged zones. There is always the possibility that errors occurred in both years for several of the sweeps whose source was in this region, but this is unlikely. However, if these sweeps were removed from the data, the region of interest would not be fully sampled and the anomaly would not be adequately resolved.

The geologic map of the structures at the FRI site is shown next to the "final" 1988 tomographic image to assist in the interpretation (Figure 3.11). The interpretation of the tomographic
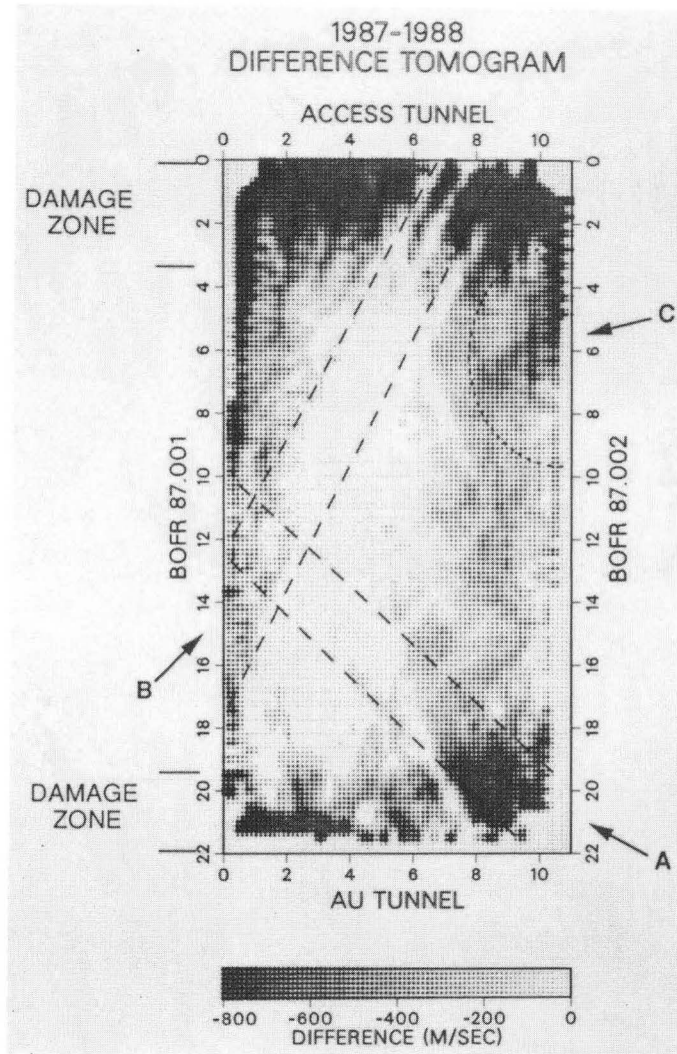
Figure 3.10. Difference between the 1988 and 1987 tomograms after anisotropy corrections.

images must include the geologic structure that is associated with each of the features that are imaged. These include:

(1)   The large low velocity anomalies observed along the tunnels in the 1987 image.

(2)   The shear zone (Feature A) was observed in 1987 as a single large low velocity zone about two meters wide. The corresponding zone in the 1988 results consists of a very thin (< 0.5 m thick) zone which becomes discontinuous.

(3)   Feature B which extends from near the access tunnel BOFR 87.002 intersection, to the middle of BOFR 87.001, and is, in fact, the dominant feature of the 1988 results.

(4)   Two strong low velocity features at the intersection of Feature B and the shear zone.

The low velocity zones associated with the tunnels in the 1987 results may be due to the initial pulse of the signal being highly attenuated. This was primarily due to a weaker source being used in the 1987 experiment. However, this does not explain why the 1988 velocity data did not resolve the damage zones, i.e., if there are damage zones with high fracture content, why did we not detect them in the 1988 velocity data? One explanation may be that the 1987 result only detected the damage zones because the initial pulse was attenuated, not slowed, and thus an artificially low velocity result was obtained by picking later arrivals. The attenuation data from 1988, however, did detect the damage zones near the tunnels. This suggests that at the frequencies we used, 5 to 10 kHz, the effect on the velocity was much less than that on attenuation. This is what the "stiffness" theory predicts (Pyrak-Nolte, 1990). As frequency increases, for a constant stiffness, the velocity or delay becomes less relative to the attenuation effect. Apparently we were at frequencies where for the stiffnesses involved, attenuation is important and delay is less important.

In the final 1988 tomogram, the shear zone appears to produce a relatively weak velocity anomaly. The zone appears, as expected, from the 1987 results, but its form is altered in 1988. Although there is a visual difference, the actual differences are not great and may be due to the better resolution obtained in 1988. The 1988 results indicate that it is likely that the zone is not a simple single planar feature and thus the permeability along the zone may also be variable rather
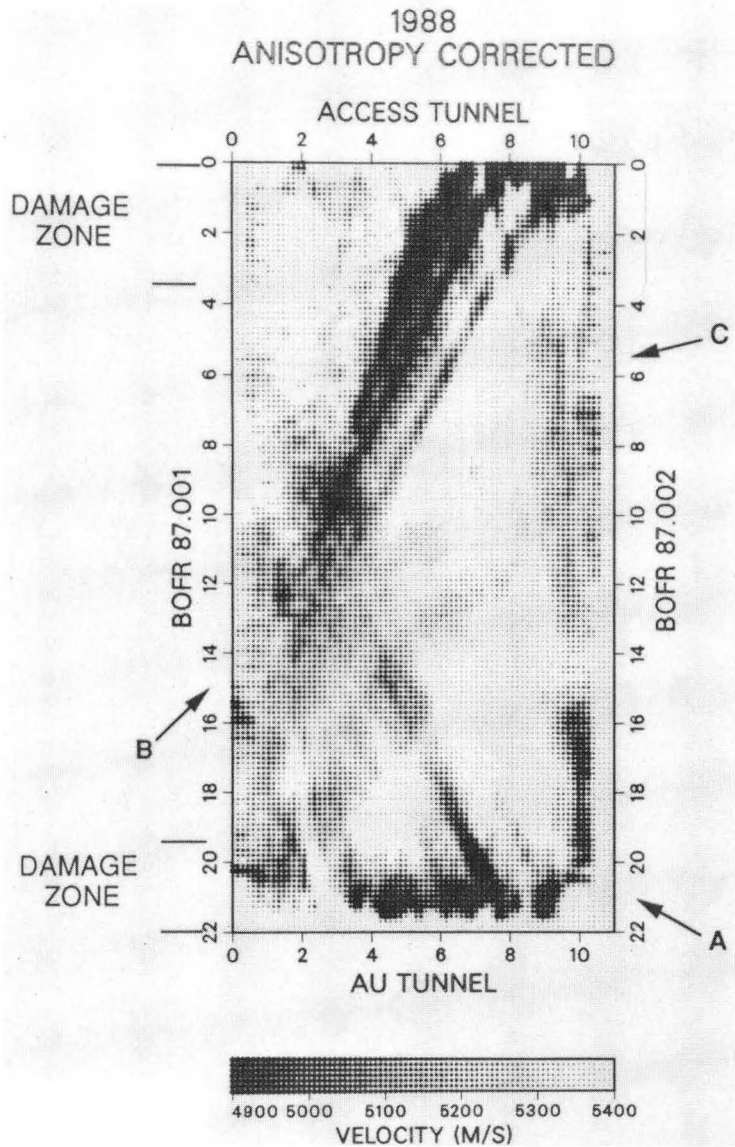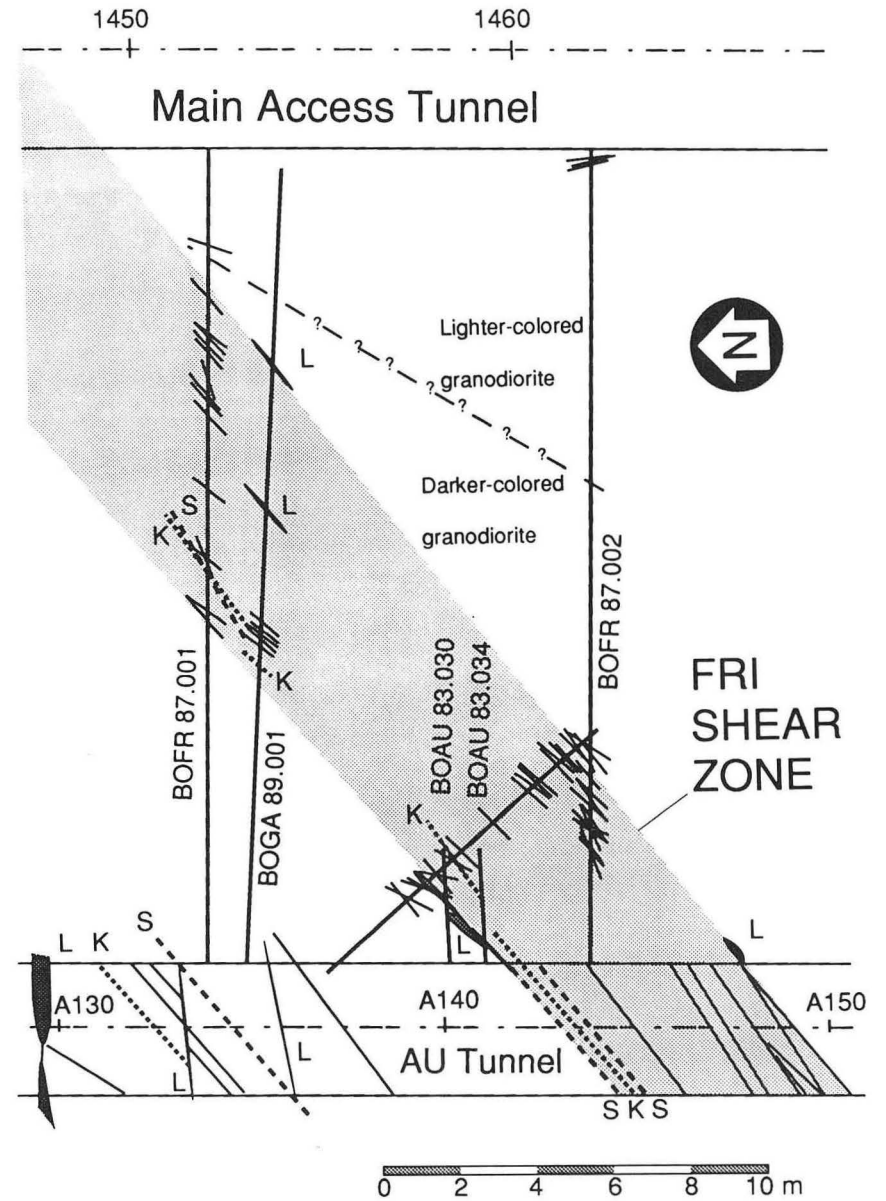
Figure 3.11. (a) The velocity tomogram for 1988 compared to (b) the geologic map of the FRI site.

than being a single well connected feature. Figure 3.11 indicates that the shear zone produces a large velocity anomaly near the AU tunnel wall, where this anomaly intersects a lamprophyre at about 4 m from the wall along the strike of the shear zone. The intersections of lamprophyres and shear zones have been observed to be areas of more intense fracturing which probably causes larger velocity anomalies. The anomaly indicates that the lamprophyre is probably discontinuous, being vertically stretched along the shear zone during deformation. After this velocity anomaly dies out, another small low velocity anomaly is encountered at about 2 m further along strike of the shear zone. This anomaly may be another piece of lamprophyre or a region of high fracturing.

The most dominant feature in Figure 3.11 is Feature B, which extends from a highly fractured area in the access tunnel to the shear zone. It is unlikely that the anomaly is totally an artifact of the inversion or due to data errors since it occurs in the results from both years. The anomaly may not actually extend to the shear zone, but may be smeared somewhat in this direction. Subhorizontal fractures and a tension fissure (not shown in Figure 3.11b) occurs where Feature B intersects the access tunnel. From geologic considerations, it is most likely that this feature is associated with a lamprophyre or an especially large tension fissure. The strike is different from the lamprophyres in the immediate area, but the Grimsel lamprophyres are not consistent in their behavior, especially when associated with shear zones. Since the geologic information about this feature is sparse, the only way to validate its presence is to drill into it. A subsequent borehole (BOGA 89.001) was drilled parallel to BOFR 87.001, but unfortunately it was several meters away from the anomaly and could not validate the prediction.

Where Feature B intersects the shear zone, Feature A, two large anomalies are also observed. These anomalies may be areas of intense fracturing, most likely due to lamprophyres intersecting the shear zone. A small lamprophyre was logged in borehole BOGA 89.001 which coincides exactly with one of these anomalies. The other anomaly coincides with a kakirite zone which also indicates a region of increased fracturing. These anomalies also suggest that there may be hydrologic communication across the shear zone in this region.

Except for Feature B, all the anomalous velocity zones are coincident with geologic structures. Feature C is still not verified, but the core suggests a different rock type, lighter granite, rather than fracturing may be the cause of this feature. The light color may reflect hydrothermal alteration of the granite, perhaps by fluids migrating along tension fissures. The two low velocity anomalies near borehole BOFR 87.001 where Features A and B intersect were interpreted as zones of intense fracturing, likely due to the presence of lamprophyres when borehole BOGA 89.001 was drilled, this interpretation was validated. Though the geologic information determined the possibility of such fractured regions, these fractured regions could not be located by core data alone. In the case of Feature B, it is always possible that it could be an artifact caused by some data error. However, there is no basis on which to reject the hypothesis that is real, it is observed in both the 1987 and 1988 results. There is little doubt that some anomalous zone exists near the tunnel wall, probably a tension fissure.

The results of the seismic field work to date at Grimsel, indicate that the original premise of using P- and S-waves for mapping fracture content is valid. The main fracture zone in the FRI site was detected using P-wave tomography. The S-wave was attenuated so strongly by the fractures that it could not be detected. However, given a strong enough S-wave source, then one might find that S-wave data would be even more sensitive to fracture content than P-wave data. Other low velocity zones in the FRI area were also detected, the most significant being the velocity anomalies associated with the stress relief at the tunnel walls and Feature B. There were also other zones of low velocity detected in the FRI zone, most notably the low velocity zone (Feature C) extending along borehole 87.002 from the access tunnel approximately 8 meters. This may be due to small fractures, or as laboratory work suggests, a difference in the rock type. The core does not show significant fracturing in this zone, but the core velocities are lower for this type of rock than for the rock in the "light zone".

Possible reasons for the differences between the 1987 and 1988 tomograms can be identified through geomechanical studies aimed at relating the mechanical stiffness of a fracture to the behavior of acoustic waves passing through the fracture (Majer et al., 1990). Values of

fracture stiffness were estimated using the in-situ deformation measurements. For these values of stiffness, the difference in the 1987 and 1988 dominant frequencies would result in significantly more delay through the fracture in 1987 than in 1988. Thus, the stiffness theory alone could easily account for the smaller anomalies in 1988. The 1987 seismic results were used to guide the well test design. The hydraulic tests that were conducted confirmed the hydrologic significance of the kakirite-bearing fractures in the FRI zone identified by the seismic tomography. These are discussed in Section 5. Other tests indicated the possibility that leakage out of the plane of the fracture could occur along secondary features that were seen as anomalies in the tomograms. Hydraulic storativity of the kakirite bearing fractures was independently estimated for the FRI fracture using the geomechanics measurements. The integration of all the information has provided a powerful approach to characterization.

3.4. Summary

Geophysical techniques provide non-invasive ways to evaluate rock properties within a body of rock. Seismic and electromagnetic techniques have been developed to sophisticated levels for this purpose. They can help project major features identified at the surface or in boreholes and can detect subsurface structures which were not previously identified. As a result, they provide a way to check and improve the structural model of a site. Geophysical investigations complement geologic work in that they are directed at unexposed portions of the site.

Seismic techniques are useful for evaluating the elastic properties of a rock mass and its density. These depend in turn on rock type, porosity, fluid content, and fracture distribution. For example, elastic wave velocities generally increase as a function of increasing rock stiffness. For a fixed saturation, an increase in rock porosity generally will decrease wave velocity. Wave velocities generally increase with the level of saturation. Signal attenuation is related to physical parameters in a complex manner.

Electromagnetic techniques are used to sense variations in parameters such as electrical resistivity or conductivity, dielectric constant, and magnetic permeability (Telford et al., 1976). In many cases, the electromagnetic properties of a rock mass are dominated not by the

mineralogy of the rock, but instead by its water content. Therefore, the porosity and saturation of a rock mass will have relatively large effects on electromagnetic waves. This means electromagnetic waves are useful for evaluating the hydrologic properties of rock.

In particular, both seismic and electrical cross-hole tomography may be a useful technique for non-destructively imaging properties of rock over distances as great as a few hundred meters. It is important to note that tomograms must be interpreted. Perceived anomalies on tomograms do not correspond uniquely to geologic features in a rock mass. Anomalies on tomograms can correspond to a variety of geologic effects. Independent information on the geology can be used to determine which geologic features are most likely represented in the image. Second, the inversion process itself commonly produces artifacts that can be difficult to distinguish from the anomalies associated with real geologic structures.

4.0. THE USE OF INTEGRATED GEOLOGIC AND GEOPHYSICAL INFORMATION FOR CHARACTERIZING THE HYDROGEOLOGIC STRUCTURE OF FRACTURE SYSTEMS

In Section 2 we discussed the need to determine which structures in the rock dominated the hydrologic behavior and to conceptualize how water might flow within and between those structures. In Section 3, we discussed how these features might be imaged through geophysics. The purpose of this section is to show how the information gained from a combined geophysical and geologic investigation can be blended to determine the 3-D geometry (position and orientation) of the major structures which might conduct water, ie. a geometric model of the geologic structure. The geologic and geophysical contributions have different strengths and different limitations. To a large extent, a limitation in one discipline is offset by strength in the other; this is a major reason why a joint investigation can be particularly fruitful.

4.1. Methodology

There are two types of geologic information available for integration with the geophysics: geologic maps made at outcrops and underground exposures, and data from boreholes. Detailed geologic mapping is particularly effective in revealing the structural and age relationships of the fractures within a fracture zone, as well as their shapes, lengths, positions, and orientations. The maps present a system in the form of an integrated picture rather than in a series of unrelated points. Moreover, the act of mapping forces the geologist to try to interpret the mapped patterns.

Small-diameter boreholes provide the least expensive way to directly sample the geology within an unexposed volume of rock. However, there are several limitations in using borehole

data alone to construct models of fracture zones. Some problems stem from the combination of small sample size and fracture irregularity. Unless a fracture is entirely confined within a borehole core, it is essentially not possible to determine the shape and dimensions of a fracture solely on the basis of borehole records.

In interpreting borehole data, one should be aware that the orientation of a fracture zone can differ significantly from the orientation of the fractures in the zone. Figure 4.1 shows a simple example of how the same borehole fracture record can reflect entirely different fracture configurations. In one case, (Figure 4.1a), the average orientation of a cluster of fractures encountered in a borehole can be a good indicator of the orientation of the zone as a whole. However, if the internal fractures are systematically oblique to the zone as a whole (Figure 4.1b), then this approach will yield a grossly incorrect zone orientation. In the case of Figure 4.1a, the fractures are not hydrologically connected, whereas in Figure 4.1b they are. Work on the structural systematics can reveal how individual fractures are arranged in fracture zones and therefore can be extremely valuable in interpreting borehole fracture data.

Another problem with borehole data is that of "borehole bias" (Terzaghi, 1965). Because of borehole bias, boreholes of different orientations drilled through a single fracture zone may appear to encounter multiple smaller fracture zones with different orientations. Borehole bias effects highlight the importance of checking the interpretations of borehole data against independent findings wherever possible.

Geologic and geophysical investigations clearly can complement each other. Geologic investigations are well-suited to identify, locate, and characterize exposed features, but they are limited in their ability to determine how far to project known features and to detect unexposed features. On the other hand, geophysical investigations can locate unexposed features, but are limited in their ability to uniquely determine the type of geologic features they detect. A clear use of geophysical information is to help project features within a site. A key contribution of
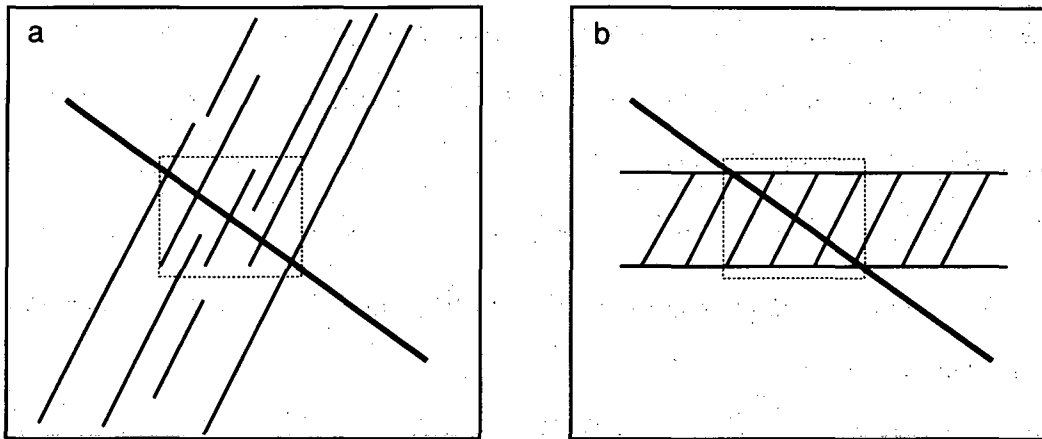
XBL 905-1898

Figure 4.1. Two markedly different fracture zones can have the same appearance where they intersect a borehole (shown in heavy line): (a) a series of joints, and (b) a fault zone. Dotted box is for reference.

geologic information is to prevent geophysical data from being interpreted blindly. If certain geologic features are known to be either exposed at the perimeter of a site or intersected within the site by boreholes, geophysical images can be interpreted with that information in mind.

Selective detailed geologic mapping is done to determine the internal systematics of the major features that are likely to exist within the site. As noted in Section 2, the detailed mapping should focus on the outcrops with the largest and most complete exposures of major structures. In cases where local exposures are of insufficient quality or size to determine systematics, it can be useful to map similar structures in analogous geologic settings.

To produce a preliminary model of the site structure, geologic structures either exposed in the site vicinity or inferred from geophysical data are projected into the site. The model is revised to incorporate the results of site-specific geophysical tests. Drill cores, core logs, and core photographs are also inspected to identify zones of abundant fractures and other structures (e.g. permeable dikes) within the site that may be important to the model. The geophysical and borehole information should be interpreted in a manner consistent with the systematics of the local structures. The model should be re-examined and refined as more site-specific information becomes available.

A model of the major geologic features can be used as the basis for a hydrologic model as shown in Section 6 in an example from Stripa. Both the gross arrangement of the major structures and the information on the internal systematics of the major structures should be considered in preparing hydrologic models. The structural information could also be used to help plan the siting of wells or boreholes for collecting hydrologic data.

4.2. An Example of Construction of a Fracture Zone Model from Grimsel

As an example of the integration of geologic and geophysical data, we summarize below our experience with data taken from the US/BK site at the Grimsel Laboratory in Switzerland (Figure 4.2). Information on the general characteristics of the major geologic structures in the

vicinity of the Grimsel Laboratory was presented in Section 2. We combine that information with site-specific data from surface and subsurface mapping, boreholes, and geophysical tomography to construct a geometric model of the major geologic structures at the US/BK site. We then examine how well this model would have predicted the flow behavior inferred from the results of difference tomography based on experiments at the US/BK site where tomographic surveys were performed before and after injection of a brine solution. Because the brine has a readily detectable electromagnetic signature, the difference between the "before" and "after" tomographic data highlights hydrologically conducting features. We can then see if the conducting features match features in our geometric model.

4.2.1. Major Geologic Structures near the Grimsel Laboratory

As discussed in Section 2, three main systems of geologic structures have been identified in the vicinity of the Grimsel laboratory: K-zones, S-zones, and lamprophyre dikes. The K-zones are steeply-dipping fracture zones that generally strike to the northwest, at high angles to the foliation of the granite, which strikes N65°E. The S-zones contain fractures that parallel the foliation in the rock. Metamorphosed lamprophyres, which are mafic dikes that contain abundant micaceous material, generally strike northwest. Keusen et al. (1989) show the distribution of these features near the laboratory through the combination of a geologic map of the surface (Figure 4.3), a geologic cross section (Figure 4.4), a block diagram (Figure 4.5), and a generalized map of the main fracture zones at the level of the Grimsel laboratory (Figure 4.6). A salient aspect of these illustrations is that many of the major structures extend to depth as roughly planar features. This is consistent with the expression of the major structures in the mountainside above the laboratory. A particularly prominent feature shown on the geologic map (Figure 4.3) is a K-zone exposed at an elevation of 2100 m above the north end of the main laboratory tunnel. The cross section (Figure 4.4) shows the lamprophyres exposed north of the BK room as being connected to this K-zone.

BOUS 85.002

L 60.00m

L 100.00m

BOBK 86.001

BOBK 85.008

BOBK 85.010

BOBK 85.006

BOBK 85.004

BOBK 85.005

BOBK 85.009

US/BK
ROOM

BOBK 86.003

BOBK 86.002

BOGS 84.041A

BOUS 85.003

L 200.00m

N

0   50m

LABORATORY TUNNEL

MAIN ACCESS TUNNEL
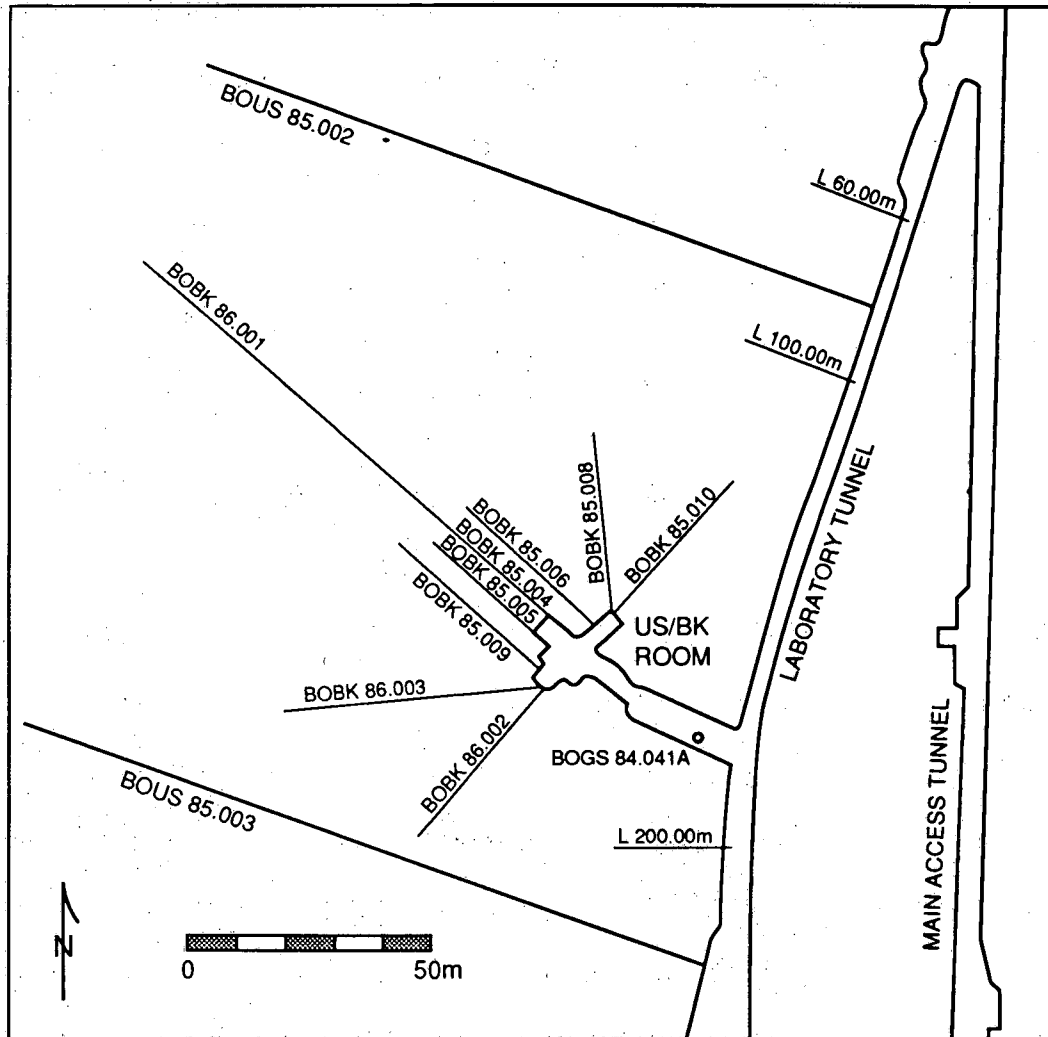
XBL 908-2746

Figure 4.2. Map showing the tunnels and major boreholes in the vicinity of the US/BK site. Boreholes BOUS 85.002 and BOUS 85.003 are considered as bounds on the site, as is the laboratory tunnel. L60, L400, and L200 mark distances (in meters) along the laboratory tunnel.
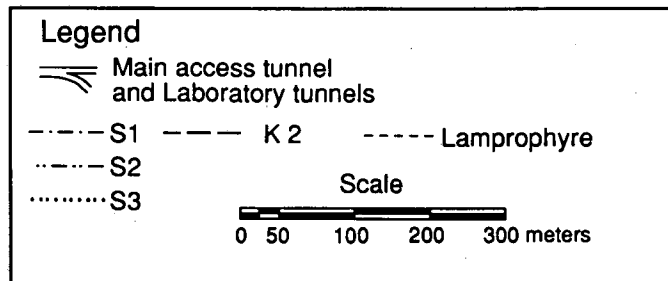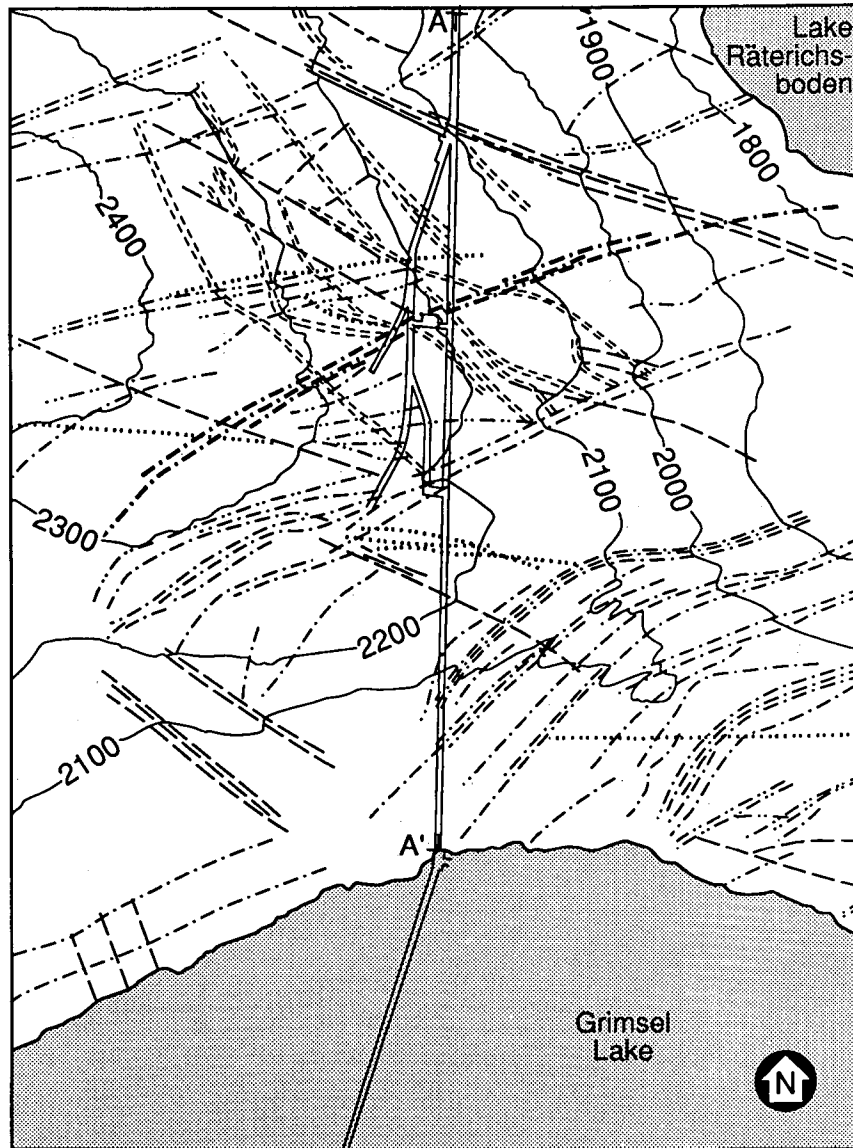
Figure 4.3. Map showing traces of fracture zones at the surface above the Grimsel laboratory. Contour interval is 100 meters. Line A-A' marks line of cross section of Figure 4.4. Lake at upper left corner of map is the Ratrichsbodensee (from Keusen et al. 1989).
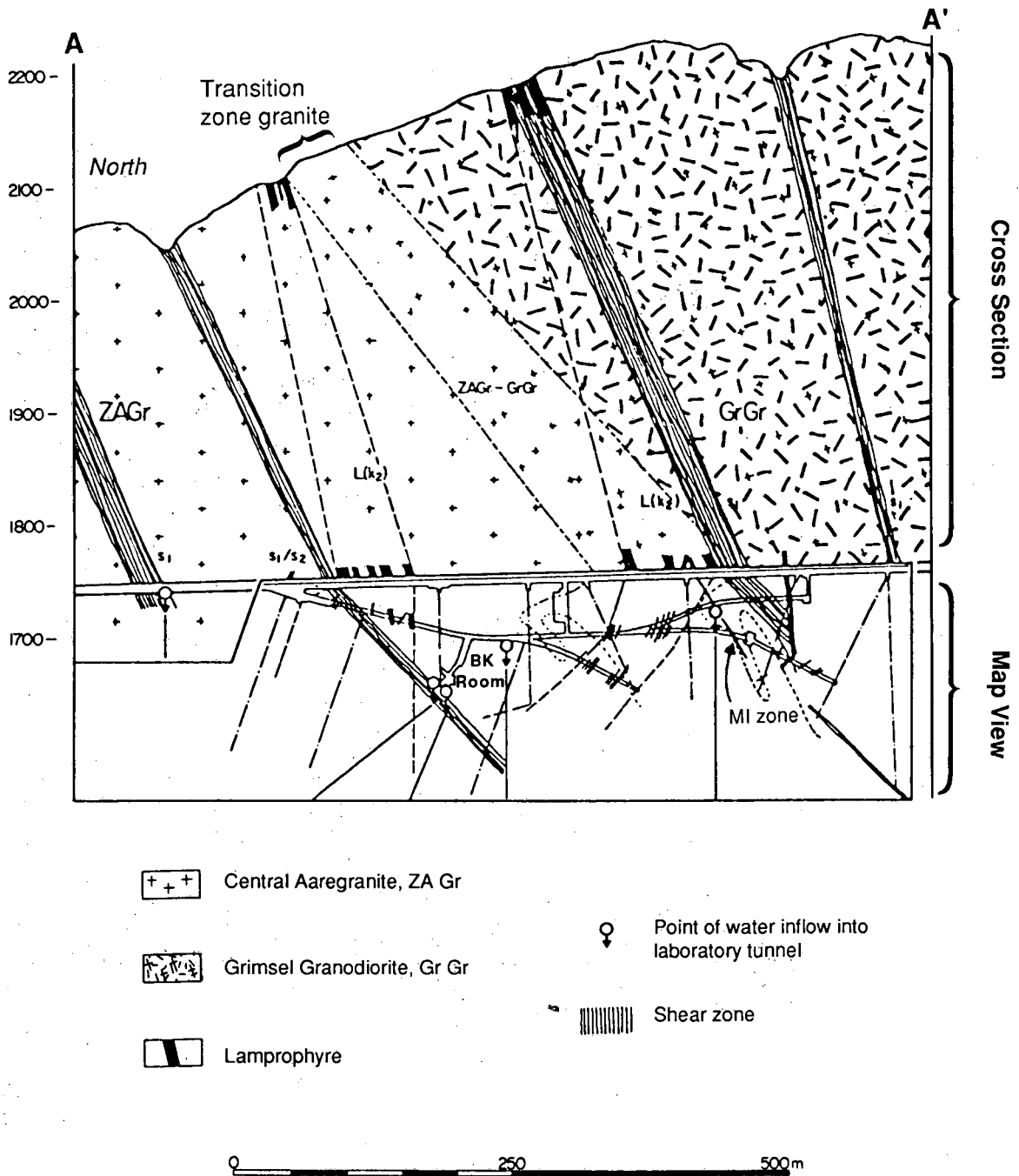
Figure 4.4. Geologic section along the main access tunnel to the Grimsel laboratory showing major fracture zones and simplified map showing major structures at the level of the laboratory tunnels. Line of cross section A-A' shown in Figure 4.3. Straight long-dashed lines in map view are boreholes (from Keusen et al., 1989).
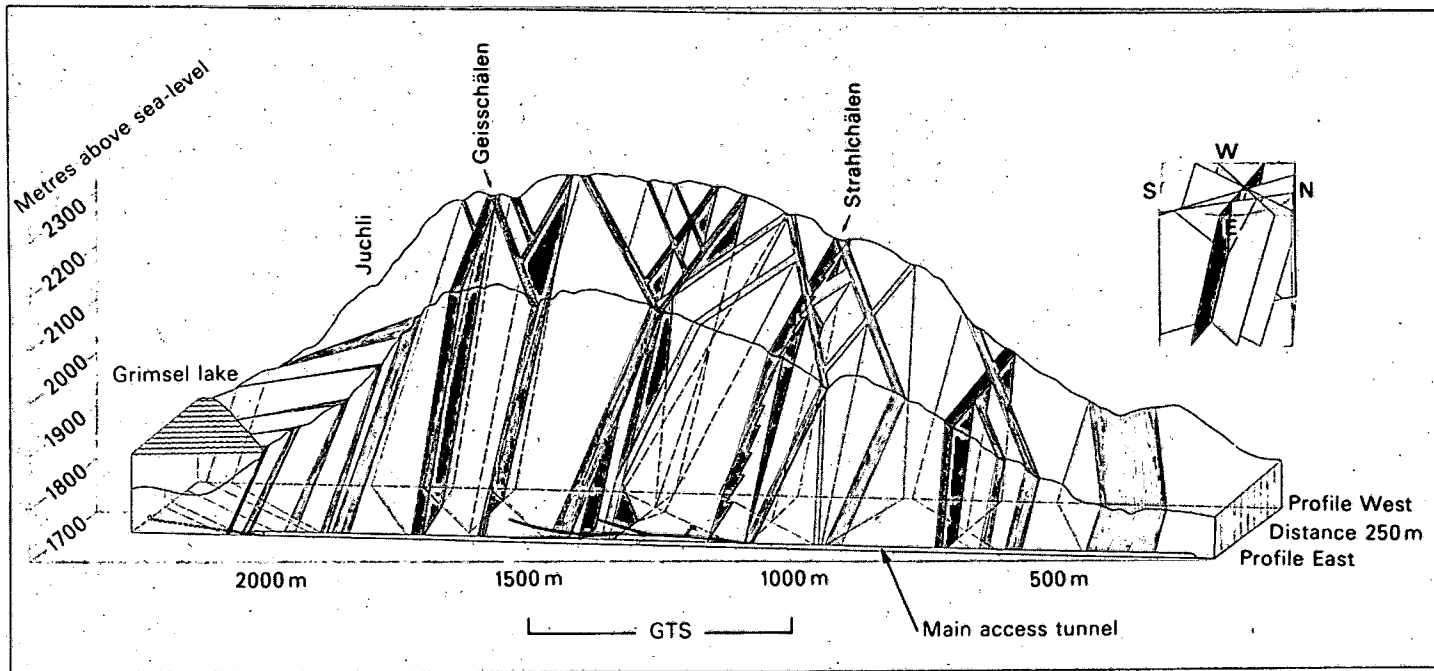
ZBB 896-5035

Figure 4.5. Block diagram showing major structures in the vicinity of the Grimsel laboratory. View is to the west. Zones shown with lined edges are S-zones. Structures marked by solid shading are K-zones and lamprophyre dikes. Numbers along main access tunnel mark distance in meters from its north entrance (modified from Keusen et al., 1989).
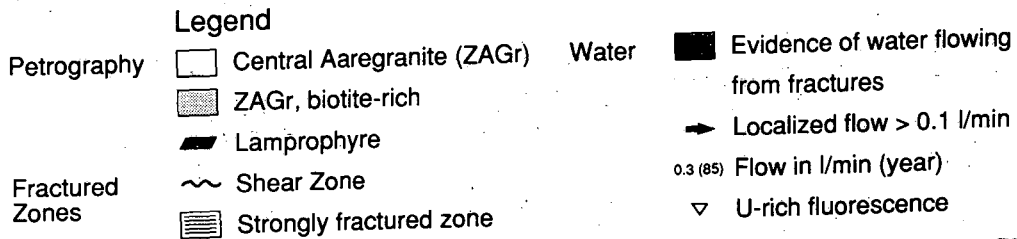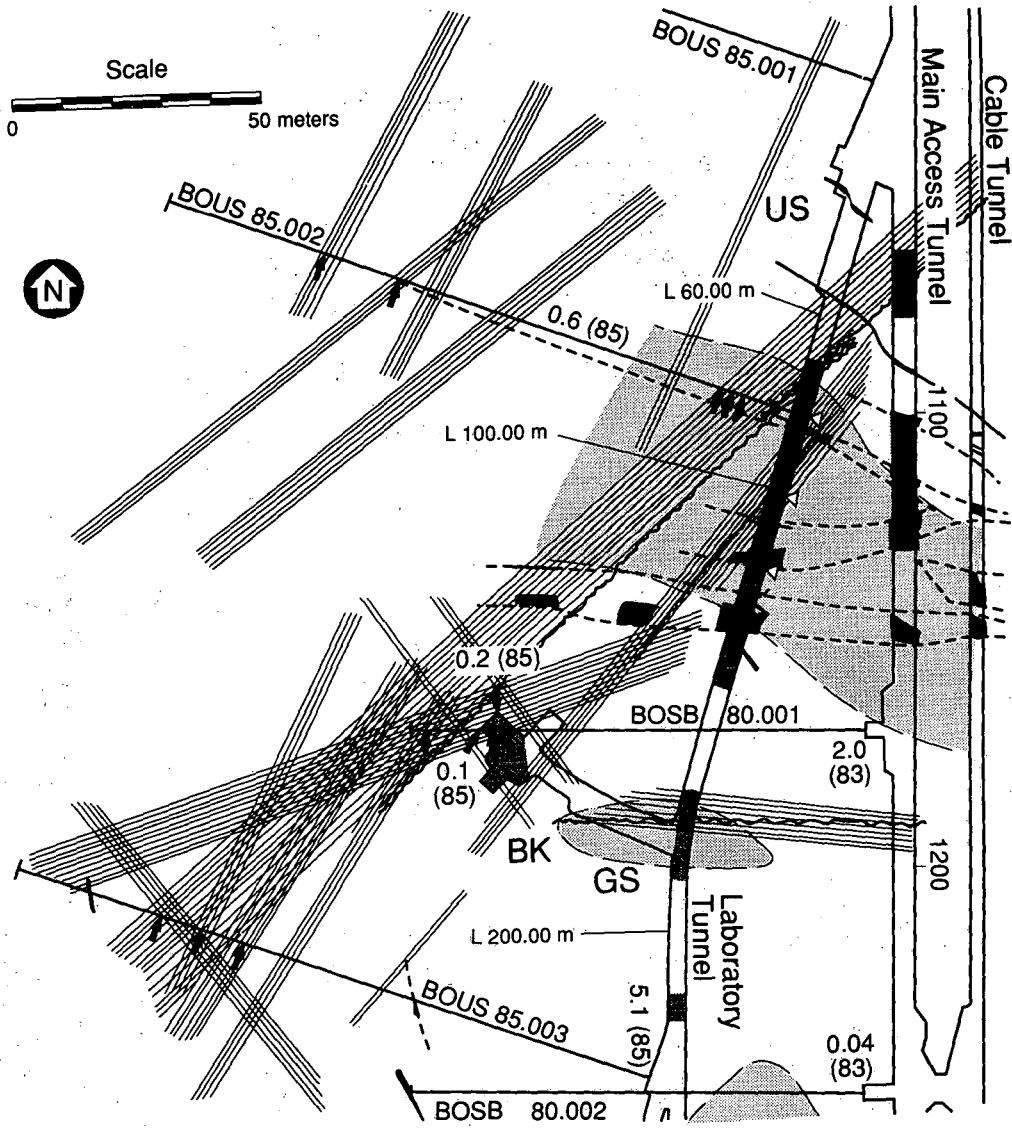
Figure 4.6. Structural interpretation of the US/BK site from Keusen et al. (1989). Numbers along main access tunnel mark distance in meters from its north entrance.

4.2.2. Geology along the US/BK Site Perimeter

Three major geologic structures that project into the US/BK site have been mapped (Keusen, et al. 1989) in the laboratory tunnel along the site border (Figure 4.6). Water drains from all these structures. A set of two adjacent S-zones strikes northeast near the mouth of BOUS 85.002. Both S-zones contain numerous northeast-striking fractures. There is evidence that there has been several meters or more of relative horizontal displacement across the northern S-zone (Martel and Peterson, 1990). Some highly deformed lamprophyres strike west between BOUS 85.002 and the BK room. Because the west-striking lamprophyres appear to coincide with a prominent K-zone mapped at the surface (Figures 4.3 and 4.4), we refer to them as K-lamprophyres. Slip along that K-zone probably was associated with deformation of the K-lamprophyres. A K-zone strikes west into the entrance to the BK room. The K-zone consists of a few prominent fractures (probably faults) that strike to the west and numerous subsidiary fractures that strike southwest.

4.2.3. Borehole Information

We took advantage of the structural systematics of the major fracture zones at Grimsel when interpreting the borehole data. From the tunnel exposures we knew that at least one or two S-zones, two lamprophyre-bearing zones, and a K-zone occurred at the US/BK site. The surface and subsurface geologic mapping demonstrate that these structures are large and relatively planar. Our detailed characterization work demonstrated that the fractures in the S-zones formed a braided pattern. Although the strike of individual S-zone fractures locally differs from the overall strike of the zone by as much as 20°-30°, the overall strike of the S-zone fractures is roughly parallel to the zone as a whole The average orientation of fractures encountered in a borehole through an S-zone should be a good indicator of the orientation of the zone as a whole. The boreholes that extend northwest from the BK room are well located to intersect S-zone fractures (Figures 4.3 and 4.6). In contrast, the K-zones consist of faults parallel to the zone linked by

fractures that strike oblique to the zone; these oblique fractures typically are more numerous than the zone-parallel faults. The orientation of the faults rather than the average orientation of all the fractures encountered in a borehole through a K-zone would best indicate the orientation of the zone as a whole.

We inspected photographs of the cores drilled around the US/BK site and located the intervals with fracture clusters, faults, and lamprophyres as the basis for projecting the S-zones, K-zones, and lamprophyres exposed at the site perimeter. We assigned an interval to a particular zone based on the location, type and orientation of the fractures in the interval. The location and orientation information was then projected up (or down) dip using the orientation of the appropriate zone to a horizontal plane at an elevation of 1730 m, the elevation of BK room, to form a map (Figure 4.7). The information could also be projected along strike to vertical planes to yield cross sections (Figure 4.8).

4.2.4. Preliminary Geologic Model of the US/BK Site

The major features in our preliminary model (Figure 4.7) based on surface and subsurface geologic information and on borehole data are (from north to south):

(1)   a discontinuous series of three northeast-striking S-zone segments,

(2)   a lamprophyre-bearing K-zone north of the BK room,

(3)   some northwest-striking lamprophyres,

(4)   a west-striking K-zone south of the BK room.

We correlate Features 1, 2, and 3 with major structures that are mapped at the surface and shown near the northern border of Figure 4.3. We have not identified a K-zone at the surface that would correspond to Feature 4 in our model. Our model is different from that in Figure 4.6 which shows an S-zone extending continuously across the US/BK site. In our model, the S-zone consists of discontinuous segments (1a, 1b, and 1c) that are separated by lamprophyres. The two models
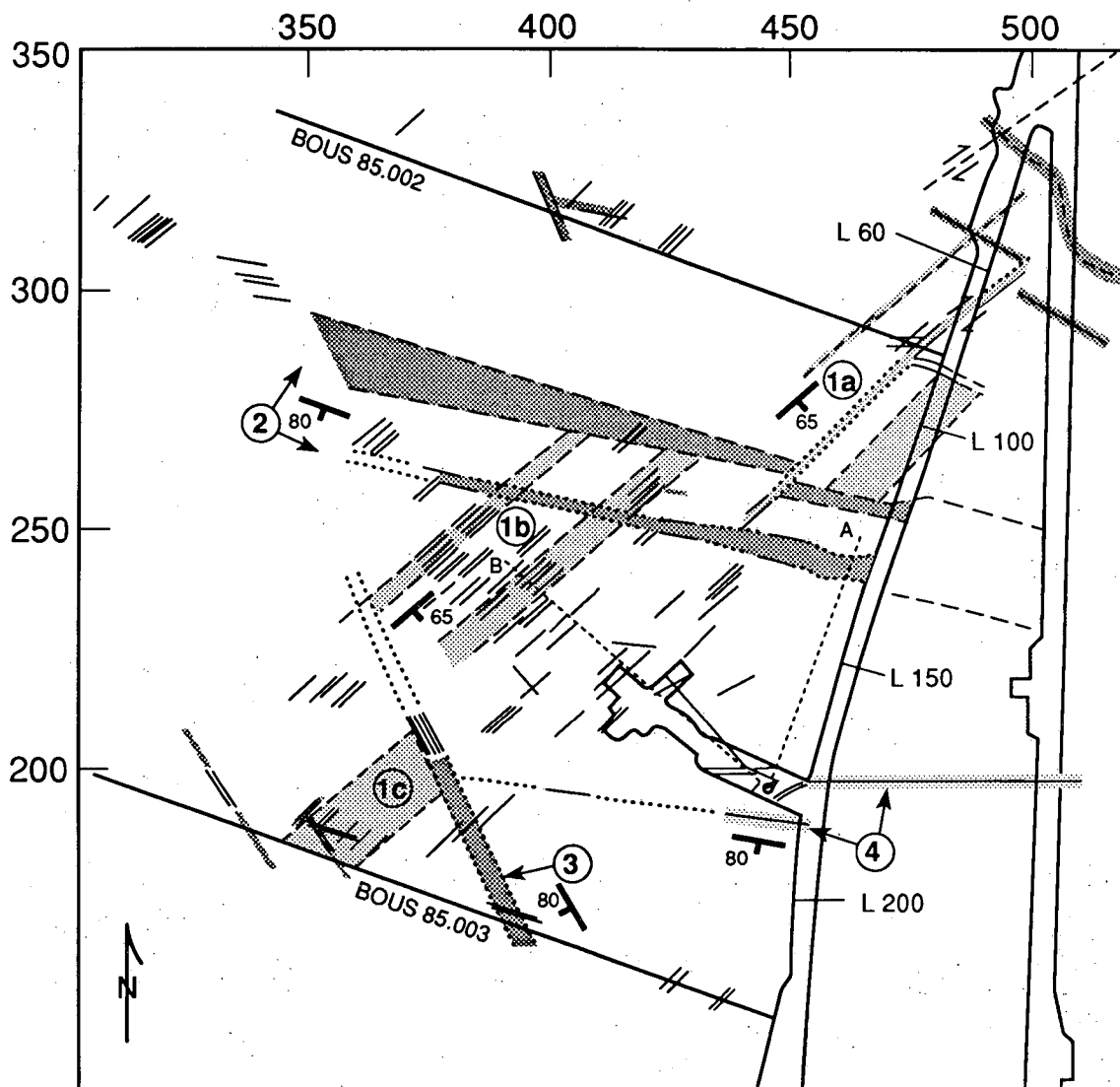
XBL 8911-7898

Figure 4.7. Map projection at the 1730 m level of borehole fractures (fine lines) and associated major structures at the US/BK site. Closely spaced pairs of lines mark edges of fractured zones; single lines mark prominent single fractures. Strike and dip used for projection of fractures shown in heavy line; these attitudes correspond to the attitudes of the major features. Feature 1 (medium screen): S-zone fractures. Feature 2 (dark screen): K-lamprophyres. Feature 3 (dark screen): Northwest-striking lamprophyres. Feature 4 (light screen): K-zone. Tick marks are on a 50 m grid. North is to top of figure. Dashed lines A and B mark lines of cross section shown on Figure 4.8.
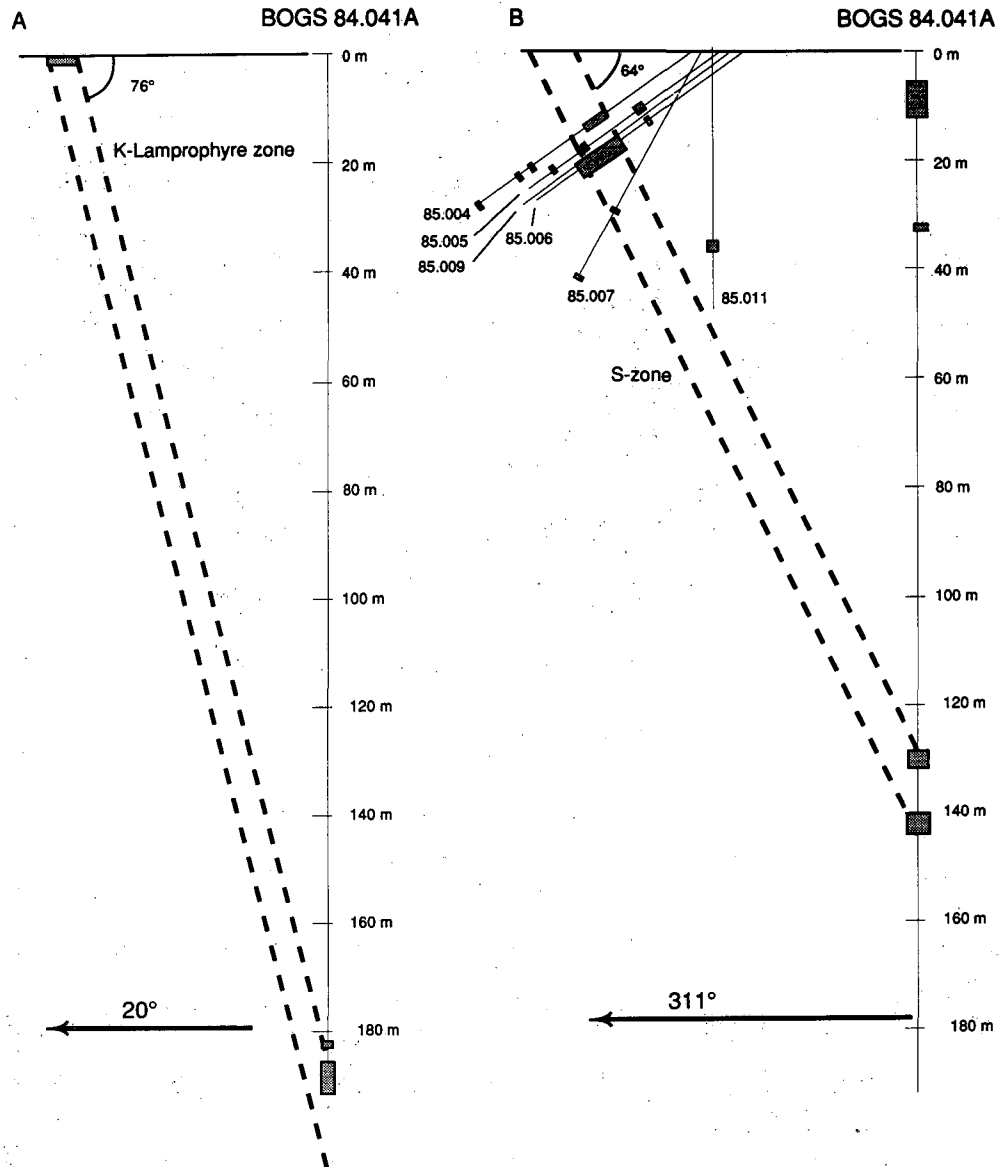
Figure 4.8. Vertical cross sections through borehole BOBK 84.041A. The bottom of the hole is at a depth of 191.5 m. Horizontal and vertical scales are equal. (a) Cross section along plane that strikes 20°, perpendicular to strike of K-lamprophyres. Dark shading indicates lamprophyres. Dashed line marks inferred edges of K-lamprophyres. (b) Cross section along plane that strikes 311°, perpendicular to strike of S-zone. Dark shading marks intervals with numerous fractures; fractured intervals in non-vertical holes are projected orthogonally onto the cross section plane. Dashed line marks inferred edges of S-zone.

should have different hydrologic behaviors.

Three lines of evidence suggest that a single, continuous S-zone segment does not extend on strike past the BK room as is shown on Figure 4.6. First, within a few meters northwest of the BK room we see only a limited amount of fracturing in the boreholes (Figures 4.7 and 4.8), and no trace of a prominent band of fault gouge that is exposed near L76 in the S-zone in the laboratory tunnel. Second, the wide zone of S-fractures between L80 and L103 does not appear to extend into the BK room. The third point regards the apparent continuity of the west-striking lamprophyres. We show two thick K-lamprophyres (Feature 2) north of the BK room in Figure 4.7. The nearly coplanar alignment of the southern lamprophyre in three boreholes and in the laboratory tunnel strongly suggests that this lamprophyre is not significantly displaced by an S-zone. Because the Feature 1a S-zone (Figure 4.7) appears to laterally offset features in and near the laboratory tunnel by several meters, the apparent lack of lateral displacement of the southern-most K-lamprophyre indicates that Feature 1a stops at the K-lamprophyres or north of them.

The geologic data are more consistent with a series of discontinuous S-zone segments. The extensive fracturing 25-50 m northwest of the BK room in the boreholes suggests that a second S-zone segment occurs there (Feature 1b, Figure 4.7). Segments 1a and 1b would form a right-stepping echelon pair. The south end of Feature 1a and the north end of Feature 1b would terminate at the K-lamprophyres. This interpretation is consistent with the geologic map of the surface (Figure 4.3) and with our own surface observations. Fractures in the core from borehole BOUS 85.003 suggests that an S-zone segment (Feature 1c, Figure 4.7) intersects the hole at a depth between 90 and 105 m. If this S-zone segment strikes N50° as we interpret, then Features 1b and 1c would be discontinuous. Northwest-striking lamprophyres (Feature 3) would separate Features 1b and 1c. The S-zone segments may have formed part of a once-continuous structure that was offset by slip across the lamprophyres, but the segments may also have formed part of a structure that was originally discontinuous.

The west-striking K-zone near the BK room (Feature 4, Figure 4.7) is well exposed in the laboratory tunnel and was well exposed in the floor of the BK room before being covered by concrete. The evidence for this feature extending several tens of meters west from the laboratory tunnel comes from a single borehole (BOBK 86.002, Figure 4.2) and is not particularly strong.

The interval of lamprophyre encountered from 88.3 to 117.3 m in borehole BOBK 86.001 is anomalously thick. It may be that some of this thickness is due to a northwest-striking lamprophyre that projects into the region from the southeast.

4.2.5. Geophysical Tomography

We used seismic tomograms (Gelbke, 1988) and radar tomograms (Niva and Olsson, 1987, 1988a, 1988b) to check and extend the geologic model of the US/BK site. Both kinds of tomograms were produced using signals transmitted between the laboratory tunnel, borehole BOUS 85.002, and borehole BOUS 85.003. The tomograms are thus "three-sided."

We have defined several major low velocity anomalies on the seismic velocity tomogram using the 5050 m/sec contour (Figures 4.9 and 4.10). In Figure 4.10, the major features inferred from the geologic data are superposed on these anomalies. The geologic features are indicated by circled numbers and the seismic anomalies by uncircled numbers. We interpret the eastern "stem" of anomaly S2 to represent fractured K-lamprophyres of Feature 2. The K-lamprophyres are associated with a major structure that cuts through the Juchlistock area (Feature 2 of Figure 4.3), and we expect that this structure would extend through the US/BK site. The exposures of the K-lamprophyres in the laboratory tunnel are highly fractured and highly deformed, and we expect them to generally have low in-situ velocities.

We interpret anomaly S1a to reflect S-zone fractures that are bounded by a K-lamprophyre and to match up with Feature 1a. Anomaly S1a does not appear to project on strike to the southwest past anomaly S2. Anomaly S1b and the southwest arm of anomaly S2 (Figure 4.10)
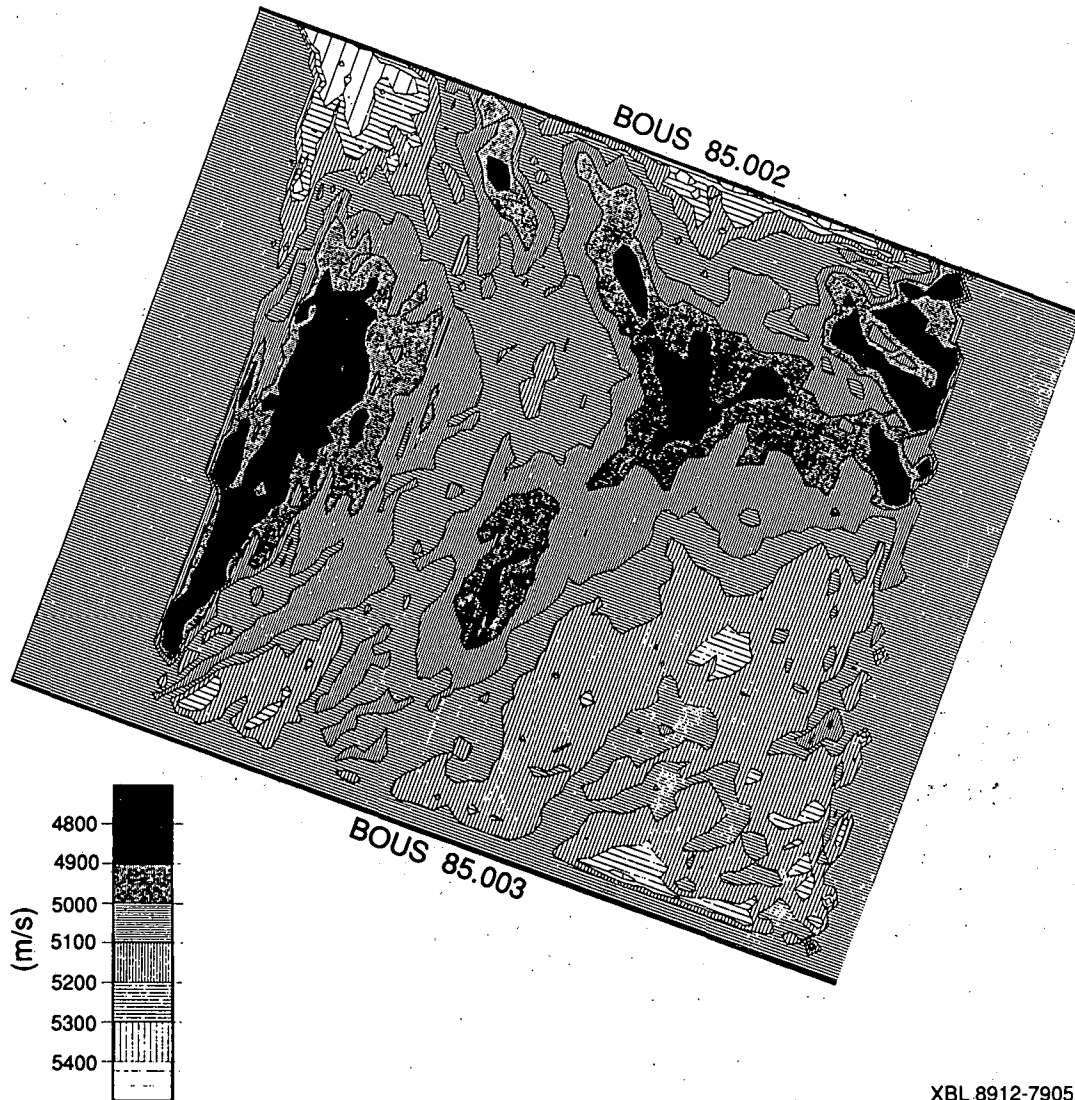
XBL 8912-7905

Figure 4.9. Seismic tomogram of the velocity structure between BOUS 85.002 and BOUS
85.003. Modified from Gelbke (1988) Figure 65. Boreholes BOUS 85.002 and
85.003 are contained within the heavy lines at the edges of the tomogram,
but do not extend along the entire length of the lines.
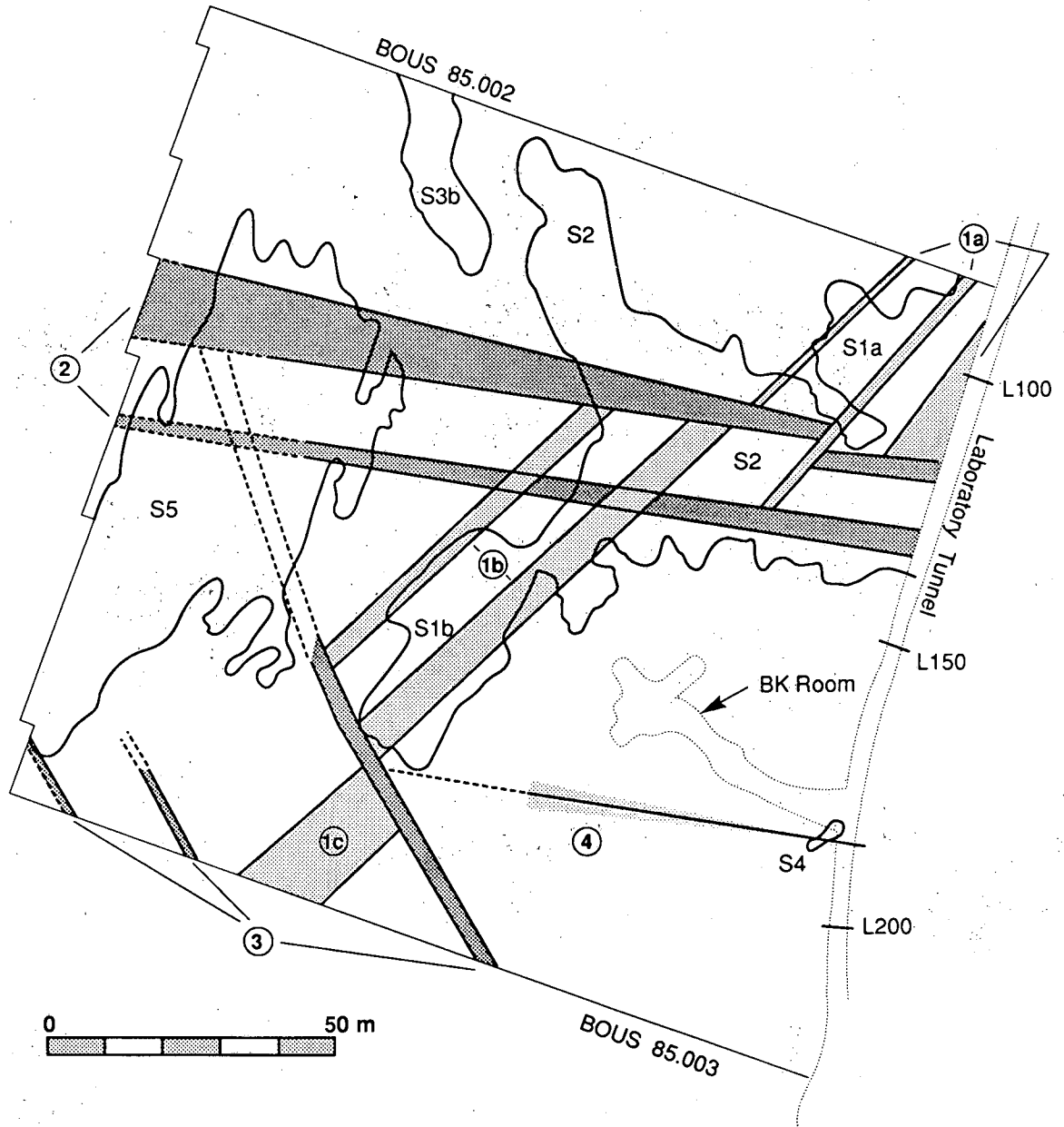
Figure 4.10. Projection in the plane of tomography showing the features of the preliminary
structural model of the US/BK site superposed on the 5050 m/sec contour
from Figure 4.9. The geologic features are marked by circled numbers. The
seismic anomalies are marked by uncircled numbers. Seismic anomalies S1-S5
are described in the text.

correspond to a cluster of concentrated S-zone fractures (Feature 1b) in Figure 4.7. The southwest end of anomaly S1b occurs along the trend of the lamprophyres of Feature 3b (Figure 4.10). This suggests that Feature 1b terminates at the lamprophyres. Because anomaly S1b does not project on strike to the northeast past the stem of anomaly S2, we interpret the seismic tomogram as supporting our model of echelon S-zone segments 1b and 1c being separated by lamprophyres. Feature 1c does not have a prominent corresponding anomaly on the seismic tomogram. It is interesting that the east-west trending portion of seismic anomaly S2 occurs only where Feature 2 is intersected by Features 1a and 1b. An alternative explanation for the eastern stem of seismic anomaly S2 is that it reflects enhanced fracturing at these intersections rather than just the presence of Feature 2. This could explain why anomaly S2 would not extend across the entire seismic tomogram even though Feature 2 almost surely extends across the entire US/BK site.

The borehole logs of BOUS 85.002 (Keusen, et al. 1989) contain ample evidence for fracturing from 69 to 113 m down the borehole, the interval into which the northwest arm of anomaly S2 and anomaly S3b project. We interpret the northwest arm of anomaly S2 and anomaly S3b as corresponding to lamprophyres that strike northwest rather than fracture zones. This interpretation is supported by the geologic map of the surface (Figure 4.3), which shows a northwest-striking lamprophyre intersecting the K-zone containing the K-lamprophyres at an elevation of ~2160 m; this intersection projects down-dip to near the intersection of S3b and BOUS 85.002 in the plane of the tomogram.

Anomaly S4 (Figure 4.10) occurs where numerous fractures have been mapped on the floor of the room and where we have inferred a step in the K-zone of Feature 4. Feature 4 is not represented on the seismic tomogram as a prominent geophysical anomaly west of S4, but we do not expect K-zones to necessarily have prominent tomographic signatures except at steps or at their ends. It is also possible that Feature 4 does not extend to the west of the BK room. In that case, anomaly S4 might represent fractures at the west end of Feature 4.

Anomaly S5 (Figure 4.10) most likely reflects artifacts produced by the inversion process in an area where the density of seismic rays is low; no acoustic rays were transmitted from or received along a line connecting the ends of the two boreholes bounding the US/BK site. The rock at S5 may or may not have a low acoustic velocity.

The anomalies on the seismic tomogram are consistent with our structural interpretation based on geology and borehole data. The only significant change the seismic tomogram would suggest is that northwest-striking lamprophyres should be added to account for anomaly S3b and the northwest arm of anomaly S2.

We now compare our preliminary model to some radar tomograms. The amplitudes and travel times of radar signals were inverted to yield attenuation (Figure 4.11) and slowness tomograms (Figure 4.12), respectively. Slowness is the reciprocal of velocity; high radar slowness equates to low radar velocity. The attenuation and the velocity (or slowness) of a radar signal is particularly sensitive to the water content of the rock. Therefore, radar tomograms primarily reflect the water distribution in a rock mass and should be suited for inferring the distribution of saturated fractures and pores.

Tomographic radar measurements were made at the US/BK site in late 1986 (Phase 1), the spring of 1987 (Phase 2), and late in 1987 (Phase 3). Brine injected during Phases 2 and 3 served as a tracer and is discussed in Section 4.3. The brine tracer is relatively weak and is not especially prominent on the tomograms except near the injection point. Tomograms from the different phases look slightly different in large part, because the data acquisition system and the processing techniques were improved through the course of the tomography experiments. We have relied primarily on the most recent (Phase 3) tomograms to help model the geologic structure at the US/BK site.

Two major anomalies exist on the Phase 3 radar tomograms (Figures 4.11 and 4.12). The first is a broad belt that trends approximately east-west midway between the BK room and BOUS
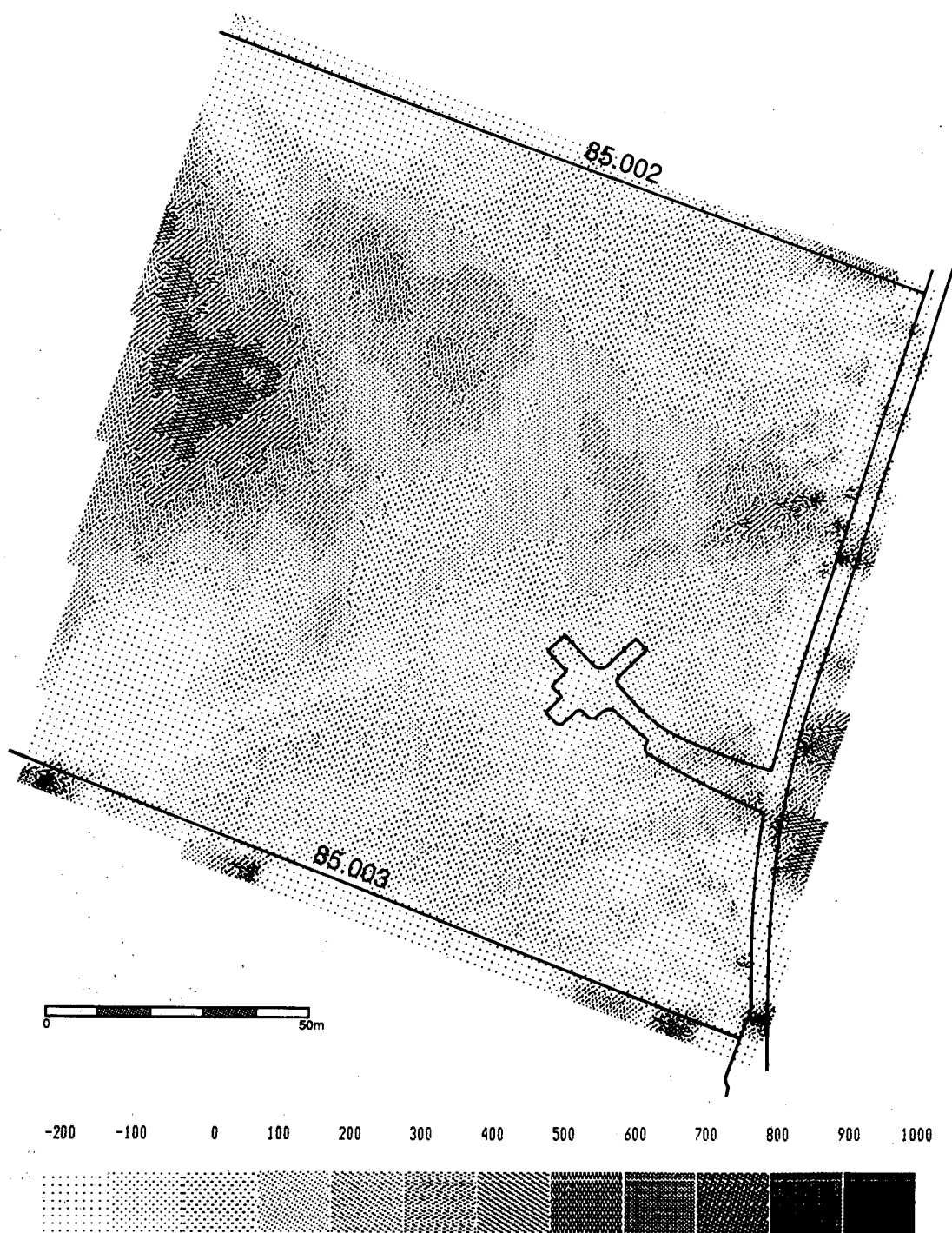
Figure 4.11. Phase 3 tomogram of radar attenuation structure between BOUS 85.002 and BOUS 85.003
(from Niva and Olsson, 1988b, Figure 4.6). Units are in dB/m. North is to top of page.
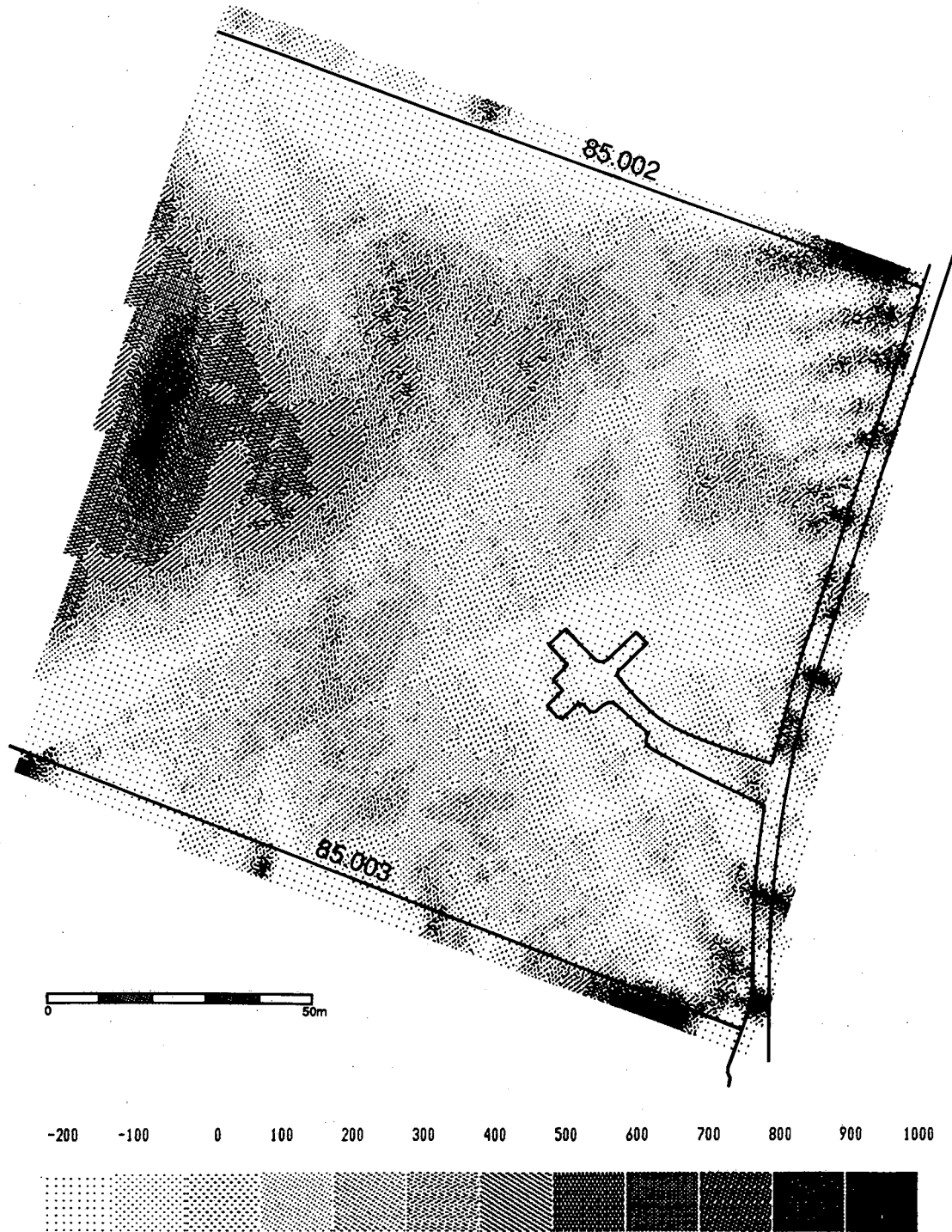
Figure 4.12. Phase 3 tomogram of radar slowness structure between BOUS 85.002 and BOUS 85.003. Values relative to 8050 m/sec standard (from Niva and Olsson, 1988b, Figure 4.2). Units are in dB/m. North is to top of page.

85.002. It is essentially in the same position as anomaly S2 on the seismic tomogram (Figures 4.10). We interpret this belt as representing the K-lamprophyres (Feature 2, Figure 4.10). Note that the internal structure of this belt is complicated and has different appearances in the radar and seismic tomograms. The tomograms thus do not clearly define the internal structure of Feature 2; they do indicate its internal structure is complicated. The second major anomaly occupies a triangular region at the west end of the tomograms. Like seismic anomaly S5 (Figure 4.10), this radar anomaly is considered to be an artifact of the inversion process.

A series of disconnected radar anomalies correspond to most of the intersections of the major features in our model. One anomaly occurs at the intersection of Features 1a and 2. Another anomaly occurs where Features 1b, 1c, 3a, and 4 converge. An anomaly of large magnitude (albeit small size) is located where Feature 1c intersects borehole BOUS 85.003. A radar anomaly also exists where seismic anomaly S3b (presumably representing a lamprophyre) intersects Feature 2. Even though the radar tomograms do not show continuous, well-defined anomalies that correspond to the features in our model, the anomalies at the intersections would be consistent with our model if the intersections are sites of pronounced fracturing.

4.2.6. Revised Structural Model of the US/BK Site and Hydrologic Implications

The radar and seismic tomograms support the presence and location of the main features in the preliminary model of Figure 4.7. This increases our confidence in the utility of tomography in projecting the major geologic features into the target site. Based on the geophysical tomograms, the structural model of the US/BK site was modified to include two northwest-striking lamprophyres (Features 3b) in the north-central part of the site (Figure 4.13). We now discuss the hydrologic implications of the model. The results of the subsurface geologic, borehole, and tomographic investigations all indicate that the lamprophyre-bearing K-zone (Feature 2, Figure 4.13) is an especially prominent structure. Fracturing and fluid flow along this feature may be quite complex. Because of locally strong fracturing along the K-lamprophyres, they may locally
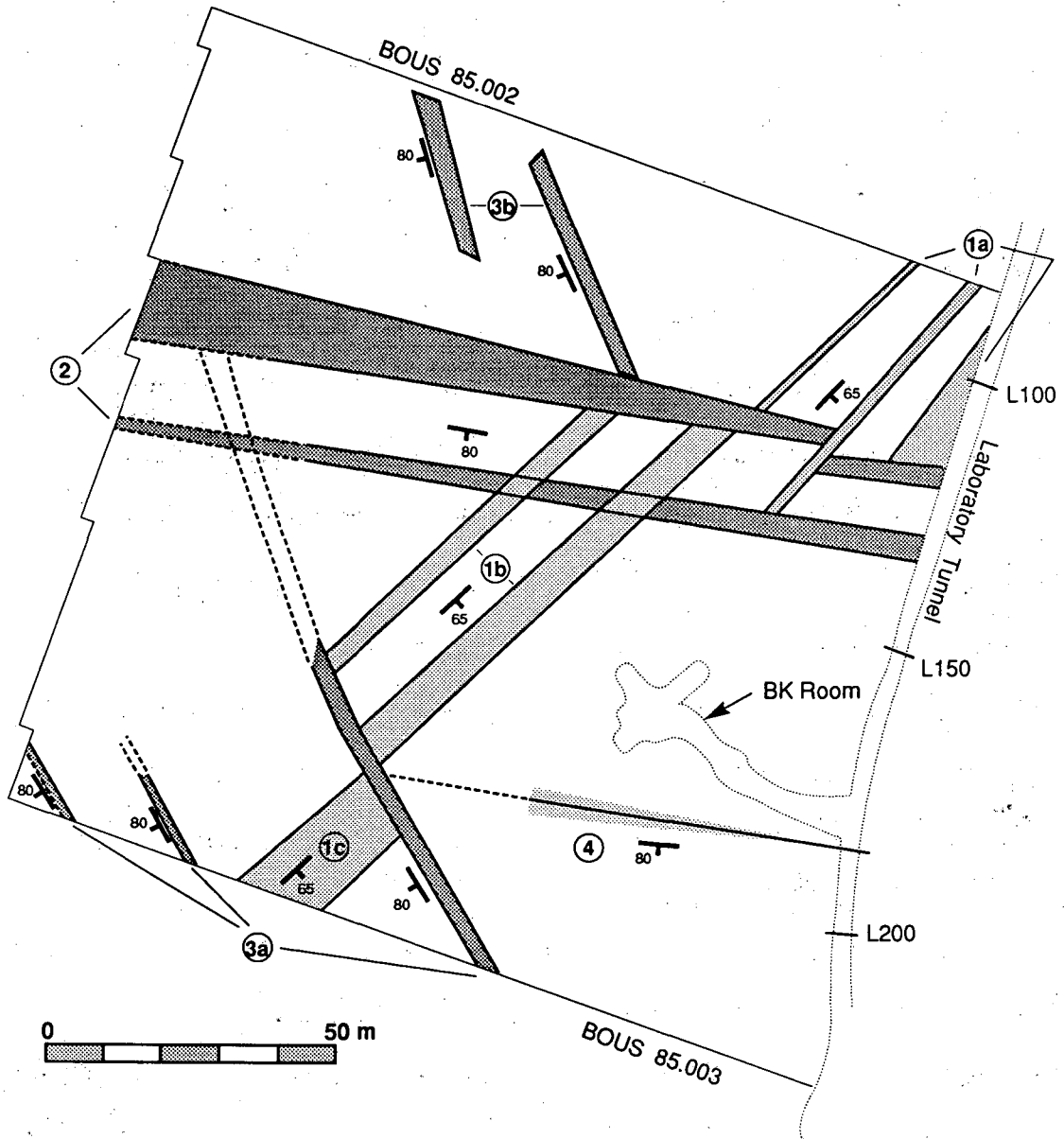
Figure 4.13. Projection in the plane of tomography showing revised model of major geologic structures at the US/BK site. Strike and dip of the major features shown in heavy line. This model includes two lamprophyres near the north (upper) edge of the projection that are not in Figure 4.10.

transmit water readily in east-west and vertical directions. Based on the local borehole data, we expect that the K-lamprophyres form a continuous belt and would tend to hydrologically separate the two S-zone segments 1a and 1b. The numerous fractures in the S-zone segments probably form a well connected network. The hydraulic conductivity along these segments probably is high, both along strike and in the vertical direction. The northwest-striking lamprophyres (Features 3a and 3b) probably contain vertical and northwest-trending flow paths. These lamprophyres probably are much thinner and more discontinuous than the K-lamprophyres, and may transmit water across strike more readily, especially where intersected by S-zones. The southernmost of these lamprophyres (3a) are interpreted to separate S-zone segments 1b and 1c. The small K-zone (Feature 4) may offer a conduit from the southwest end of Feature 1b towards the laboratory tunnel.

Although the positions of the major structural elements at the US/BK site seem to be fairly well resolved, the nature of the intersections between structures is not well established. For example, although the S-zone appears to consist of discontinuous segments that are separated by lamprophyres, we cannot rule out the possibility that hydraulic connections extend across the lamprophyres where intersected by S-zones. The geophysical tomograms suggest that fracturing may be particularly extensive at such intersections. Hydrologic testing is necessary to firmly establish the nature of the hydraulic connections between the lamprophyres and S-zones.

4.3. Brine Tracer Tests and Difference Tomography

Brine tracers were injected (Figure 4.14) during the second and third phase of the radar tomography surveys. We have used difference tomograms to check how well our model identified major flow paths and flow barriers at the US/BK site, and to indicate how the model might be improved. Difference tomograms (Figure 4.15 and 4.16) are prepared by inverting travel time- or amplitude-differences between two tomographic surveys. These tomograms show how the region being analyzed in the plane of the tomography changed between test phases, allowing
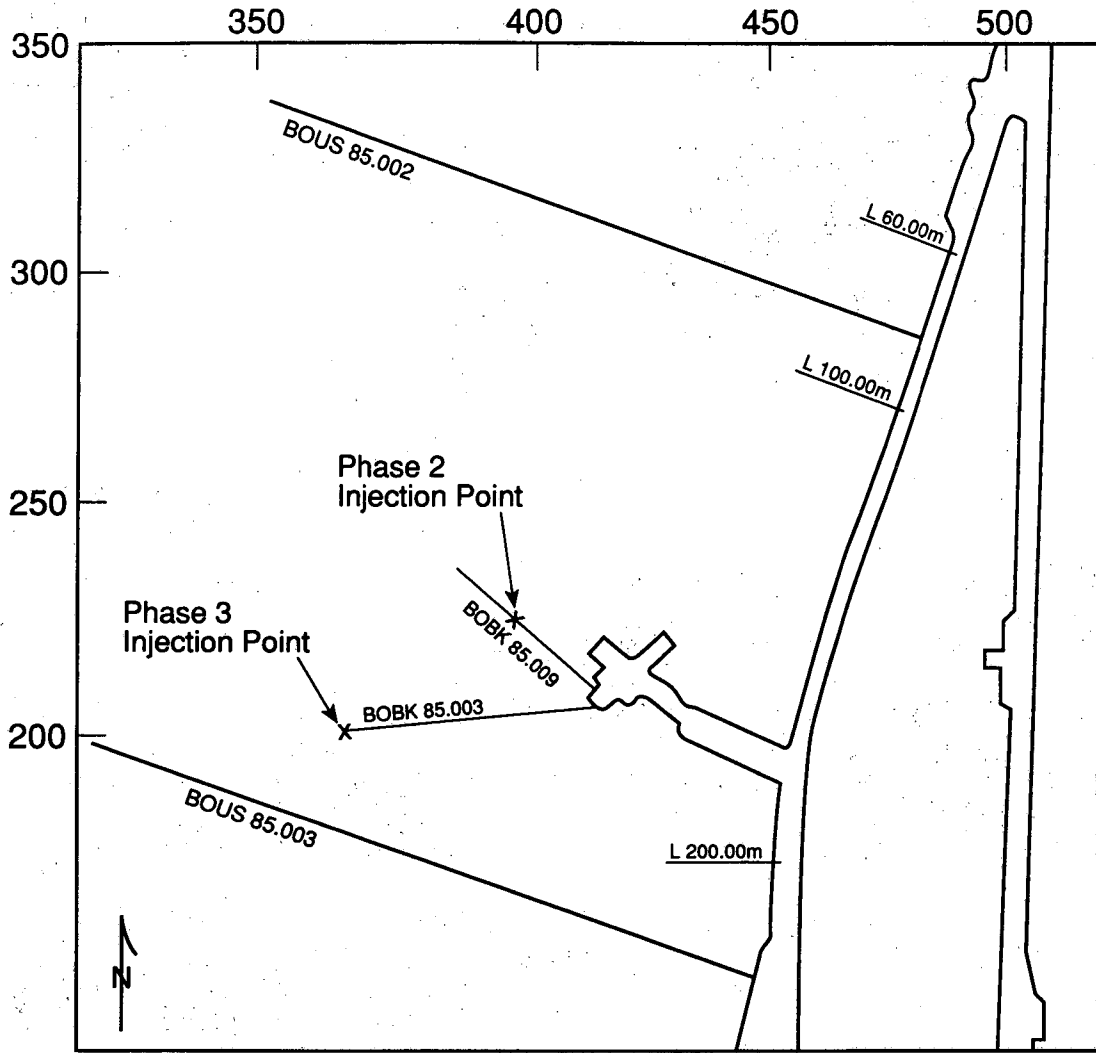
Figure 4.14. Projection in the plane of tomography showing where brine was injected during the phase 2 and phase 3 tomographic measurements. Tick marks are on a 50 m grid.

XBL 8911-7899
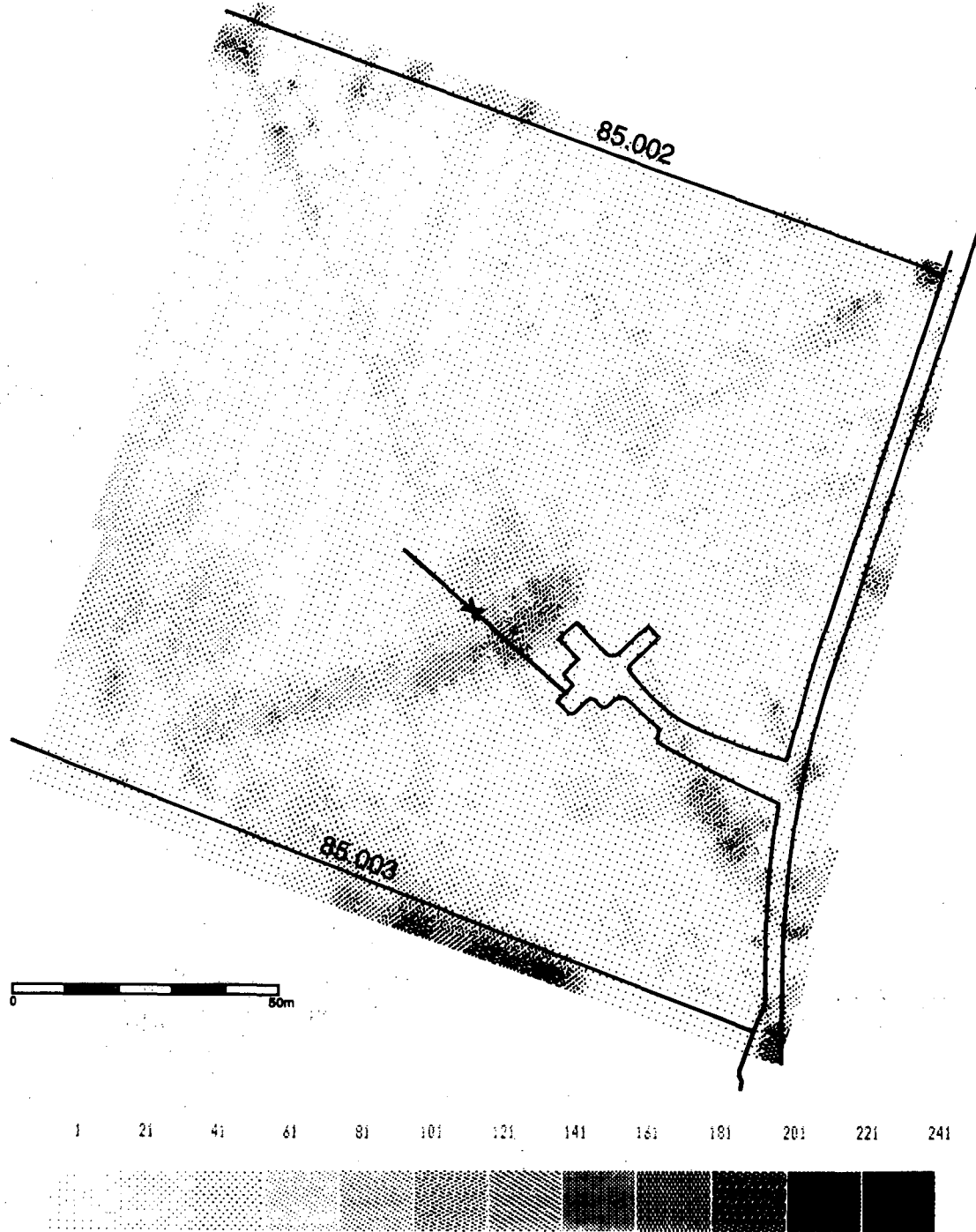
XBL 8912-7902

Figure 4.15. Difference tomogram of radar attenuation structure between BOUS 85.002 and
BOUS 85.003 from phase 1 and phase 2 measurements. The tomogram shows
the increase in radar attenuation and indicates where brine has migrated during
phase 2 (from Niva and Olsson, 1988a, Figure 5.12). Units are in dB/m. North
is to top of page.
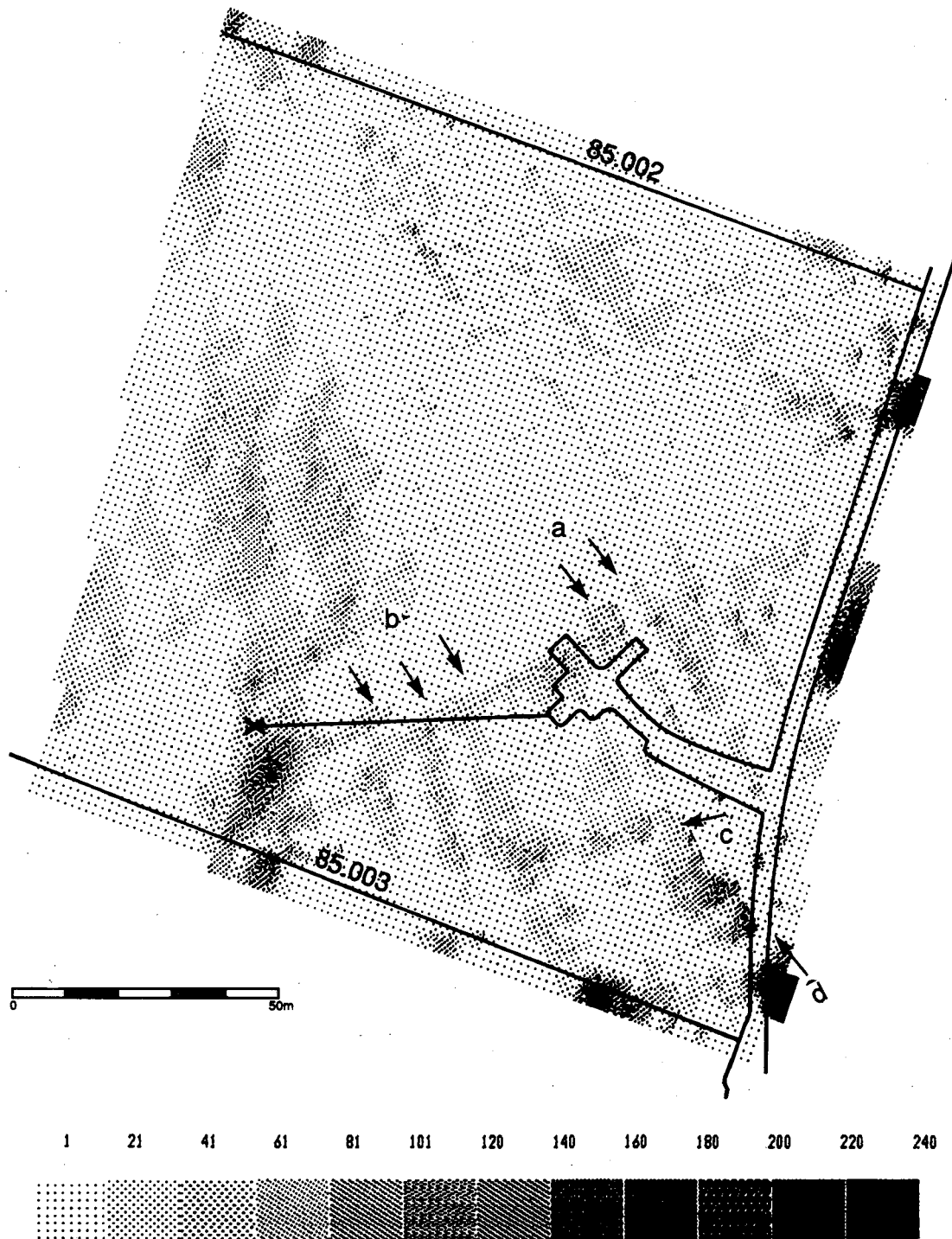
XBL 8912-7903

Figure 4.16. Difference tomogram of radar attenuation structure between BOUS 85.002 and
BOUS 85.003 from phase 2 and phase 3 measurements. The tomogram shows
the increase in radar attenuation and indicates where brine has migrated during
phase 3 (from Niva and Olsson, 1988b, Figure 5.26). Units are in dB/m. North
is to top of page.

the brine paths to be traced. The brine will locally increase the radar attenuation but should cause little change in the radar velocity at the frequency and brine concentration used (Sen et al., 1981). Based on these effects, the attenuation difference tomograms should be more sensitive to the brine than the slowness difference tomograms. Furthermore, the processing and instrumentation changes mentioned in Section 4.2.5 did not affect the attenuation difference tomograms, but the instrumentation changes most likely did produce some changes in the slowness difference tomograms. Not surprisingly, the radar attenuation difference tomograms provided a more consistent picture of the brine location than the slowness tomograms; from here on we discuss only the attenuation difference tomograms. Figure 4.15 was prepared using attenuation data from phases 1 and 2; it reveals the flow of brine injected during phase 2. Figure 4.16 was prepared using attenuation data from phases 2 and 3; it reveals the flow of brine injected during phase 3.

4.3.1. Expected Results of Brine Tracer Tests

The injection points for the tracer tests are nearly in the plane of the tomography and are below and west of the main laboratory tunnel (Figure 4.14). The laboratory tunnel, the BK room, and boreholes BOUS 85.002 and 85.003 were at atmospheric pressure during the injections, and we expect the hydrologic gradient to have been toward these openings. We also expected brine from each test to migrate along major features identified in our structural model towards the laboratory tunnels and/or these boreholes.

According to our structural model (Figure 4.13), the Phase 2 injection point is located midway along the length of S-zone segment 1b. This segment is bounded by lamprophyres about 20 m on either side of the injection point. The 1b fractures should form a well connected network. We expect that the brine detected in the plane of the tomography could extend northeast and southwest of the injection point along Feature 1b towards both sets of lamprophyres. Brine that flowed northeast might eventually encounter the K-lamprophyres (Feature 2). These probably would hydrologically separate S-zone segments 1a and 1b. Although brine would not be expected

to flow across the K-lamprophyres some might flow along them towards the main laboratory tunnel. Brine that flowed southwest along Feature 1b might do one of three things once it reached the series of thin lamprophyres (Feature 3a):

(1)   flow south across the lamprophyres toward borehole BOUS 85.003 that do not form part of the well defined throughgoing fracture zones;

(2)   flow southeast along the lamprophyres towards borehole BOUS 85.003;

(3)   flow east along the K-zone south of the BK room (Feature 4).

Because we expect the hydraulic conductivity along the S-zone to be the greatest in the vertical direction, the brine might eventually flow out of the gently inclined plane of the tomography.

The Phase 3 injection point is located about 25 m north of borehole BOUS 85.003, just south of where the S-zone segment 1b intersects the Feature 3a lamprophyres (Figure 4.13). We interpret the injection point as not being in a major geologic or hydrologic feature. We expect that the hydrologic gradient would favor flow toward borehole BOUS 85.003 along one or more of the following paths:

(1)   south by way of "background matrix" fractures that do not form part of the well defined throughgoing fracture zones;

(2)   southeast along the lamprophyres;

(3)   southeast to Feature 1c and then southwest along it to the borehole.

The last option seems most likely because the hydraulic conductivity along S-zone segment 1c would be highest.

4.3.2. Discussion

The results from the phase 1-2 and phase 2-3 radar attenuation difference tomograms are, on the whole, consistent with the predictions of our structural model. Most of the brine displayed in the phase 2 radar attenuation difference tomogram (Figure 4.15) appears to be contained within

this S-zone segment 1b. The position and shape of the brine anomaly in the phase 3 radar attenuation difference tomogram (Figure 4.16) indicates the phase 2-3 brine flow was concentrated along a path that extends about 10 m southeast from the injection point and then heads southwest towards borehole BOUS 85.003. This is consistent with flow being strongly controlled by both the hydrologic gradient and Feature 1c. Both radar attenuation difference tomograms are consistent with our interpretation that Feature 1b does not continue on strike to the south across the Feature 3a lamprophyres.

The radar difference tomograms increase our confidence in our interpretation of the geologic structure at the US/BK site. The features which we expected flow along were highlighted, and the features we did not expect flow across seem to have impeded flow. The difference tomograms suggest that not all the hydrologic features at the site are contained in our structural model. If all of the anomalies on the attenuation difference (e.g. Features a,b,c and d on Figure 4.16) tomograms accurately represent the location of significant amounts of brine, then a detectable portion of flow at the US/BK site is occurring along a network of fractures that do not form a major throughgoing zone. The distribution of fractures in such a network would not have been identified in our model, which was constructed to identify only the major features, but perhaps should be included in a hydrologic model as "background matrix" fractures.

4.4. Conclusions

The thrust of our effort is to integrate geologic observations and geophysical measurements to identify, locate, and characterize the major geologic structures at a given site. We place a heavy emphasis on characterizing the fracture zone structural systematics help unite the site-specific geologic mapping, borehole data, and geophysical information. We strongly recommend that detailed mapping be carried out where possible.

For our methodology to work best we need 1) site-specific geologic, borehole, and geophysical data and 2) exposures that allow the systematics of the major fracture zones near the site to be defined. Clearly, these key requirements for our methodology to work were met at Grimsel. In many places, excellent exposures will not be readily available and it may be extremely difficult (or too expensive) to determine the systematics of the fracture systems. For example, the subsurface fracture systems in many places are not exposed at the surface at all. In such cases, studies of geologically analogous areas may be useful, even if those areas are distant from the target site. Although the features at a given site will be unique to some extent, similar features would probably occur elsewhere. Still, in some locations the fracture systems may be too complex to evaluate their systematics. In cases where the systematics can not be determined, it may be appropriate to consider a number of significantly different geologic models and to treat the fracture systems stochastically. Some direct sampling of the target site is essential to relate geologic models and tomograms, and small-diameter boreholes are probably the least destructive way to conduct direct sampling.

Geophysical tomograms provide a unique way to check geologic models. In places where clusters of boreholes would not be drilled, geophysical tomograms would be relied upon even more heavily than we did here. The usefulness of tomograms is a function of both their resolution and how well the geology is known. Anomalies on tomograms can reflect a wide range of features (different rock types, fractures, zones of hydrothermal alteration, areas of increased porosity, etc.), but major throughgoing geologic structures may not be represented as continuous anomalies on tomograms. An advance knowledge of the geology is essential in order for the anomalies to be interpreted correctly.

In conclusion, geologic and geophysical information can be integrated to give a consistent model of the major geologic structures in rock volumes with dimensions on the order of one hundred meters. Geologic observations establish the position, orientation, and type of structures near

a site. Geophysical measurements and borehole data aid in projecting the structures within a site. Detailed geologic observations of the internal structure of the major features can provide insight into how fluid might flow along the structure, and radar difference tomography can image how tracers actually do flow. The tomograms suggest that the intersections of major geologic structures could be sites of particularly extensive fracturing and enhanced fluid flow. An integrated geologic/geophysical investigation can contribute greatly to hydrologic site characterization.

5.0. HYDROLOGIC FIELD TESTING IN FRACTURED ROCK

Hydraulic field testing from boreholes has two places in the characterization scheme described here. Well tests can be used to help define a hydrologic conceptual model for fracture hydrology. As shown in Section 6, the hydrologic information would contribute to the geologic and geophysical model as described in Section 4. Well testing comes up again after the conceptual model has been defined when we wish to use inverse techniques to construct a predictive model based on the conceptual model. In both cases, interpretation of a well test is a type of inverse method: we use observations on the behavior of the system to predict or calculate the system parameters. In the case of conceptual model development, the inversion is based on the supposition of simple, well defined system geometry and the inversion process yields the flow parameters (permeability, specific storage, etc.) associated with parts of the system. In Section 7, we show how inversion can be used to help determine aspects of the geometry as well as the flow parameters after the conceptual model has been proposed. The fundamentals of well testing are the same in either case. An example of well testing for conceptual model development is given here, but the example of using well testing data for inversion to obtain a predictive model is deferred until Section 7 where the inversion technique is described.

5.1. Theory of Hydrologic Tests in Fractured Rock

There are two types of hydrologic field tests that can be done from boreholes: hydraulic tests and tracer tests. The theory supporting interpretation of these tests is well established for homogeneous media under well defined boundary conditions. Under heterogeneous conditions, such as those in fractured rock, the interpretation of standard tests becomes more difficult. In general, hydrologic testing under these conditions will be more effective if it is conducted in a cross-hole or interference manner. Single hole tests will not provide the required information about the disposition and interrelationship among the highly conductive features.

In a hydraulic test, fluid is either pumped into or withdrawn from a well. The response to this perturbation is the change in hydraulic head which can be measured both at the pumping well and at the monitoring wells. These tests can be done in four basically different modes: steady state, constant flux, constant head, and slug tests where neither the head nor the flux in the well is kept constant. Tracer tests can also be configured in several modes. In a single well configuration, they include point dilution and injection-withdrawal tests. In a multiple well configuration, there are converging tests and two-well circulation tests. These tests are briefly described below.

5.1.1. Types of Hydrologic Tests

In a steady-state test, either the flow rate or the head at the well is kept constant until there is no further observable change in the system. For many sets of boundary conditions, there will be no true steady state. In these cases, we make the assumption of insignificant local changes in order to make an analysis of the data. In any case, the data from a steady state test will simply reflect the "bottle neck" or least conductive part of the flow path between the perturbation point and the boundary. The test is not particularly sensitive to the arrangement of the conducting elements in space.

In a constant pressure test, the hydraulic head in an isolated interval is kept constant and the transient flow rate is monitored. In most groundwater applications, however, constant flux tests are more commonly used because it is generally easier to achieve and maintain a constant flux, q, than a constant pressure from the onset of the test. Therefore, analytical solutions are more readily available for constant flux tests. The majority of the published papers in the literature are based on constant flow rate tests.

Constant flow tests are also easier to analyze because the type curves have somewhat more distinct shapes compared to constant pressure tests where q vs. time curves are more or less flat. Only pressure can be measured at observation wells. So, in analyzing constant pressure crosshole tests, pressure vs. time type curves have to be developed for each well at different radial distances, because the constant pressure solution does not have similarity in Kt/S_sr^2, where K is the

hydraulic conductivity, t is time, S_s is the specific storage and r is the radial distance measured from the well. The constant rate boundary condition is, in general, mathematically easier to work with to develop a new analytical model. Reciprocity holds for constant flow tests over all time. That is, if you pump q l/min from well A, the drawdown at well B will be the same as the draw-down at A when B is pumped at the rate of q l/min. The same is not true for constant head tests.

However, constant pressure tests are not without advantages. In very low permeability rocks, constant pressure is generally easier to achieve than a constant rate. It is also easier to minimize the wellbore storage effect in a constant pressure case. Moreover, because the rock near the wellbore is subjected to a constant pressure throughout the test, there is less concern about the permeability near the well changing as a function of time. However, the permeability may change farther away from the well as the pressure front propagates into the rock.

Whichever method is used, when conducting well tests in a tight fractured rock, it is important to measure early time data as accurately as possible. Transient data reflects the change of hydraulic conductivity in space as a function of time. In this regard, transient data is more descriptive of the rock heterogeneity than steady state data, which is influenced by the spatial arrangement of heterogeneity in an unknown way. Especially when there is a skin zone near the well, one should be able to resolve the nature of the skin by using a set of good transient data (i.e., data from both the flow period and the shut-in period).

In a point dilution test, a known concentration of tracer is introduced in a packed-off interval and the subsequent change in concentration due to the natural groundwater flow is monitored. The groundwater velocity near the borehole can be estimated by analyzing this concentration change.

In an injection-withdrawal test, a tracer is actively injected in the interval. This is then followed by a pumping and the concentration of the pumped fluid is monitored. This test is expected to yield an estimate of the dispersion coefficient.

A two-well circulation test is done by pumping fluid from one well and injecting it into another. After a steady state flow field is established a plume of tracer is introduced in the

injection well and the break-through is monitored in the pumping well. This test is used to estimate the ratio between flow and velocity as well as the dispersion coefficient.

In a converging test, one well is pumped to establish a steady-state flow field. A plume of tracer is introduced in another well and the break-through is monitored in the pumping well. This test should also give one an estimate of the ratio between flow and velocity as well as the dispersion coefficient.

5.1.2. Interpretation of Hydrologic Tests

Fundamentally, well tests provide information about how much flow or pressure will result from a given perturbation in the hydraulic potential field or vice versa. Any further interpretation requires that the analyst provides a conceptual model which essentially describes how the conductances in the system are arranged. However, there may be a number of possible conceptual models with different combinations of geometry and flow parameters that cause the same observed response at a given point. Alternatively, none of the well defined conceptual models may match the data at all. For this reason, there is always an inherent question about the uniqueness of any solution to a well test problem. The degree of uncertainty can be reduced by having many observation points, although it is not usually practical to do so.

Hydraulic tests are diffusion dominated. This means that we may know the location of the perturbation and the location of the response, but we do not know the structure of the flow paths (unlike seismic wave propagation where it is possible to estimate the ray paths). As a result, each well test response is a result of some average conductance. From a single well steady state test, it is not possible to determine the arrangement of the conductors. Transient tests are a little better in that the volume which is controlling the average conductance is changing with time. So, we can say more about the possible arrangement of average conductance as a function of distance from the well. Tracer tests on the other hand are advection dominated and only the properties in the direct path are seen.

It is very important to realize that the parameters we derive from a well test interpretation

are always linked to the conceptual model, which is the basis of the interpretation and we can never be sure of the conceptual model. This means that any parameters derived from well test data are only as good as the conceptual model.

In order to use hydraulic data to determine the conceptual model and the associated parameters from hydraulic tests, a conceptual mathematical model for the behavior of the system is established by comparing the well test data to the behaviors of various classical conceptual models subjected to the same test conditions. Geologic and geophysical data may also be used to govern the choice of possible models. Once a model is adopted, the parameters of the model may be calculated by using an inversion technique developed for the model (eg. curve matching). In Section 5.2 below, we give an example of hydraulic testing at the FRI zone (see Section 4.3) that was interpreted in this classical manner using results of seismic tomography and geology to guide the interpretation. In this case several possible conceptual models were defined and compared to the data to help determine which conceptual model fits best.

5.2. An Example of Conceptual Model Testing at FRI

At the Grimsel test site, Nagra conducted hydraulic tests in conjunction with the seismic tests and geomechanical tests described in Section 3. In this section, we will describe how the information obtained by geophysical investigations was used to design hydrologic investigations. We then will discuss the results and analysis of the hydraulic tests. In particular, we will focus on an anomalous interference data and attempt to find an explanation for it. We will also try to relate the analysis to seismic test results.

The hydraulic tests were planned based on the 1987 tomography results. Packer locations are shown on Figure 5.1. Each test consisted of pumping water in the interval at a constant pressure and monitoring in all the other intervals. Objectives of each test were

(1) to find hydraulic connection with other zones,

(2) to characterize the properties of zones that are hydrologically active, and

(3) existence of zones about which we have only inconclusive evidence.
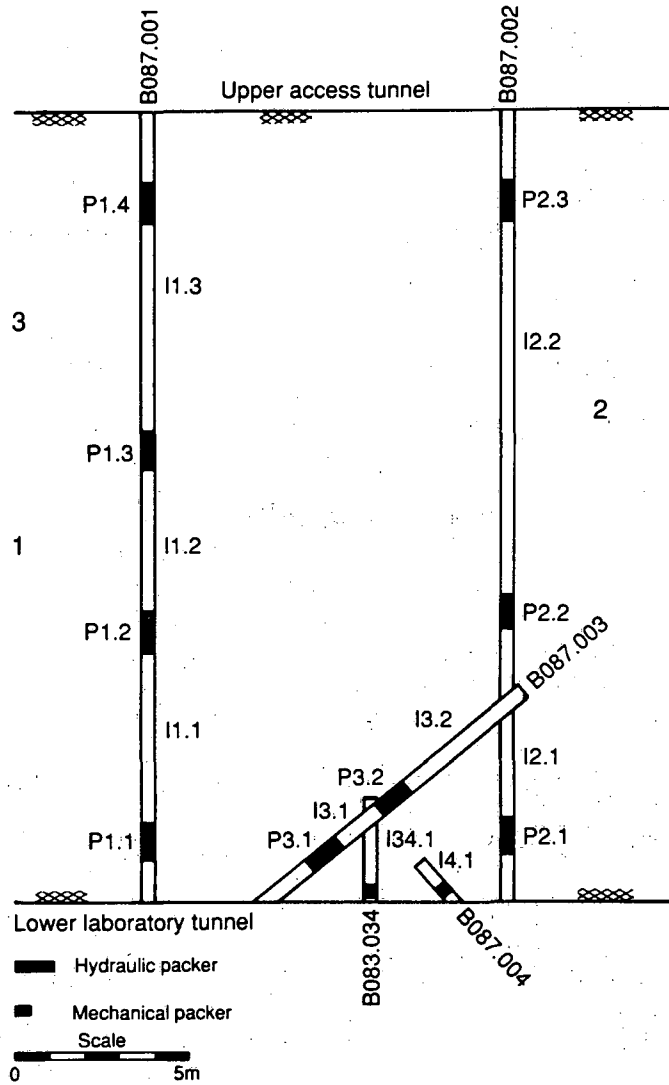
Figure 5.1. Packer locations used in Tests 1, 2 and 3.

The purpose of Test 1 was to provide a hydrologic characterization of a feature which is clearly evidenced by geophysics. The packers for Interval I1.2 were placed such that they confine the main fracture zone (corresponding to Feature A on Figure 3.6) as tightly as possible in order to minimize wellbore storage and isolate the hydrology of the feature. Interval I1.2 was used as the inflow interval and pressure was monitored in all the other intervals.

In Test 2, interval I2.1 was the source. The purpose of Test 2 was to see if the region to the north of I2.2 is hydrologically significant. The tomogram of Figure 3.6 showed this area to be a low velocity zone (Feature C). This test would only have been conclusive if the result were positive. A negative result would have meant that we did not find any connection between the low velocity region and any area being monitored. A positive test result would have been very significant because this feature had only been located with geophysics.

In Test 3, I1.3 was the source. Test 3 was designed to understand the south-eastern part of the shear zone. Feature A appeared clearly in the tomogram as extending across the tomographic plane. A parallel feature to the south-east appeared in BOFR87.021, in the BOFR87.002 core, and nearby in the tomogram. However, the tomogram did not indicate that this part of the shear zone is continuous. The test was designed to see if there is continuity or if a cross-cutting fracture connecting this part of the shear zone to I2.2 or I1.1 might exist.

5.2.1. Test Results and Analysis

The results of Tests 1, 2 and 3 indicated that Feature A is clearly the most significant hydrologic feature at the FRI site as expected. In Test 2, a coherent analysis is difficult because although I2.1 did take up some water and a weak interference was observed in some intervals, some intervals were still recovering from Test 1. Therefore, there is no good evidence that the low velocity zone to the north of I2.2 is hydrologically significant. Similar conclusions can be drawn for the Test 3 results. A weak but definite hydrologic connection between Interval I1.2 and I2.2 was observed. Although existences of cross-cutting features cannot be completely denied, one can postulate that their hydrologic significance is quite weak even if they exist. Readers interested in the details of the test results are referred to Wyss (1988).

Because the tests were conducted at constant pressures, we briefly present the analytical solutions for constant pressure test. The dimensionless pressure in Laplace space for a constant pressure test with skin in an infinite system can be written as:

$$\bar{h}_D(r_D, p) = \frac{K_0(p^{1/2} \cdot r_D)}{p[K_0(p^{1/2}) + s(p^{1/2}) \cdot K_1(p^{1/2})]}, \tag{5.1}$$

and for dimensionless flow, the solution is:

$$\bar{q}_D(p) = \frac{K_1(p^{1/2} \cdot r_D)}{p^{1/2}[K_0(p^{1/2}) + s(p^{1/2}) \cdot K_1(p^{1/2})]}, \tag{5.2}$$

where p is the Laplace space variable, s is the skin factor, r_D is the dimensionless radius, and K_0 and K_1 are the modified bessel functions of the second kind of zero-th and first order, respectively. The solutions in real space, h_D and q_D, can be obtained by inverting Equations (5.1) and (5.2) numerically (Figures 5.2 and 5.3). For references, readers may consult Carslaw and Jaeger (1946), Van Everdingen and Hurst (1949), and Ehlig-Echnomides (1979).

Figure 5.4 shows the pressure transient of interference data at various observation points in Test 1. Note that the Interval I3.1 responds most markedly. The response data at I3.1 is compared to the theoretical response obtained by evaluating Equation (5.1) at r = 10.2 m, or r_D = 10.2 m/43 m = 237 for s = 0 (Figure 5.5). As can be seen from the figure, the pressure observed at I3.1 is significantly lower than that predicted by the analytical solution, although the shapes of the curves are almost identical. The analytical solution assumes that the fracture is infinite, isotropic and homogeneous. Therefore, conditions must exist where one or more of the above assumptions are not appropriate. The plausible scenarios are:

(1) Skin: There is a low permeability zone around the injection well, i.e., a skin that causes the effective pressure at I1.2 to be lower.

(2) Anisotropy: The fracture is anisotropic with the maximum permeability direction is oriented vertically.

(3) Leakage: There is leakage from the fracture to the adjacent rock so that the pressure is more diffused.
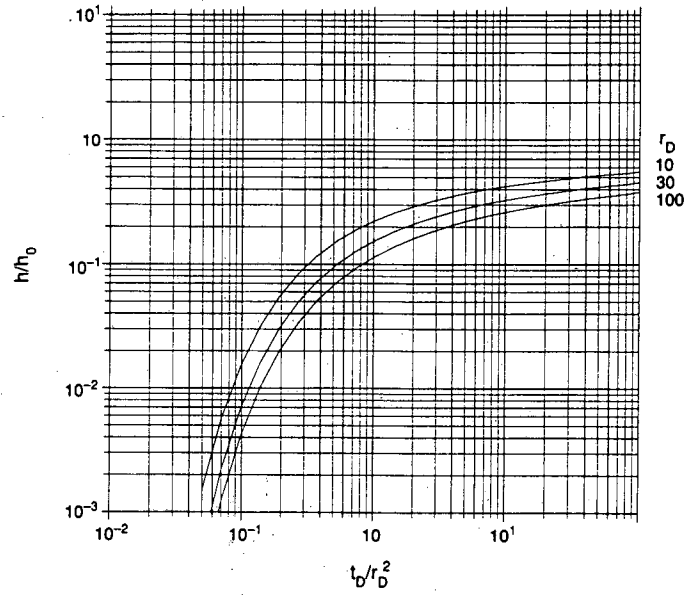
XBL 907-6448

Figure 5.2. Dimensionless head at $r_D = 10, 30,$ and 100.
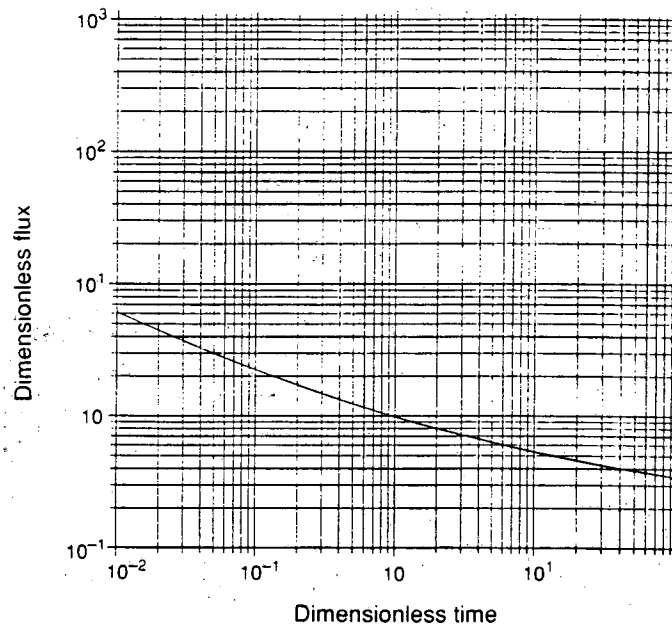
XBL 907-6449

Figure 5.3. Dimensionless flow at the well.
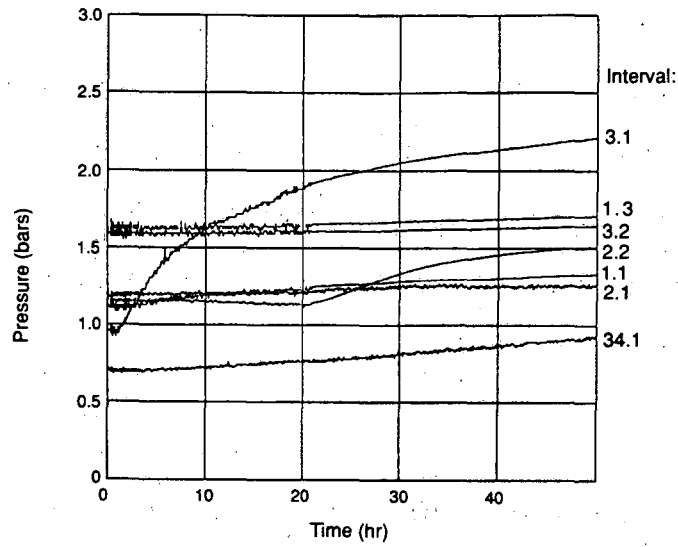
XBL 907-6451

Figure 5.4. Interference buildup data for Test 1 at various observation points.
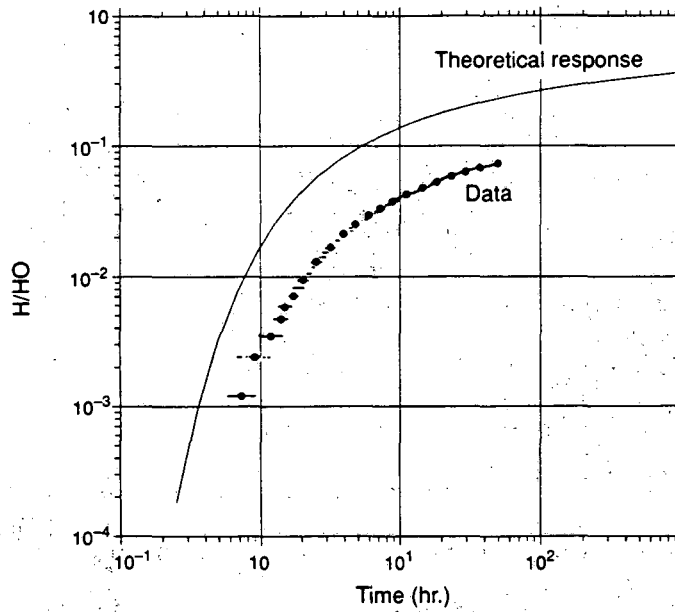
XBL 907-6452

Figure 5.5. Comparison between data and the theoretical response curve.

(4)   Boundary Effect: The boundary effect of the laboratory tunnel is keeping the pressure low at I3.1.

In the following sections, more detailed discussions will be given for each case, although in reality all of the above conditions may coexist. As is the case with any field experiment, the possibility of an erroneous measurement should not be completely discounted. For example, the pressure loss through the tubing may not be negligible. However, we will limit our discussions to the effects of the hydrologic features in the rock only.

5.2.2. Skin

Skin effect is usually suspected when anomalous results are obtained. Equation (5.1) can be used to obtain pressure response curves at I3.1 for various values of skin factor s. Figure 5.6 shows that the curve for s = 13 yields a relatively good match with the data except for the late time portion. An almost perfect match can be obtained by letting s equal zero and lowering the pressure in I1.2 6.6 bars instead of the measured values of 19 bars (Figure 5.7). This is equivalent to assuming that there is a constant pressure loss of more than 12 bars at the borehole wall. However, this assumption contradicts the conventional skin concept where the pressure loss is assumed to be proportional to the flow rate. Because the test was a constant pressure test, the flow rate in I1.2 varied with time as shown in Figure 5.8. As can be seen in the figure, there is an inflection point in the curve at around 0.18 hours, which cannot be explained by assuming an ideal homogeneous medium. Figure 5.8 also shows the dimensionless flow rate for various values of s. The curves are obtained by evaluating Equation (5.5). As can be seen from the figure, the flow rate curve does not match any of the skin curves. When considered in combination with the fact that the match for I3.1 is not very good, it seems that the conventional skin concept cannot explain the observed behavior. If a constant pressure drop is assumed at the borehole wall independent of the flow rate, the flow rate curve would look identical to that of no skin. Although the no-skin curve is closer to the observed curve, it still does not explain the inflection in the flow rate curve.
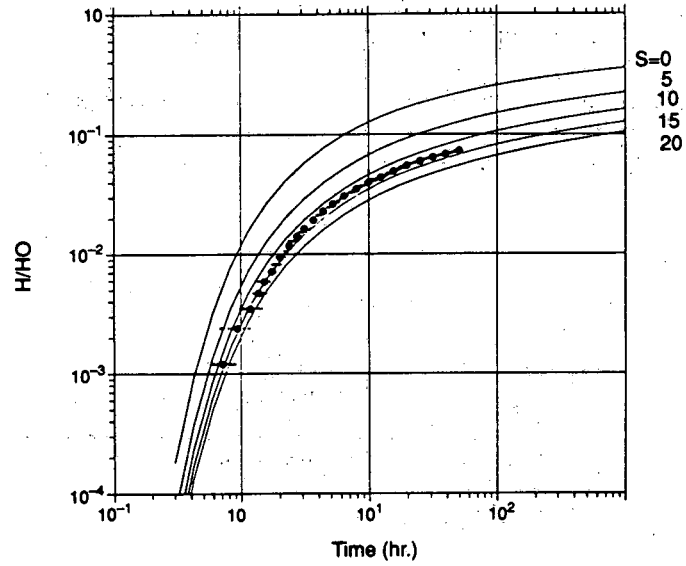
Figure 5.6. Type curve match with the skin curves.
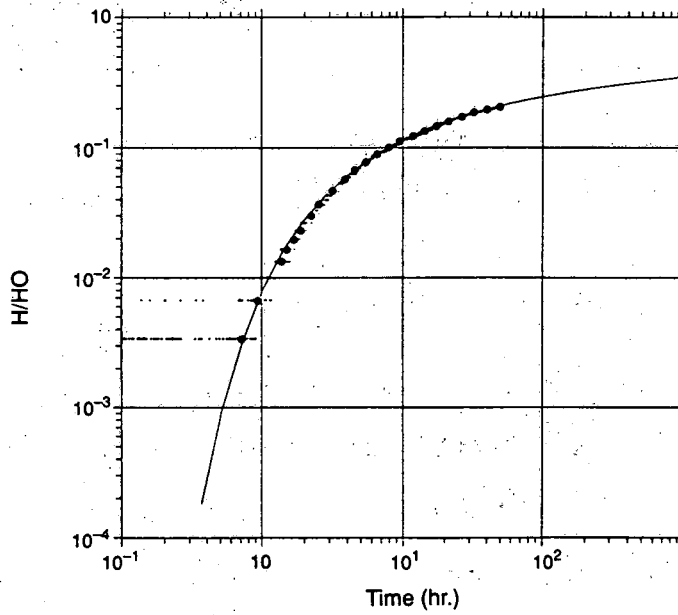
Figure 5.7. Type curve match assuming the lower injection head of 6.6 bars.
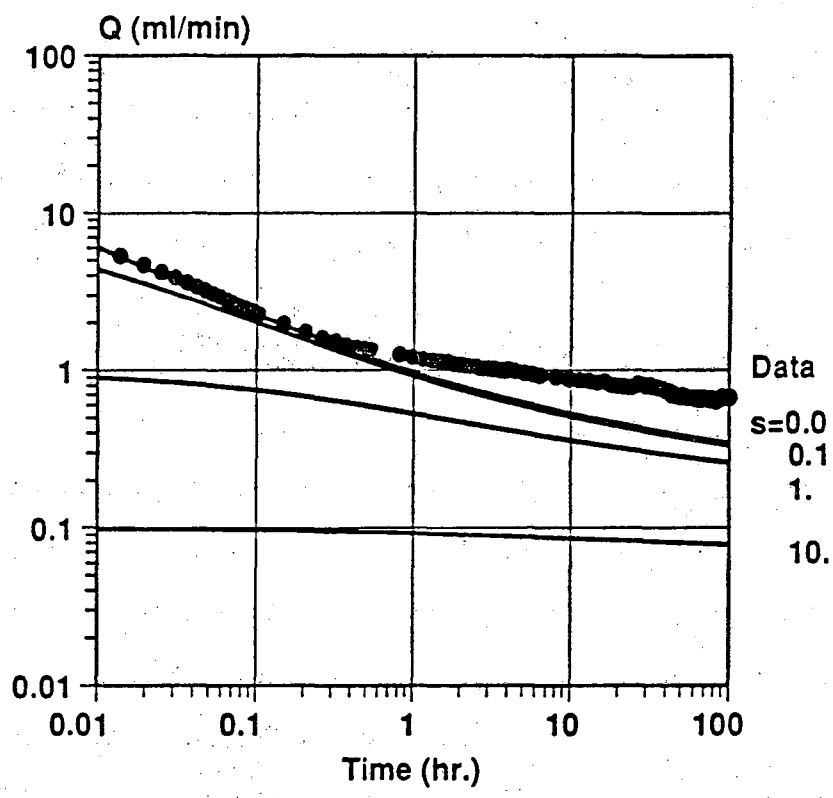
Figure 5.8. Flow rate decline curve observed at I1.2. Also shown are the decline curves for various values of s observed at I1.2.

5.2.3. Anisotropy

Geologic observations (Section 2) indicate that the fracture zone may be highly anisotropic with the highest permeability in the vertical direction. Thus, the injected water may flow preferentially in the vertical direction. As a result, observed pressure head in the horizontal direction at I3.1 may become lower than that in the isotropic case. In this section, the effect of anisotropy on the interference pressure is investigated.

Analytical solutions for flow to a well in an anisotropic medium can be obtained through a transformation of coordinates. The transformation of a coordinate is equal to the square root of the ratio of the permeability in its direction to the geometric mean permeability. In the transformed coordinates, the governing equation for flow becomes identical to that in an isotropic medium. However, the shape of the well becomes elliptical. Kucuk and Brigham (1979) solved the flow equation in the elliptical coordinate system. The dimensionless pressure outside the well producing at a constant pressure in the Laplace space can be written as:

$$\bar{h}_D = \sum_{n=0}^{\infty} (-1)^n \frac{1}{2\lambda} \frac{A_0^{(2n)} \mathrm{Fek}_{2n}(\xi, -\lambda)}{\mathrm{Fek}_{2n}(\xi_w, -\lambda)} \cdot \mathrm{ce}_{2n}(\eta, -\lambda), \tag{5.3}$$

where $\lambda = p/4$, $A_0^{(2n)}$ is a Fourier coefficient, ξ, and η are space coordinates in elliptical coordinate system, and $\mathrm{Fek}_{2n}(\xi, -\lambda)$, and $\mathrm{ce}_{2n}(\eta, -\lambda)$ are Mathieu functions. To obtain the exact value of the dimensionless pressure at I3.1, Equation (5.3) can be evaluated and transformed back to the Cartesian coordinate systems in the real space. Alternatively, an effective well radius can be used to approximate the elliptical well and Equations (5.1) and (5.2) can be used in the transformed coordinates. This approximation should be adequate because the dimensionless distance from I1.2 to I3.1 is large enough ($r_D = 237$) so that the elliptical shape of the well does not have much effect. Thus, a lower pressure than the theoretical pressure can be translated as a longer distance from the pumping well in the transformed coordinates. Figure 5.9 shows the dimensionless pressure at various r_D and the equivalent anisotropy ratio normalized to $r_D = 237$. As can be seen from the figure, an unreasonably large anisotropy ratio (2×10^9) is necessary to explain the pressure drop. Therefore, it is unlikely that anisotropy is the cause for the low pressure measurement.
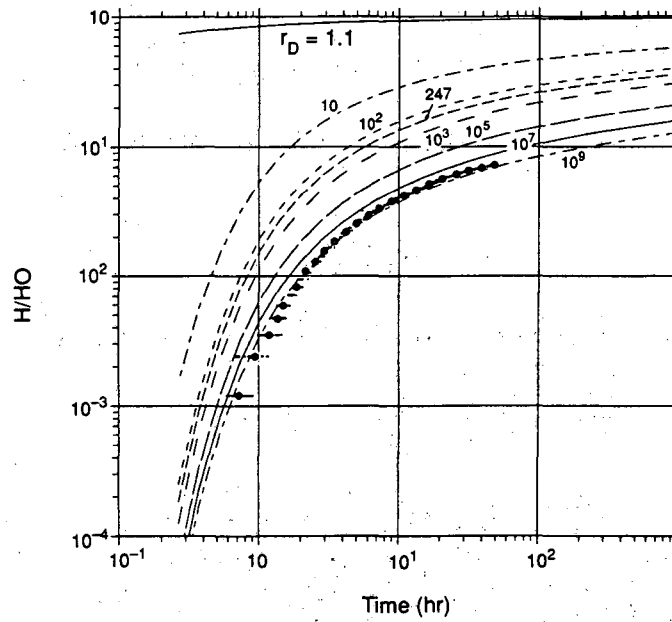
XBL 907-6456

Figure 5.9. Dimensionless pressure at various r_D and the equivalent anisotropy ratio.

However, this does not preclude the existence of anisotropy in general.

5.2.4. Leakage

So far, it was assumed that the flow is confined within the fracture zone. However, as can be seen from Figure 5.4, interference responses, although small, were observed at various intervals that are not in the plane of the fracture zone. This implies that there was a leakage from the fracture zone into the adjacent rocks, which may explain why the interference response at I3.1 was low. The solution for pressure under a constant pressure test in a leaky aquifer is not readily available in the literature. However, if the thickness of the rock that leakage occurs into is assumed to be a finite size and that the leakage is at quasi steady-state, the solution presented by Da Prat et al. (1981) for a double porosity medium can be used. Figures 5.10 and 5.11 show the type curve matches to the flow rate and the observed pressure at I3.1, respectively. Although the flow rate match is very good, the match with the observed pressure at I3.1 is not good at all. The theoretical pressure is too high compared to the data. This is because the rock is assumed to be a finite size.

Let us now consider leakage into an infinite size rock. The Laplace space solution for the normalized pressure in the fracture zone at a nondimensional distance, r_D under a constant pressure test with leakage into an infinite size rock can be written as:

$$\bar{h}=\frac{K_0\left[[(S_{sD}\delta p)^{1/2}+p]^{1/2}\cdot r\right]}{pK_0\left[[(S_{sD}\delta p)^{1/2}+p]^{1/2}\right]} \tag{5.4}$$

and the dimensionless flow rate at the well is simply:

$$\bar{q}_D=\frac{[(S_{sD}\delta p)^{1/2}+p]^{1/2}\cdot K_1\left[[(S_{sD}\delta p)^{1/2}+p]^{1/2}\right]}{pK_0\left[[(S_{sD}\delta p)^{1/2}+p]^{1/2}\right]}, \tag{5.5}$$

where S_{sD} is the ratio of the fracture specific storage to that of the matrix, K_D is the ratio of the hydraulic conductivity of the same, and $\delta=K_D/b_D^2$, where b_D is the ratio of fracture thickness to the well radius. Equations (5.5) and (5.4) are evaluated for various values of δ and plotted in Fig-
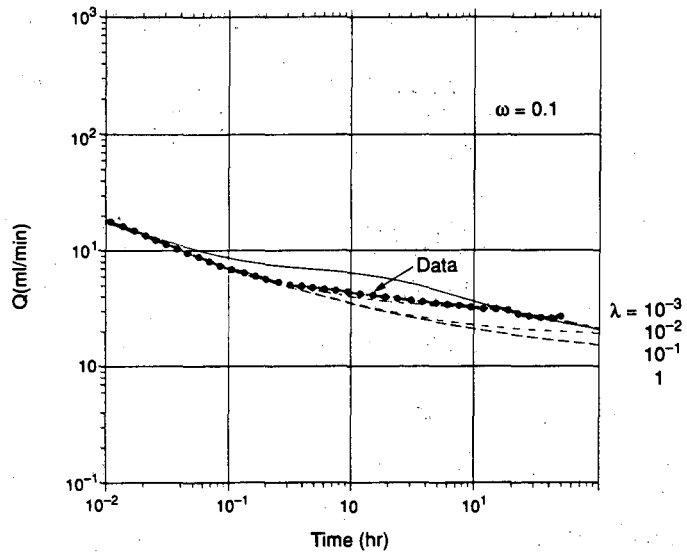
Figure 5.10. Type curve match of the flow rate with Da Prat et al. solution.
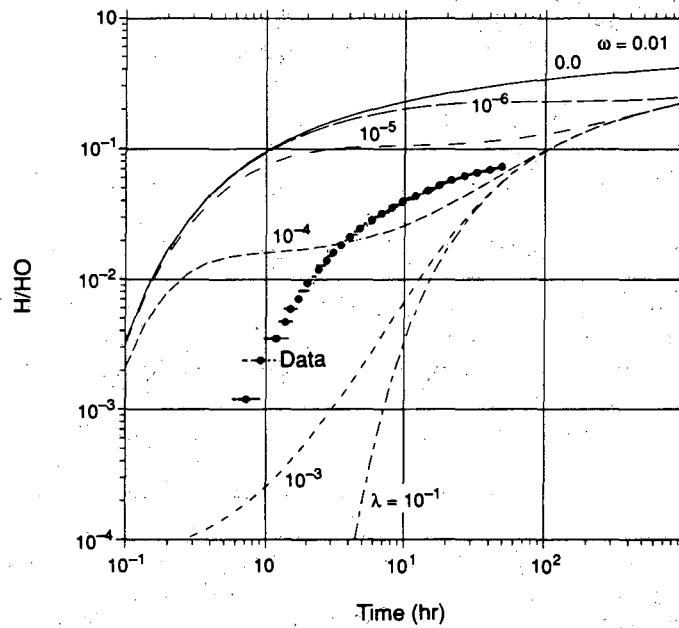
Figure 5.11. Type curve match of the pressure at I3.1 with Da Prat et al. solution.

ures 5.12 and 5.13 along with the observed data. As can be seen in Figure 5.13, the match with the interference data at I3.1 is now much better compared to the case of Da Prat's solution. However, the late time data of I3.1 is still not matched very well. Also, the observed flow rate curve is much flatter in the late time than the theoretical curves (Figure 5.12).

Nonetheless, the concept of leakage seems to explain the trend of the data: low interference pressure, and the flattening of the flow rate curve. The weak hydrologic connection between Interval I1.2 and I2.2 may be through this low permeability rock matrix. It is worth noting that the 1988 seismic tomography results indicate the existence of a Feature B that extends diagonally from the access tunnel toward BO87.001 (Figure 4.9). This may be the actual conduit of the leaking water. Although a localized leakage cannot be handled with an analytical solution, this would also explain the low pressure at I3.1, the flattening of the flow rate curve and the imperfect fit to equations 5.4 and 5.5.

5.2.5. Boundary Effect

In the previous analyses, the boundary effects of the tunnels were neglected. However, during the injection test it was observed that water was seeping out thorough the shot-crete along the zone where the FRI fracture intersects the access drift (Peterson, 1989). In this section, the effects of the drifts on the measured pressure is investigated. Because of the complexity of the geometry and the boundary conditions, a numerical model was used, where the FRI fracture is assumed to consist of a two-dimensional interconnected channel network (Figure 5.14). Both models were assumed to be initially at steady-state subjected to the same hydrostatic head. Then the node that corresponds to the location where the interval I1.2 intersects the fracture was opened to simulate the field test. Results of the simulated well test are compared using the cases with, one tunnel, two tunnels and without tunnels. Figure 5.15 shows the comparison of the pressures at I3.1 for these cases. As can be seen from the figure, the effect of the tunnels is felt at dimensionless time equal to 10. The curve for the case with the tunnels flattens and deviates compared to the case without the tunnels, as the pressure in I3.1 responds to the atmospheric pressure in the laboratory tunnel. However, the actual data shows little sign of flattening as can
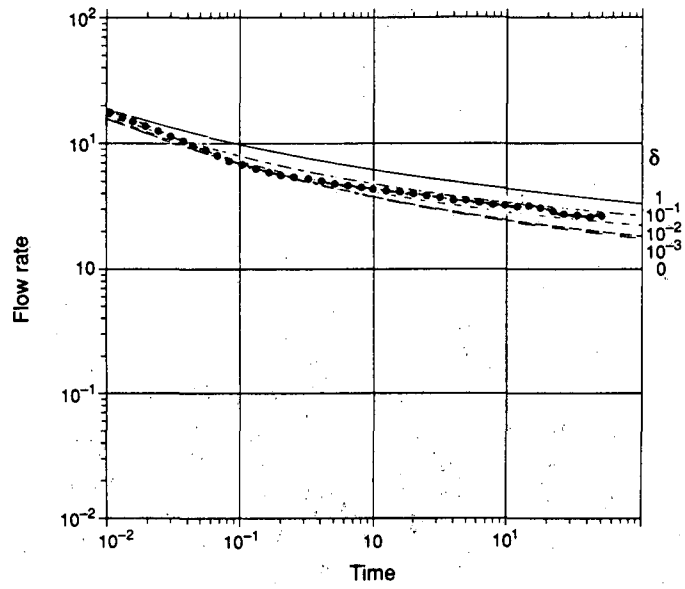
XBL 907-6463

Figure 5.12. Type curve match at I1.2 with a leaky fracture zone solution.
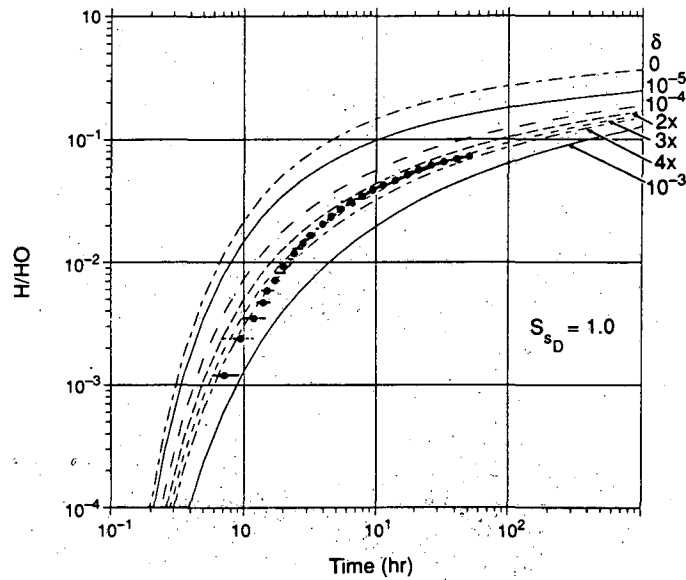
XBL 907-6459

Figure 5.13. Type curve match at I3.1 with a leaky fracture zone solution.

Laboratory
tunnel

Access
tunnel

45 m

45 m

I3.1   I1.2
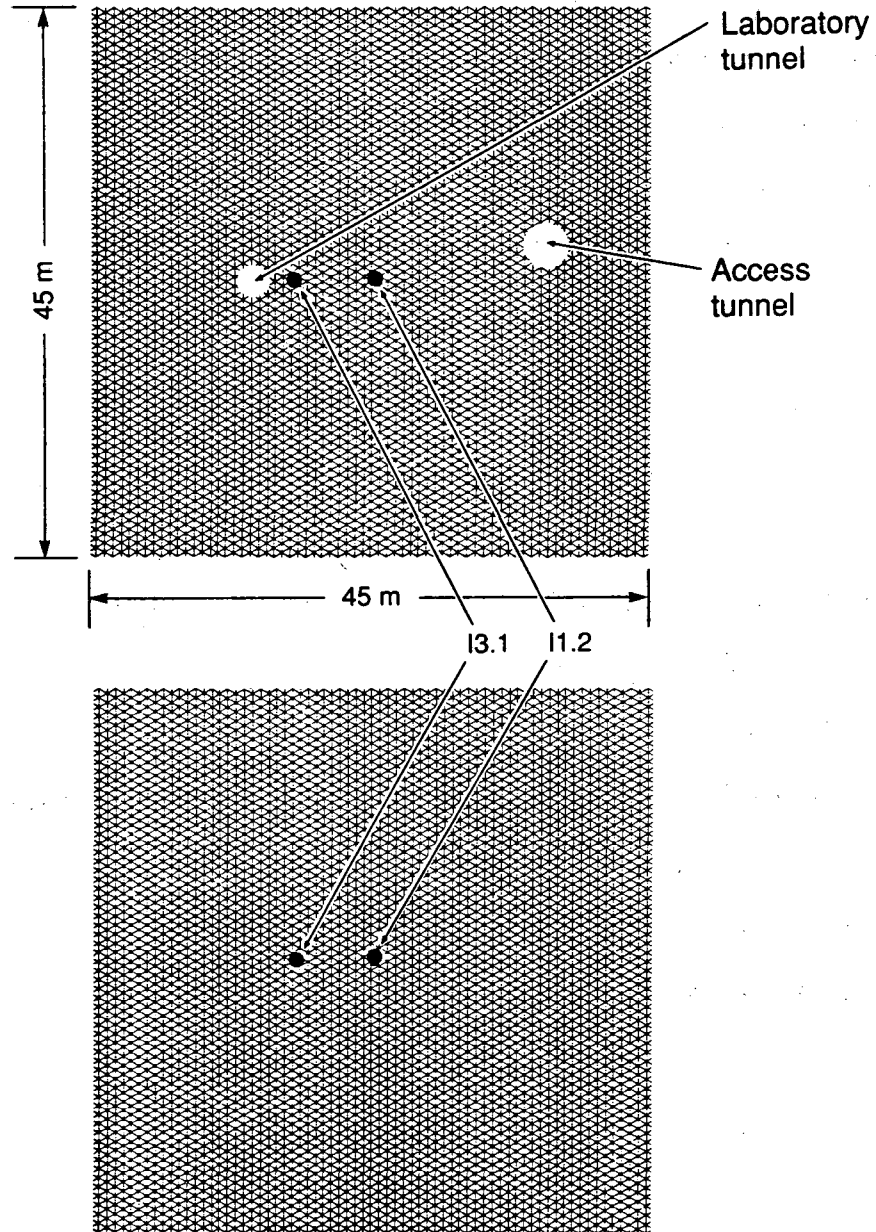
XBL 907-6460

Figure 5.14. Numerical model of the FRI fracture a) with and b) without tunnels.

be seen in Figure 5.4. The effect of the laboratory tunnel on the interference data at I3.1 seems to have been minimal which indicates that the permeability of the fracture around the laboratory tunnel is low. This agrees with the observation (Peterson, 1989) that no apparent increase of water seepage was noted in the vicinity where the FRI fracture intersects the laboratory tunnel during the injection test.

Figure 5.16 shows the comparison between the flowrates at I1.2 for the three simulations. This figure shows that the effect of the tunnels would be seen as a flattening of the flowrate decline curve. However, it is not as significant as the previous case. The inflection in the actual data cannot be explained by the effect of the tunnels alone.

5.5. Conclusions

The hydraulic tests have confirmed the hydrologic significance of the fracture zone which was previously identified by the seismic tomography. It appears that the majority of the flow occurred within the relatively thin fracture zone which connects interval I1.2 and I3.1. A weak but definite hydrologic connection between interval I1.2 and I2.2 was also observed. Feature B identified by the seismic tomography that extends diagonally from the access tunnel to BOFR87.001 may partially explain this hydrologic connection.

Because of the anomalous interference and flow-rate data, four different scenarios that differ from the ideal conditions were examined. They are 1) skin, 2) anisotropy, 3) leakage, and 4) boundary effects. Although it is possible for all of the four conditions to coexist, the most plausible scenario seems to be the leakage effect outside of the fracture plane.
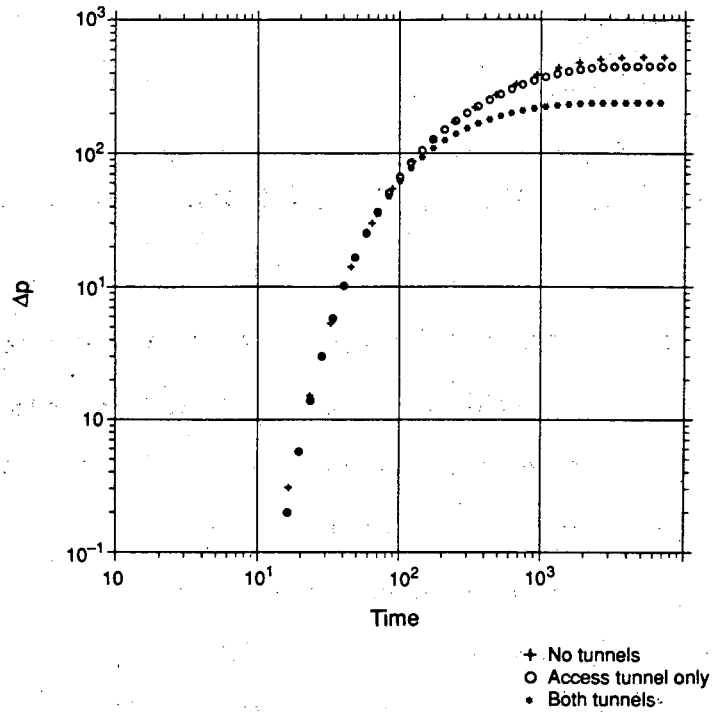
Figure 5.15. Comparison of the three simulations for the pressures at I3.1.
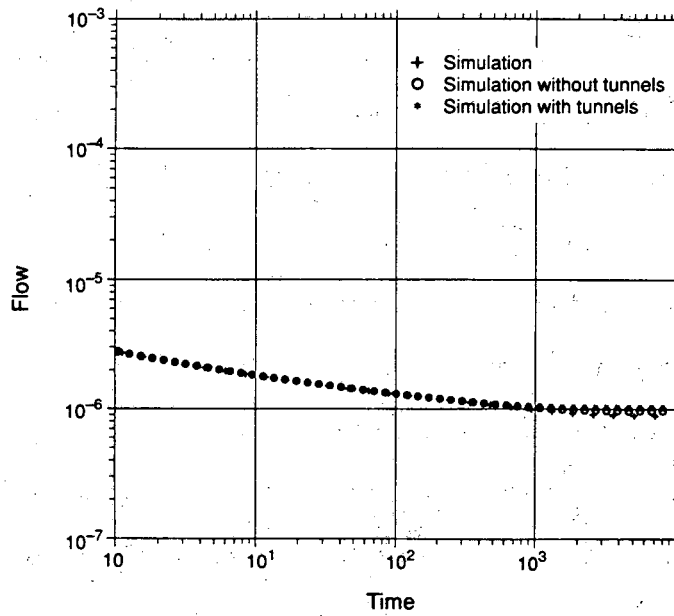
Figure 5.16. Comparison of the three simulations for the flow rates at I1.2.

6.0. CONSTRUCTION OF THE HYDROLOGIC CONCEPTUAL MODEL

Once the geologic, geophysical, and hydrologic techniques have been applied the stage is set to specify the hydrologic conceptual model. For our purposes, the hydrologic conceptual model is taken to be a description of the geometric relationships between conductive elements of the hydrologic system. To go from the conceptual model to a predictive model, it remains to parameterize these elements. In this report we discuss the use of inverse techniques (Section 7) for parameterization. An alternative is to present a stochastic conceptual model and use statistical simulation to obtain predictive models. This approach is not discussed here, but for sites where the fracturing is more gradational, statistical simulation may play a larger role in model development (as mentioned in Section 1). The two approaches are not exclusive: inversions can be designed based on the parameters of the simulation. In this case, the inversion controls the simulation such that a model is obtained which honors both the statistical data and the observed hydrologic behavior. Such a combined approach is under development and may prove to be very powerful. For the inverse technique, "simulated annealing," described in Section 7, the goal in creating this model is to include hydrologic conductors in all the places that they are likely to be. It is not a problem to include more conductors than are actually active. It could be a problem to leave out a potential pathway. This is because the "simulated annealing" will pick those conductors among the possible conductors that can best explain the hydrologic responses observed in the rock. So our aim in creating the hydrologic conceptual model is to specify a set of conductors that hopefully include all the important flow paths. This is a straight forward approach, probably best suited for sites where fracture zones are distinct and clearly dominant.

6.1. An Example from the Stripa Mine

As an example of conceptual model development, we describe a process used for a block of rock in the Stripa Mine in Sweden called the SCV (Site Characterization and Validation). This conceptual model was designed as a platform for simulated annealing.

Extensive geophysical data was collected on the SCV block through five boreholes (W1, W2, N2, N3, and N4) as shown in Figure 6.1. An integrated analysis of radar and seismic data was used to identify major features (Olsson et al., 1988a,b). It is notable that the geologic side of this process was not included in this particular analysis. Nevertheless, it was possible to come up with a picture based on geophysics alone.

The features in the SCV block were assumed to be planar fracture zones. Normally, a feature is first identified in the tomograms and then the borehole intersections are estimated. These borehole intersections can usually be identified with a reflector from the single-hole reflection analysis. The possible orientations from the reflection data are displayed in a Wulff diagram. A pair of possible planes are determined by the two possible orientations which lie on the locus of possible reflectors and also lie in the plane of the tomogram. If the feature is visible in both the N2-N3-N4 plane and the W1-W2 plane, then there is a further three-dimensional check on the geometry.

In a similar manner, the crosshole reflection data is checked to see if it is consistent with the location and orientation of the zone. Such analysis was performed for both the radar and the seismic data. Then all the data was integrated to obtain four major fracture zones; A, B, H and I and a minor zone, C, as discussed in Olsson, et al. (1988a). Some of these zones are shown on Figure 6.2 superimposed on an example radar tomogram. Table 6.1 represents these results with a qualitative classification of the strength of the anomalies associated with the zones made in three classes: S, Strong; M, Medium; and W, Weak. Table 6.1 also includes zone B' which is discussed below.

Figure 6.3 (after Olsson et al., 1988a) gives an example of the borehole data acquired for the N- and W-holes. The geophysically defined features are shown on the plots as horizontal

Macropermeability
drift

3D migration drift

N4

W1

W2

N2

V3

Future
validation
drift

Site
characterization
and validation
drift
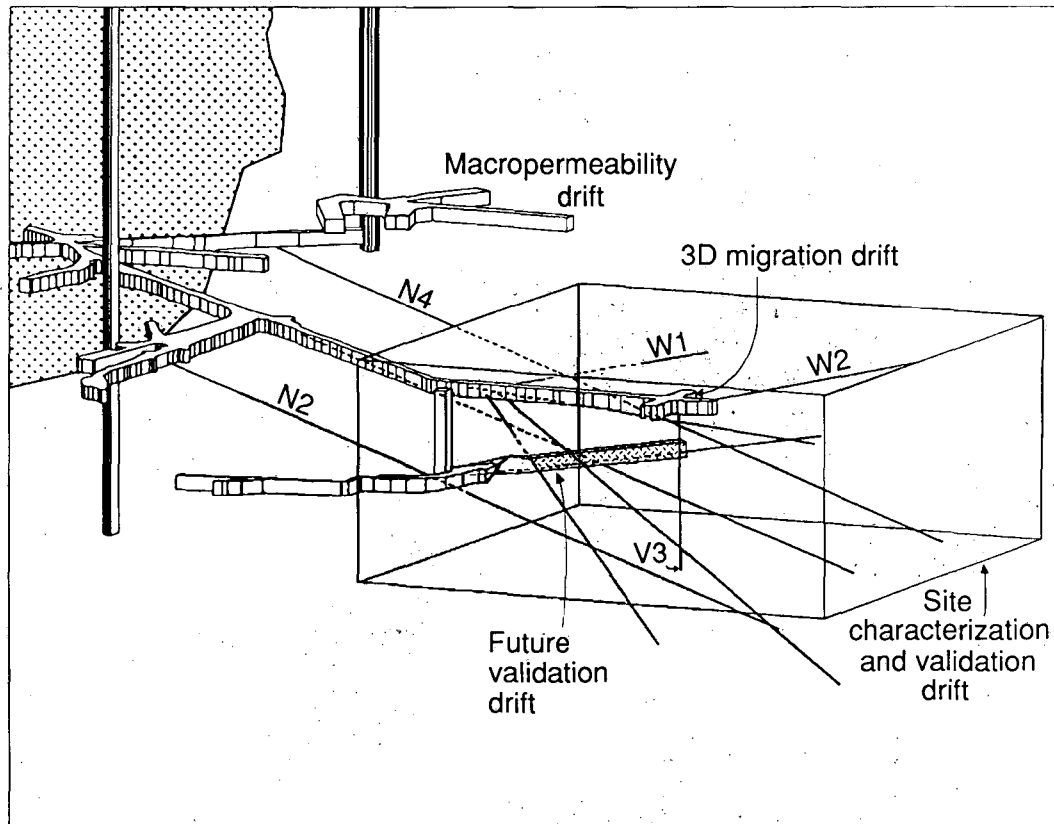
XBL 897-2676

Figure 6.1. Perspective view of the SCV block. Dotted area in the upper left is the mined out
stopes (after J. Gale).

N2 N3 N4 22 MHz RESIDUAL ATTENUATION (dB/km)
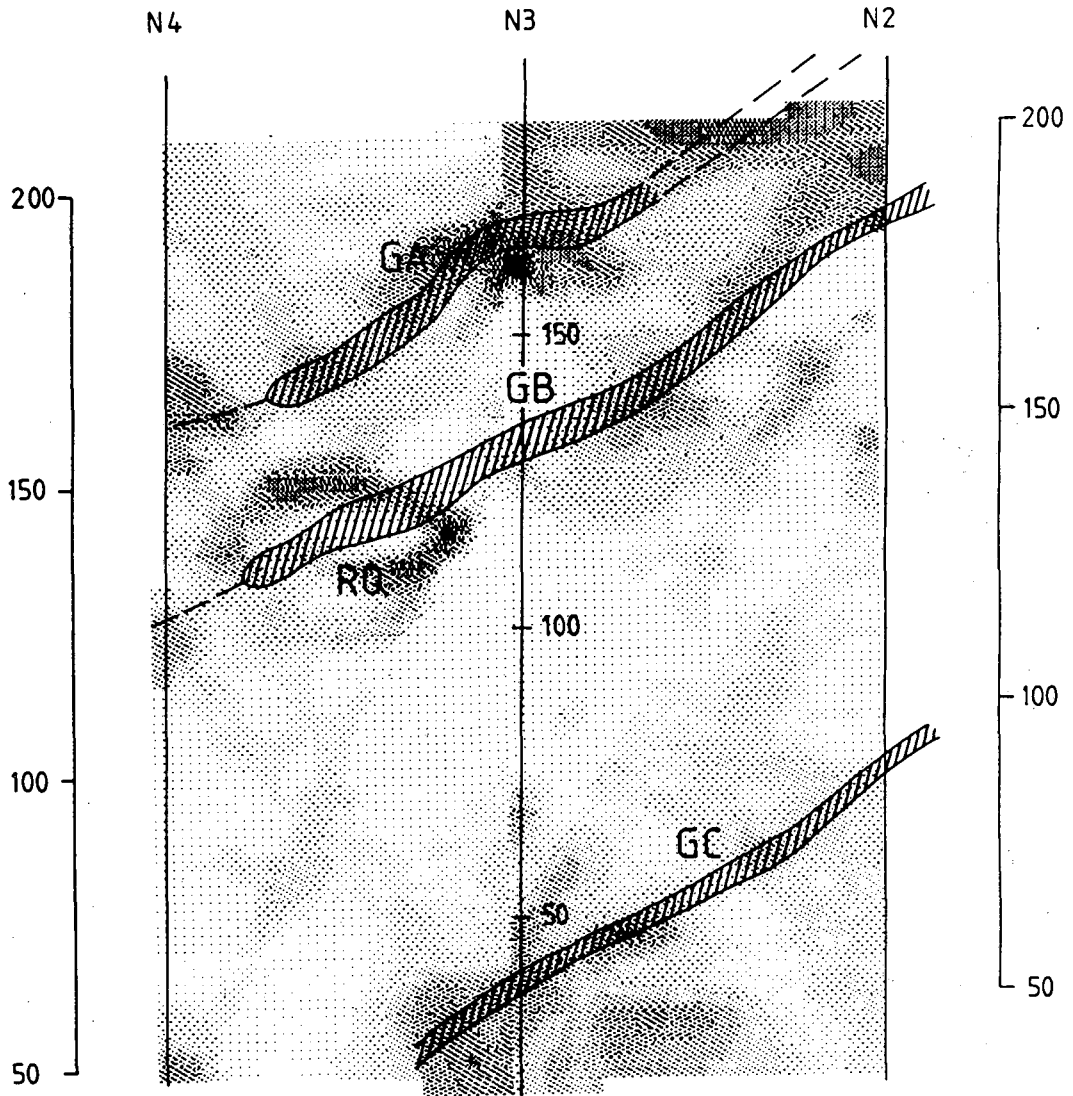
XBL 896-2394

Figure 6.2. Example radar attenuation tomogram between holes N4 and N2 showing predicted fracture zones A, B and C (Olsson, 1988a).

N 2
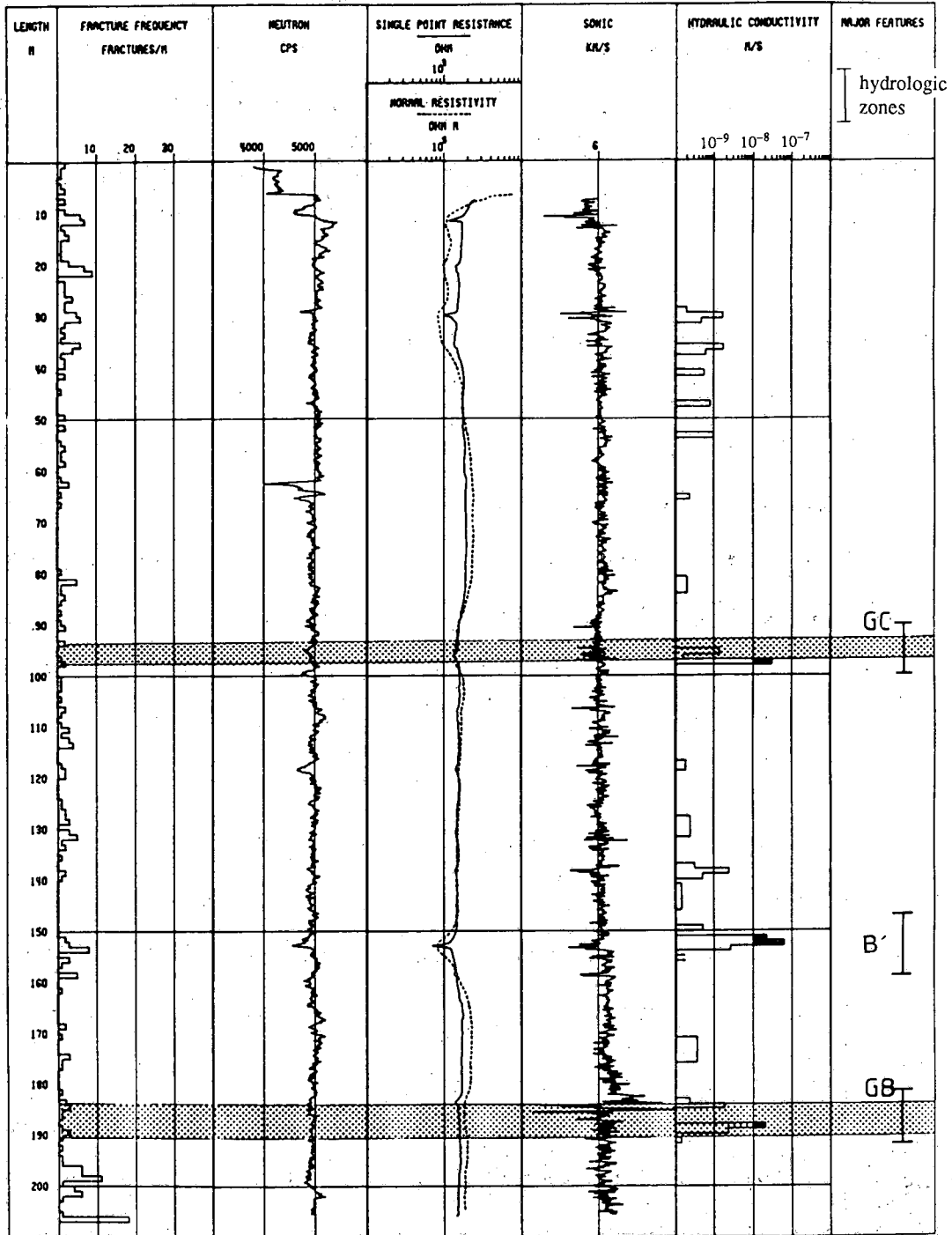
XBL 896-2387

Figure 6.3. Summary data sheet for N2. Hydraulic conductivities greater than 10^{-8} m/s have been blackened in. Hydrologic zones are marked in the right hand column.

bands. Under the hydraulic conductivity column, we have blackened in those conductivities greater than 10^{-8} m/s. If these features are taken to have a width of about 10 m, they account for about 60% of the measured hydraulic transmissivity measured in the boreholes (Table 6.2). Almost all of the remaining 40% of the transmissivity is accounted for in three zones: at 80 min borehole W2, 152 meters in N2 and from 80 to 90 meters in borehole N4. There are strong radar and seismic anomalies at each of these zones as well as supporting evidence from geophysical and core logs.

Initially, we tried to account for these hydrologic features by altering the orientations of the six major zones by an amount consistent with the geophysics. After determining that no improvement was possible, another zone, B', was added to explain previously unaccounted for hydrologic anomalies in N4 and N2. Figure 6.4 shows a perspective plot where zones B and C are represented as dots located on planes. In this figure we are looking along the B and C planes so that the zones appear as dots clustered along a line. In this perspective, one can see that the hydrologic anomalies in N4 and N2 lie on a plane roughly half way between zone B and zone C. For this reason, we chose B' to be a plane between B and C and parallel to the A, B, and C zones. The addition of B' increases the percentage of transmissivity accounted for to about 78%.

The fact that no similar hydrologic anomaly is seen in N3 (between N4 and N2) is not a problem for this model. This can easily be accounted for if no permeable channel from B' intersects N3. We are more concerned with insuring that channels are possible where hydrology has been observed. Extra channels can always be made inactive in the annealing process described in Section 4.

The B' zone also fits in well with the geophysical results. The radar results show a very strong low velocity zone in the section N4-N3 slowness tomograms corresponding to the feature at 90 m down borehole N4 (Figure 6.5, from Olsson et al., 1988b), as well as single hole radar reflectors on either side (Olsson et al., 1988b). In Figure 6.5, our B' feature is located at the point labeled "RB" (R for radar). This is due to the original radar interpretation putting zone B in this location. (Later, the integration of radar and seismic results put zone GB (G for geophysics) up to

Table 6.1. Geophysical fracture zones

Zone	Radar	Seismics	Geoph Logging	Core Logging	Hydrologic
A	S	S	M	M	W
B	S	S	M	M	M
B'	S	S	M	W	S
C	M	S	W	W	W
H	S	S	M	S	S
I	M	W	M	M	S

Table 6.2. Hydraulic transmissivity distribution

Hydraulic Transmissivity (10^{-9} m^2/s)						
Zone	W1	W2	N2	N3	N4	Total	% of total
A	-	99	-	0	1	100	3.2
B	0	88	20	12	5	125	4.0
B'	-	-	80	0	450	530	17.1
C	-	-	36	0	0	36	1.1
H	120	950	-	-	-	1070	34.5
I	25	510	-	-	-	535	17.2
(HB*)	-	670	-	-	-	670	21.6
Sum	145	2317	136	12	456	3066	98.7
Total transmissivity						3100	100

* Transmissivity between zones H and B in borehole W2
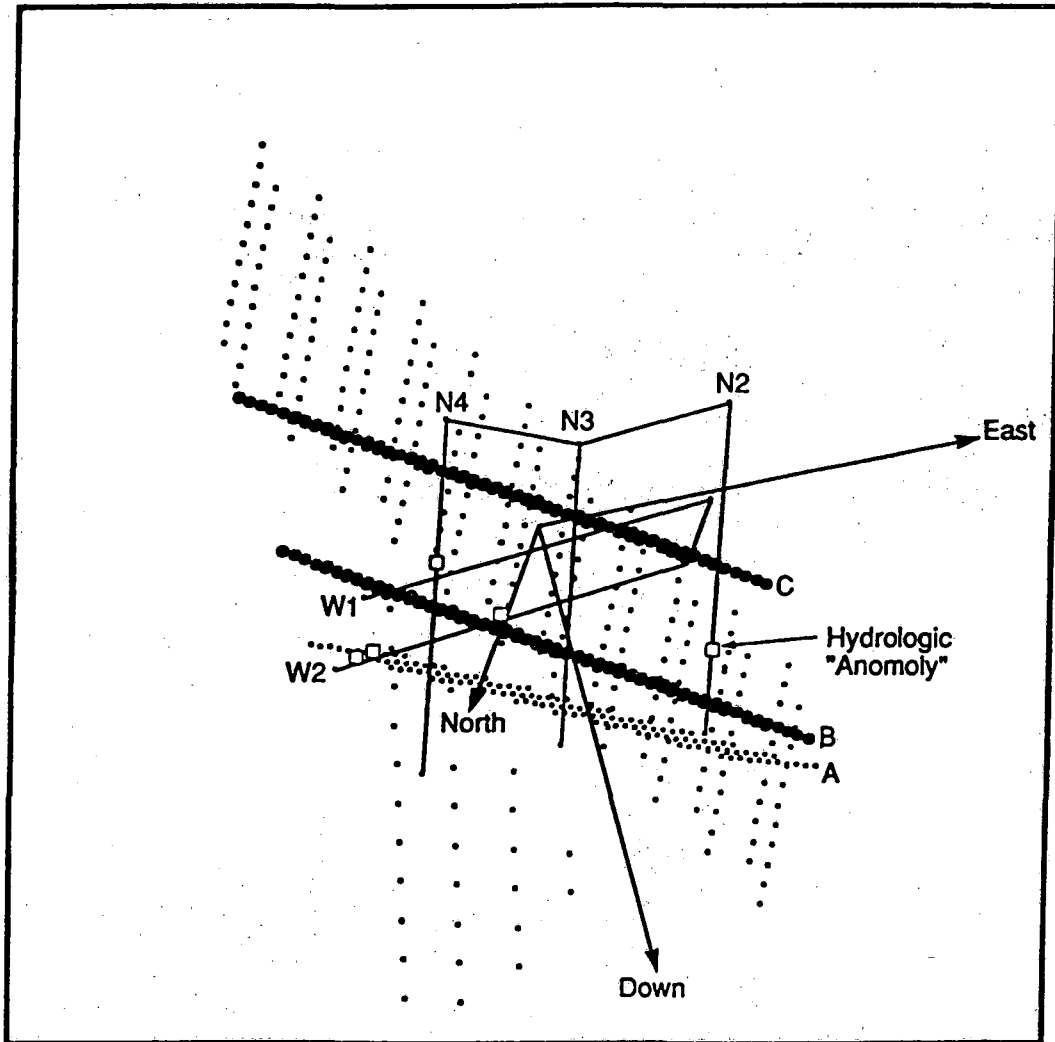
Figure 6.4. A perspective view of the SCV block looking up to the North-East showing zones B and C and that two hydrologic anomalies lie between these zones in the plane parallel to them.
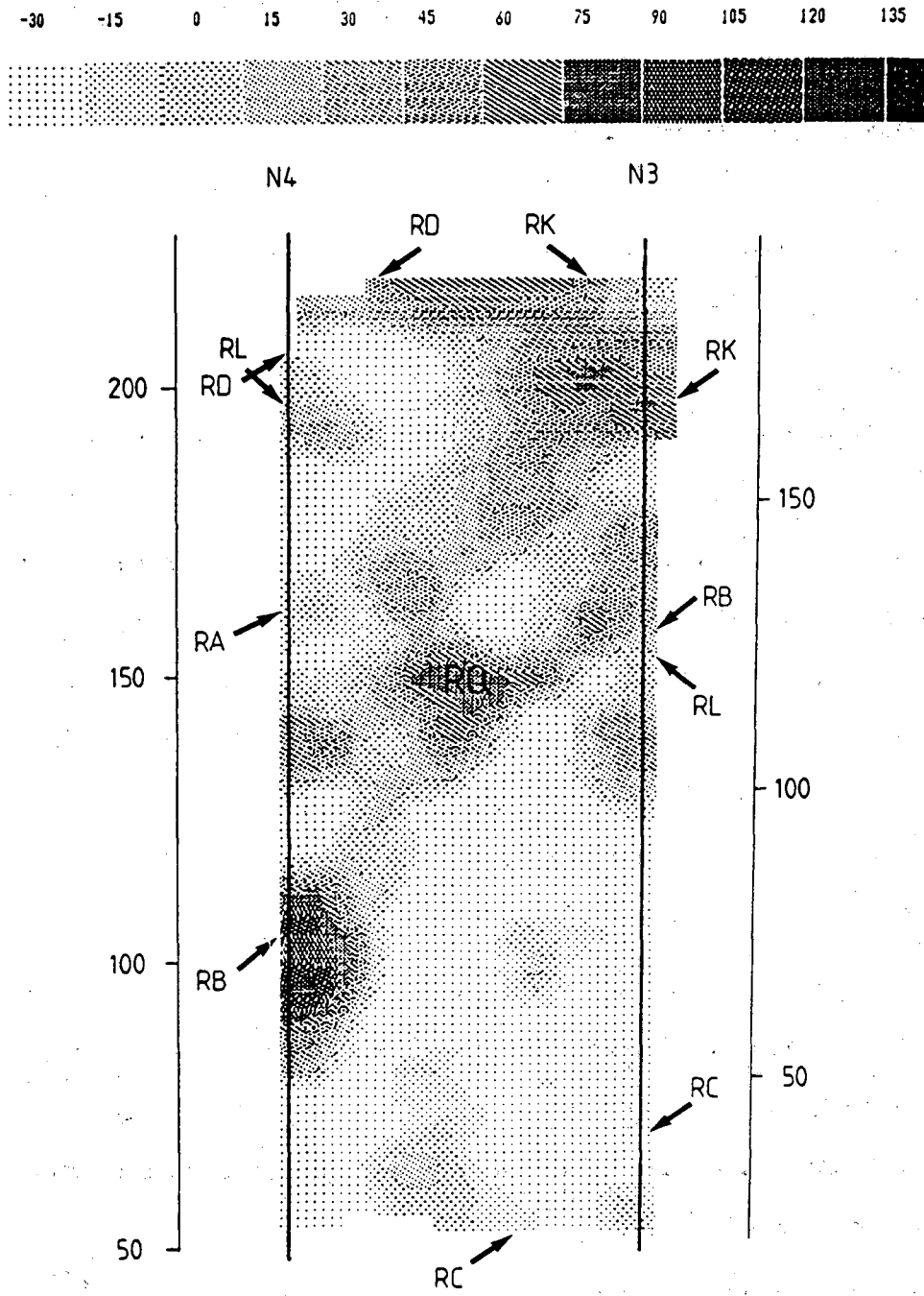
XBL 896-2392

XBL 896-2397

Figure 6.5. Residual radar slowness tomogram for the borehole section N3-N4 made with a center frequency of 22 MHz.

just below where zone RA is on Figure 6.5. The tomograms for section N2-N3 are not available, but several strong reflectors are observed at the 152 m region down borehole N2. The B' feature is not apparent in any of the attenuation tomograms or the section N2-N4 slowness tomograms.

The B' feature may be related to the RQ feature shown on Figure 6.5. This tomogram shows the B' (or RB) anomaly begins to peter out about 20 meters from the borehole. It appears that it may intersect the South edge of the RQ feature. The feature B then skirts the North edge of RQ and produces the largest hydrologic anomaly in N3. It may be that RQ is a step between *en echelon* fracture zones represented by B' and B. This would also explain the lack of hydrologic activity in N3 at B'. However, it does not explain why B' is again the largest anomaly in N2 unless there is another step in the opposite direction.

One remaining anomaly in W2 between zones H and B (called HB* in Table 6.2) accounts for 21.7% of the transmissivity. If we allocate this transmissivity partly to H and partly to B, then we have accounted for 98.7% of the observed transmissivity with a zone model. This makes a certain amount of sense when we consider that the transmissivity measured in the boreholes is not strictly additive. Figure 6.6 illustrates that successive borehole tests are actually sampling some of the same transmissivity. It is easy to imagine that the high conductivity found between zones H and B in W2 is due to a few conductive features that are related to H and B and possibly related to the intersection of H and B.

The resulting hydrologic zone model is shown in Figure 6.7 in a perspective view from the North-West. The zones are disc-shaped planes. As we do not expect the zones to be uniformly permeable, within the block, the zones are discretized into flow channels. Any type of discretization could be used. We base the choice of grid with the support of geomechanical investigations of the shear zones explained below.

Slickenside striations in the two sets of fracture zones indicate that they have undergone shear deformation. Utilizing a database consisting of 3100 logged fractures from borehole core and 900 fractures mapped on the walls of underground drifts, the character of these fracture zones have been analyzed. This data, along with numerical fracture mechanics modeling, suggests that
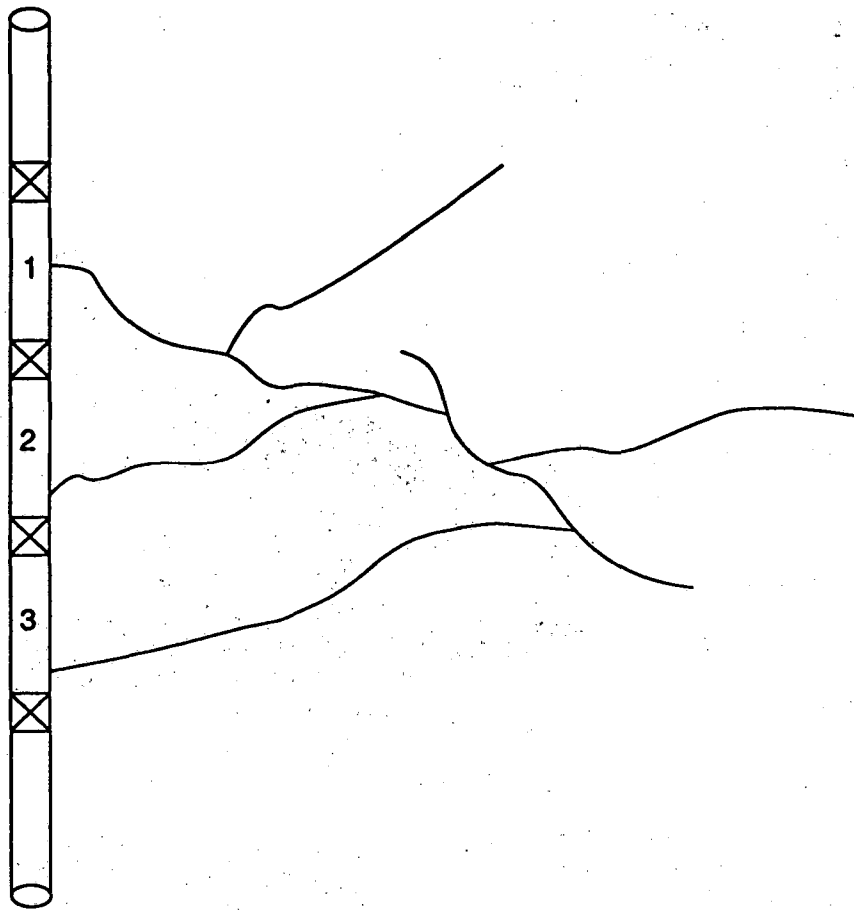
XBL 908-2793

Figure 6.6. Hypothetical testing zones in a fractured rock showing that the transmissivity measured in the three zones will overlap such that the transmissivity measured separately will add up to more transmissivity than the true total.
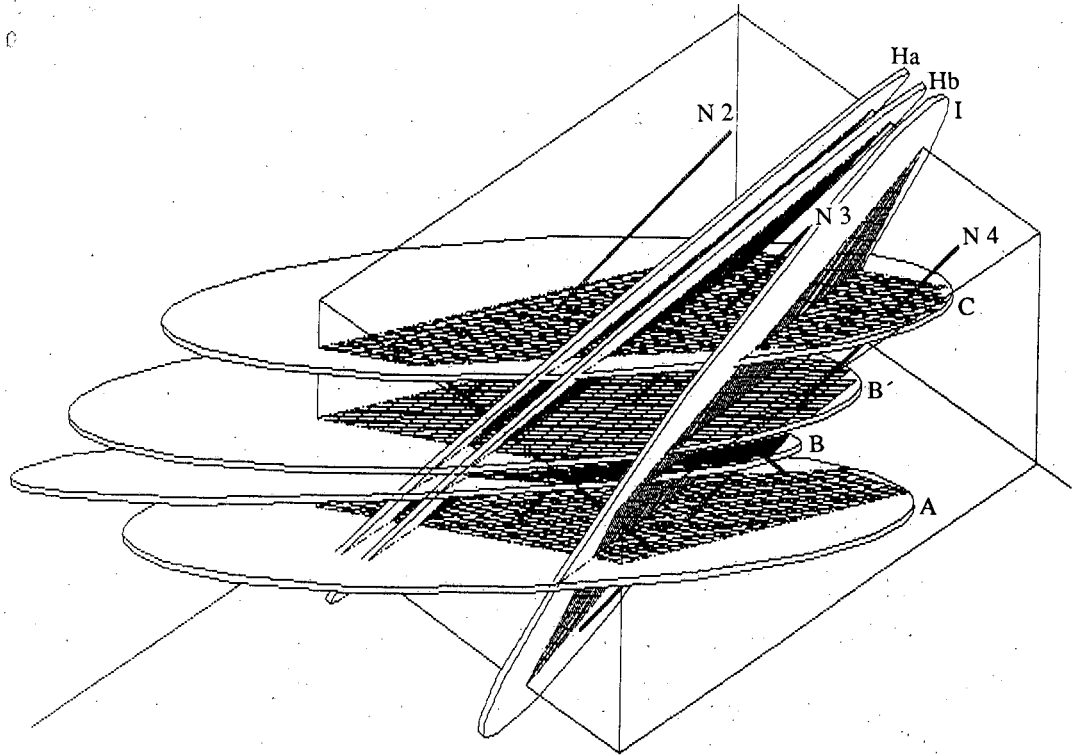
XBL 896-2396

Figure 6.7. The hydrologic zone model shown in perspective from the North-West looking
down. Zones A, B, B', C, Ha, Hb and I are shown. Gridding on the planes
represents the hydraulic conductors of the template used for annealing.

the higher fluid conductivities in the zones compared with the surrounding rock may be due to a combination of higher fracture densities, and stresses in the zones that promote dilatancy in fractures with certain orientations. This would also result in anisotropic flow in the zones, with the primary flow direction in the direction of the dilatant fractures.

For the NE-striking, low dipping zones, the secondary fractures are sub- horizontal, and for the N-S striking, steeply dipping zones, the secondary fractures strike N-S and dip 10-40° to the east. Numerical modeling indicates that under the present stress state in the SCV block, the sub-horizontal secondary fractures could be open and have a much higher conductivity than other fractures in the SCV block. This, along with the higher fracture densities in the zones, may explain why the conductivity in the zones is greater than the surrounding ground. Also, this will cause anisotropy in flow in the zones, with preferred pathways in the direction of the secondary fractures. Though not discussed in this report, there is evidence that zone intersections may be important in controlling flow through the SCV block. Future work looking at the properties of zone intersections is recommended.

Based on this work, we chose a zone model where the zones are modeled as planes. The planes are discretized using a square grid of conductors to form the possible paths for fluid flow. The grid elements are constructed along strike and dip lines. In this way, we allow for the horizontal conductors indicated by the geomechanical observations. Each grid element is assumed to have the same conductance, so if the geomechanical observations are correct, we expect that fewer of the dip direction elements will be active, i.e. permeable than those in the strike direction. In order to determine which of the grid elements are active and which are inactive, we use "simulated annealing" to find the pattern of conductances which cause the model to behave in the way the the insitu tests behaved. This is described in Section 7.

7.0. SIMULATED ANNEALING

LBL has been developing an inversion technique called "Simulated Annealing" which can be used to construct a system which is functionally equivalent to the observed system: i.e., a model which simulates the observed behavior. We describe here how to use annealing to find an equivalent fracture network model. The fracture network model is "annealed" by continually modifying the base model, or "template" such that the modified systems behave more and more like the observed system.

Hydrologic inversion models developed in the past, such as the conjugate gradient method, or maximum likelihood method (Carrera and Neuman, 1986), were focussed on determining the conductivity values in the equivalent continuum or porous medium case. Annealing could theoretically be used to do this type of inversion, but might be relatively inefficient in this role. On the other hand, these equivalent continuum techniques work poorly when they are asked to completely turn off the conductivity of a portion of the region. Thus, they are not the technique of choice for poorly connected systems, such as fracture systems, when we wish to determine how the conductive features are connected.

We think that the pattern of conductors is responsible for the first order hydrologic behavior of fracture systems. In other words, it is most important to know how the system is connected and to next determine the variability in conductance. We use a template, a collection of simple flow elements or channels, to build a model with connections equivalent to those in the field.

In simulated annealing, we search for patterns of conductors which behave like the observed field system. To do this, we set up a "template" of allowed conducting elements. Then we look at different configurations of these elements by turning some of them off, i.e. making them non-conducting. For each configuration we can compute the behavior of a well test that was also

conducted in the field. The "energy" of the configuration is then defined as a function of the difference between the observed and the simulated response. The problem of finding the appropriate model now becomes one of finding configurations which have low values of the energy function. Searching for a low energy configuration is a difficult task because there are many possible configurations.

The simulated annealing algorithm starts from some arbitrarily selected configuration and computes the energy, which is proportional to the difference between observed and simulated values. Then an alternative configuration is selected, and the energy for this configuration is computed. If the alternative energy is lower than the energy for the current configuration, then the alternative matches the observed data better, and the algorithm will decide to move to the alternative configuration. This is analogous to a downhill step. An "uphill step" to an alternative with a higher energy function will be taken randomly, with a probability which depends on the amount of increase in energy incurred by the step and on a weighting parameter called the temperature. The temperature, T, is decreased as the number of iterations increases to make it more and more unlikely that an unfavorable change will be accepted.

The simulated annealing algorithm incorporates temperature changes such as those used by Metropolis et al. (1953) and an appropriate energy function (Kilpatrick, et al., 1983; Tarantola, 1987). The temperature is held fixed for a certain number of configuration changes and then lowered. At first, a high value of T allows the algorithm to jump out of local minima and continue searching for a better region of the function. Later, lowering the temperature tends to confine the search for a minima, so the algorithm can converge.

7.1. Annealing Theory

To use simulated annealing on a general problem, one needs a set of possible configurations, a way of randomly changing the configurations, a function one would like to minimize, and an annealing schedule of temperature changes (Press, et al., 1986).

Let

Q = an energy function

C = a configuration of elements

M = the finite set of all possible elements, ordered from 1 to M.

We can define the set of all possible configurations using our template or base model; *M*, the set of all possible pipes or channels. The channels have two possible states: they are either on or off, i.e. conducting or nonconducting. The set of all possible configurations is the set of all combinations of on and off pipes. Let C = $\{C_m, m = 1 \ldots M\}$ denote a configuration of on and off pipes, where C_m is a binary random variable associated with each pipe.

We now must decide how to change the system. We choose to try removing or replacing one randomly chosen conductor at a time. Thus any new configuration, C^i, will vary only slightly from C, that is C^i will be in the neighborhood of C. Consider some configuration C. We will use some probability function to randomly select a pipe. If the pipe is on, we turn it off, and if the pipe is off, we turn it on. The neighborhood of C should contain all configurations one step away from C with one pipe missing or one pipe added. Let

$\{C^i\}$ = the configuration formed by selecting pipe i, and removing the pipe if it is on, or adding the pipe if it is off.

Let C be the configuration at iteration n and G_C be its neighborhood, $G_C = \bigcup_{i=1}^{M} C^i$. When we anneal the system, we randomly select a configuration C^i from G_C at each iteration n, and compare the two energy functions Q(C) and Q(C^i).

The energy functions we use are a measure of the difference between the observed and the simulated system response. We consider energy functions of the form:

$$Q = \sum_j (o_j - s_j)^2 \qquad (7.1)$$

where

o_j = a vector of observed responses, and

s_j = a vector of simulated responses.

The observed measurements could be hydrologic, geological, or geophysical. For example, we can use

$$Q = \sum_t \sum_j (h_{oj}(t) - h_{sj}(t))^2$$

where $h_{oj}(t)$ is the observed steady state head response at well j and time t, and $h_{sj}(t)$ is the simulated steady state head response at well j and time t.

The energy function, scaled by the temperature, is used to decide whether the system should make a transition to a new configuration. The temperature is lowered as the algorithm progresses, to make it increasingly unlikely that a transition to a higher energy state will occur.

If we let the algorithm run at a fixed temperature, we are sampling configurations using a Gibb's distribution, a generalization of the Boltzmann distribution:

$$P(C) = \frac{1}{k} e^{-\left[\frac{Q(C)}{T}\right]}.$$

The likelihood of occupying a configuration at any iteration is related to the energy of the configuration.

The normalizing constant, k, which assures that the sum of the probabilities of all possible configurations is unity. We assume that this constant exists, but it is very difficult to evaluate because we must know the energy for every possible configuration to compute k. So, we can not compute the absolute probability of any given configuration because we do not know k. However, we can compute the relative probability of any given configurations. For instance, we could say that a configuration would be twice as probable as another.

Further, we know that if the probability function is a Gibbs distribution then this is equivalent to modeling C, the current configuration as a Markov Random Field. A Markov Random Field of order 1 exists if the probability defined meets two conditions. The first condition is that the probability of selecting any configuration in the system is greater than zero. The second is that the probability of making a transition from C to any other configuration C' given we are at C,

depends on C, C' and whether C' is in the neighborhood of C. Past history, such as the configuration we selected before C, does not tell us anything about the probability of moving from C to C'. So, the probability of moving from one configuration to another can change with the iteration, but does not depend on which configurations have been examined in the past. This means we can examine a series of configurations without remembering how we moved from one to the next and we can still compute the relative probability of each configuration.

At each iteration k, given C, G_C, the neighborhood, and T, the temperature, we can find a matrix of transition probabilities. The probability we will move from configuration C to C', given our current configuration C is equal to the probability that we select C' to compare with C, multiplied by the probability that the system would make the transition to a given C'. That is:

$$P\{C \rightarrow C' \mid C\} = \begin{cases} 0 & \text{if } C' \notin G_C \\[2ex] P(C' \mid C) \cdot 1 & \begin{array}{l}\text{if } C' \in G_C, C' \neq C \\ Q(C') - Q(C) \leq 0\end{array} \\[3ex] P(C' \mid C) \cdot e^{-\left[\frac{Q(C') - Q(C)}{T}\right]} & \begin{array}{l}\text{if } C' \in G_C \ C' \neq C \\ Q(C') - Q(C) > 0\end{array} \end{cases} \quad (7.2)$$

and the probability of not accepting the change to C' is:

$$P(C \nrightarrow C' \mid C) = P(C \rightarrow C)$$

$$= 1 - \sum_{\{C' : Q(C') \leq Q(C)\}} P(C' \mid C) - \sum_{\{C' : Q(C') > Q(C)\}} P(C' \mid C) \cdot e^{-\left[\frac{Q(C') - Q(C)}{T}\right]}$$

$$(7.3)$$

It remains to discuss the temperature schedule. The schedule is used to lower the temperature as annealing progresses. Physically, this means that as annealing progresses we are less and less likely to keep changes which increase the energy of the system. At this time, there is a theory which relates the temperature schedule to the convergence properties of annealing. This theory (Hajek, 1988) shows that a temperature schedule which is inversely proportional to the log of the iteration number will converge in probability to a set of minimum energy states.

Unfortunately, the theoretical results for convergence to this set of minimum energy states depend on sampling a large number of configurations. While this is necessary for convergence, it is not necessary to find one or several low energy solutions. We are searching for several good solutions, which give a response within the measurement error of the observed response. Hajek's temperature schedule is over constraining for our purpose.

The temperature schedule we use here, following the suggestion of Press, et al. (1979), is only justified heuristically: it does find low energy solutions. We decrease the temperature whenever 50 changes have been accepted at the current temperature. Each interval of the schedule with constant temperature is called a step. At the end of each iteration, k, the temperature, T_k, is decreased using a geometric series,

$$T_{k+1} = T_k \, t^k \tag{7.4}$$

where

$$0 < t < 1.$$

The initial temperature is chosen such that it is of the same order of magnitude as the energy difference between the first two configurations. This is done in an attempt to scale the energy difference between successive configurations between zero and one. Other choices of temperature schedule are possible which are currently a topic of research.

7.2. A Synthetic Example

In order to see how the simulated annealing algorithm works, we have developed a series of synthetic "real" cases. In these cases, the "real" system is completely known so that the results of annealing can be evaluated absolutely to the steady state data.

A synthetic case was generated using the fracture network generator FMG, (Long, et al., 1982, Long, 1983). FMG produces random realizations of a population of one-dimensional fractures in a two-dimensional square region called the generation region. A dimensionless network with two fracture sets was generated on a 100×100 grid (Figure 7.1).

On this network, we model an interference test by creating a constant flux internal boundary at a centrally located well. The program TRINET (Karasaki, 1989) is then used to calculate the
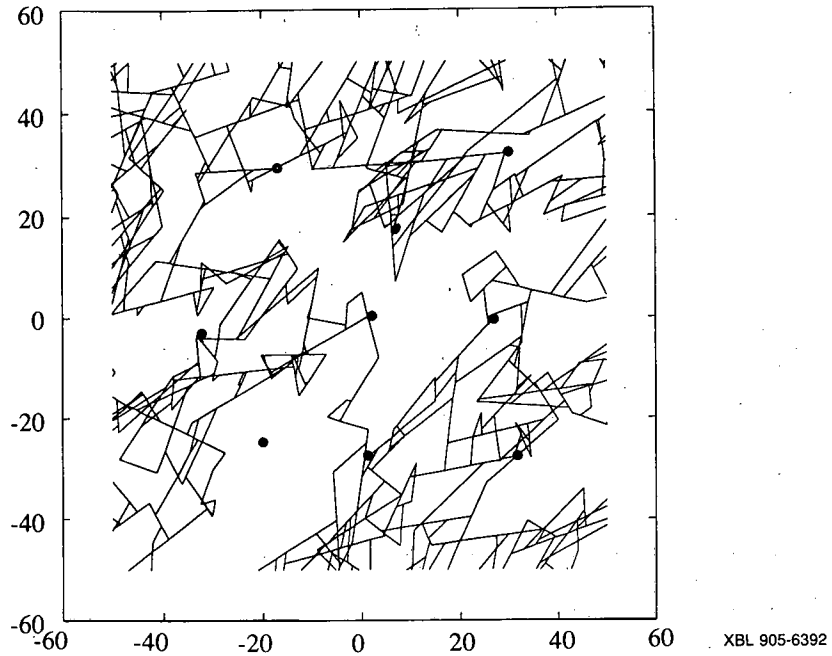
Figure 7.1. The synthetic case used to generate well test data for use in annealing. Dots represent points where "well" data were generated, the central being the pumping well. Scale can be considered dimensionless.
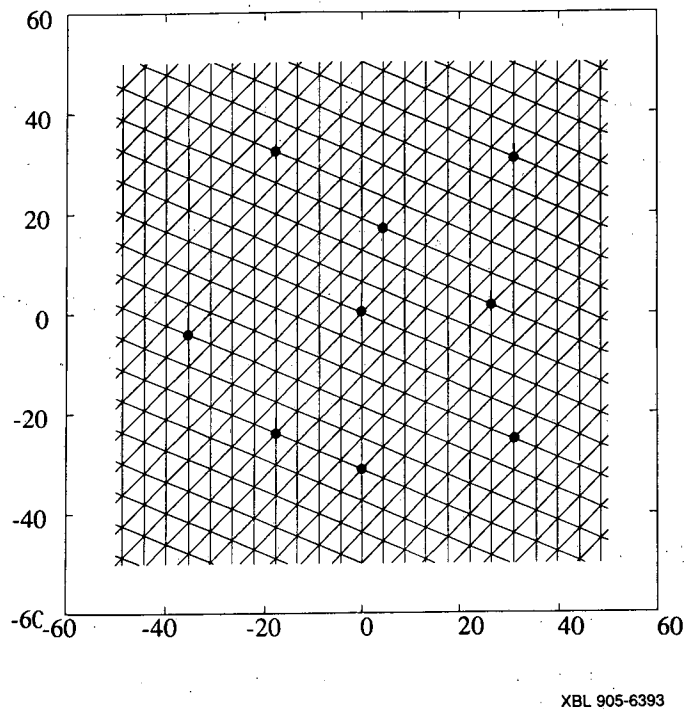
Figure 7.2. An example template developed for annealing the synthetic well test data.

head response at a series of observations wells. These heads become the "real" data that we try to match with annealing.

A template for annealing was developed using a grid with orientations close to those of the two fracture sets in the synthetic case. Figure 7.2 shows the template. The annealing algorithm found a minimum energy solution which appears by eye to match the flow geometry well. Figure 7.3 shows the minimum energy solution and Figure 7.4 shows the energy versus the iteration number for the annealing run.

Many of these synthetic cases have been generated in order to learn how annealing works best. We have studied the effect of the starting configuration by varying the percent of conducting elements in the initial configuration. Results have shown that the final configurations converge to about the same percentage of conducting elements. Further, we have tried various formats for the template. It is not surprising that building a template with conducting elements oriented similarly to the real system appears to give better results. These studies are ongoing and can also be used to indicate which schemes for choosing configurations to test are best.

7.3. Application of Annealing to the MI Site

Annealing has now been applied at several fractured sites with encouraging results. Here we will briefly summarize one such application at the MI site in the Grimsel Mine (Davey et al., 1990). Annealing was applied to cross-hole tests which were conducted in the plane of a fracture (or fracture zone) called the MI. So far this is the best application available because of the good quality of the cross-hole data. Annealing was also applied to the Stripa cases described in Section 6 and is described in Long et al. (1990), but the available hydraulic tests were poorly controlled.

The MI is a fracture zone (shown as shaded planes in Figure 7.5 which intersects a drift. From the drift, eleven boreholes have been drilled into the plane of the fracture zone. Water flows from the zone into the drift which is not sealed. The zone is an S-zone as described in Section 2. This means that the geologic investigations indicated that vertical permeability should be the most significant.

XBL 905-6394
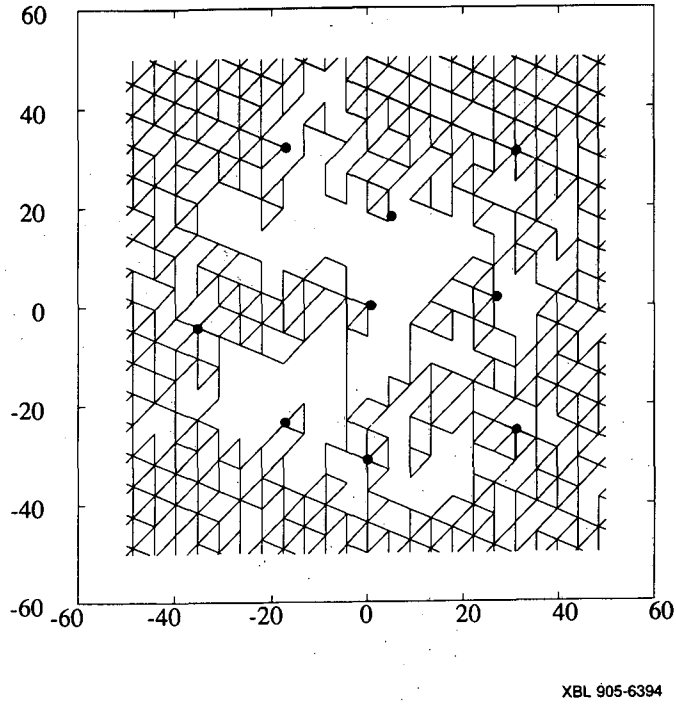
Figure 7.3. A configuration resulting from annealing the synthetic well test data.

XBL 8910-3871
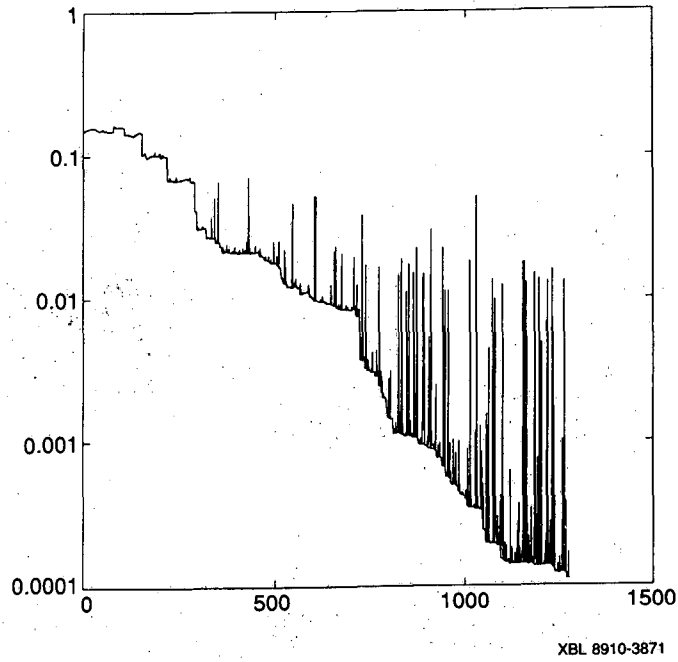
Figure 7.4. The dimensionless energy versus iteration curve for the synthetic annealing case.
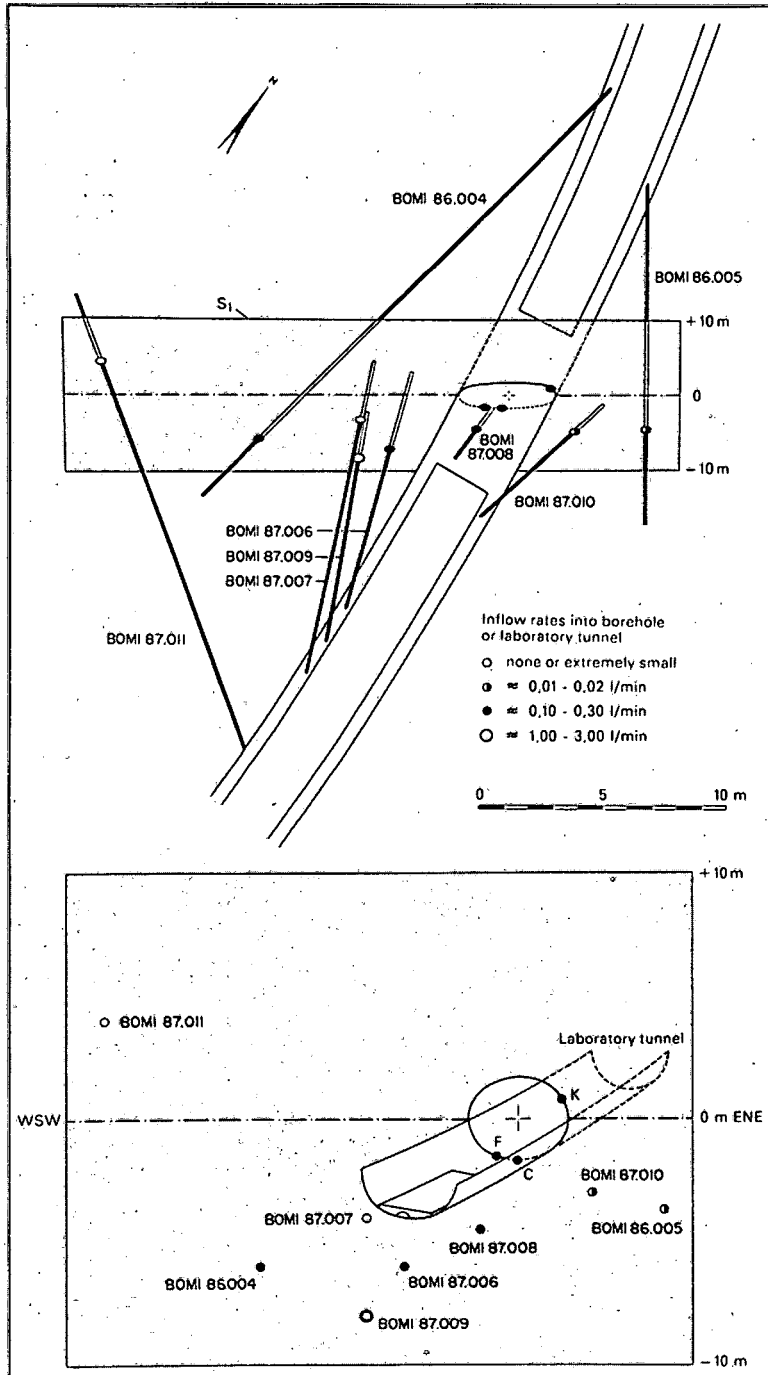
XBB 896-5038

Figure 7.5. The lay out of the MI experiment showing the plane of fracture zone which intersects the laboratory tunnel and the eleven wells drilled from the drift which intersect the zone.

At the MI site, several constant pressure tests and a constant injection test were conducted in the Migration fracture while the pressure was measured at a number of observation points. The intervals in the boreholes that intersect the fracture are isolated with double or triple packers. The packed-off intervals are numerous and closely located.

A group of tests conducted from late December 1988, through mid-February 1989, consisted of a constant flow withdrawal test followed by a buildup test (Figure 7.6). The flow period was maintained for more than 35 days long and the buildup was monitored for about 20 days. Two different cases were studied. The first was a steady flow example, and the second was a transient flow example. In the steady case, head measurements at the various wells were measured in response to drawdown to the drift running through the fracture. The heads at the end of the recovery period were used for the steady state case. The drawdown data was used in the transient case. Unfortunately, the flow rate fluctuated in the first few minutes of pumping because a stable flow rate could not be maintained at the initial flow rate of 150 ml/min. Consequently the rate was changed to 340 ml/min at 4 minutes into the test.

Figure 7.7 shows the template that was developed for this site and Figure 7.8a-e shows five of the configurations that resulted from annealing this data. A dense mesh is used in the vicinity of the wells where we expect annealing to be able to resolve the pattern of conductance. A coarser mesh is used outside of this region in order allow the numerical simulation to be insulated from the boundaries. The template includes vertical conductors in accordance with the geologic investigations.

In Figure 7.8, one can see regions between wells 7, 11 and between wells 4, 6, and 9 where annealing is predicting lack of connection. Also, annealing has found lack of connection between well 11 and the boundary. This is happening because well 11 had a very low head, close to zero. As the drift boundary is zero head and the boundaries are held at a head of 100 m, steady state annealing encourages a connection to the drift. In transient annealing, we may be able to identify lack of connection to anything given sufficient different cross-hole data. This data would have to sequentially use different holes as different sources.

MI

ALL BOREHOLES
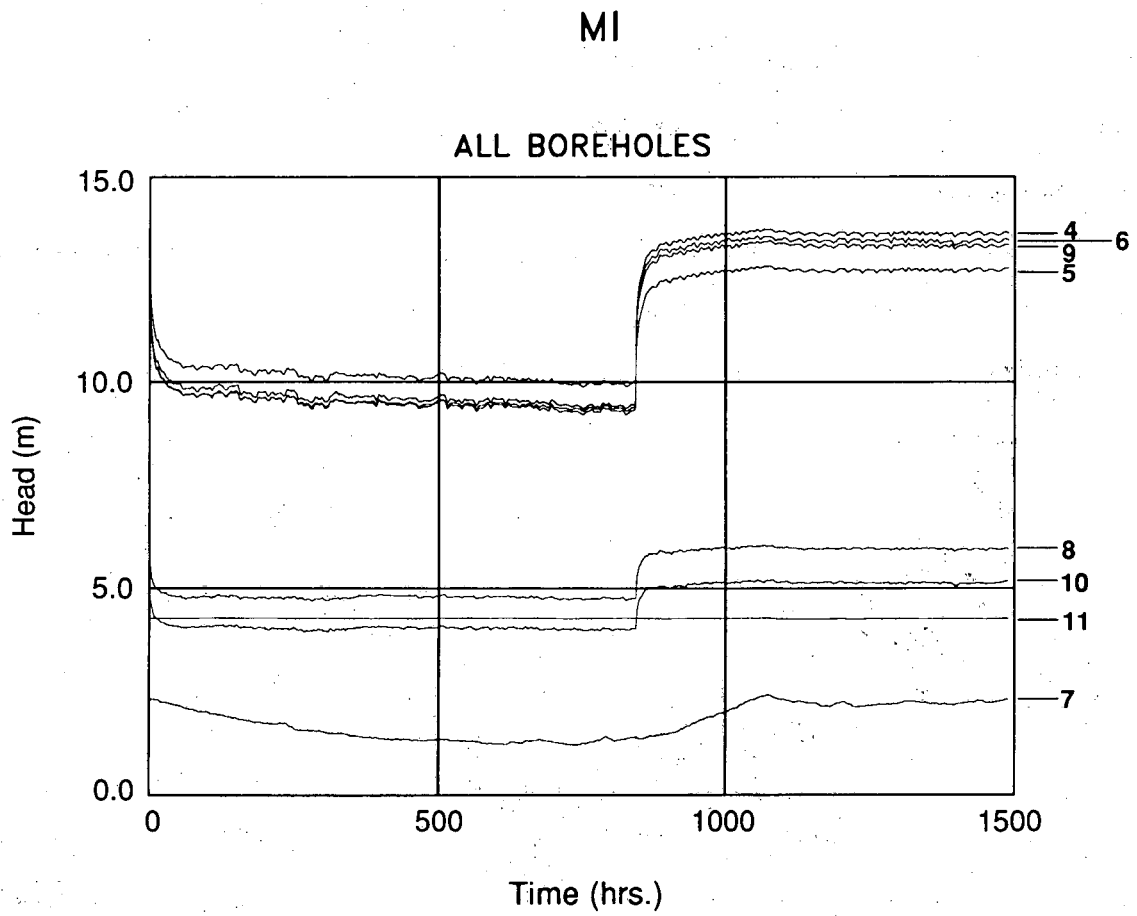
Figure 7.6. Head records in the eleven wells during pumping of well 9 and subsequent recovery.

The MI Template
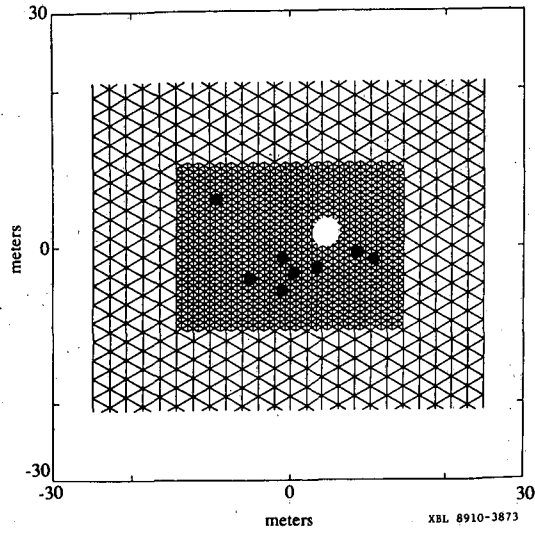
Figure 7.7. The MI template.
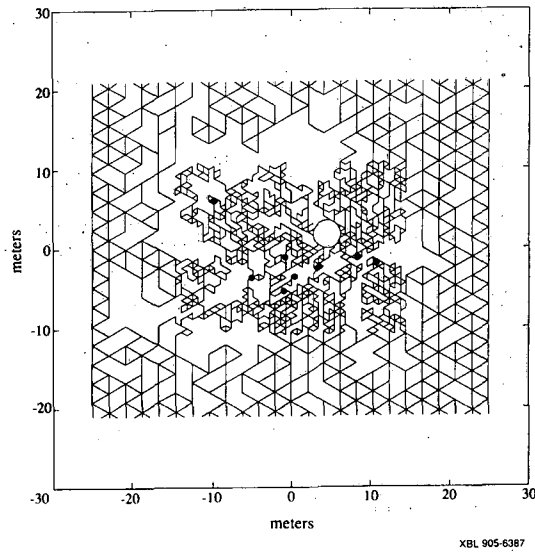
Figure 7.8a. The first of five solutions which have similar geometries, case 1.
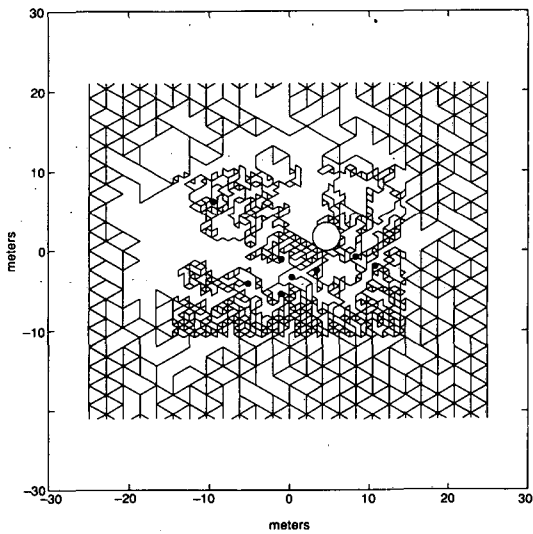
Figure 7.8b.   The second of five solutions which have similar geometries, case 2.
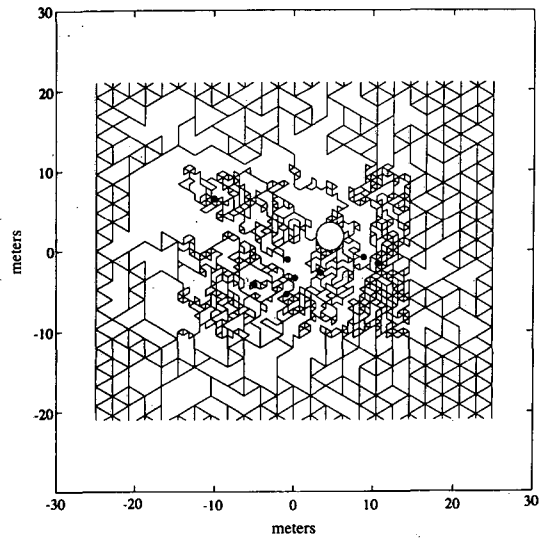
Figure 7.8c.   The third of five solutions which have similar geometries, case 3.
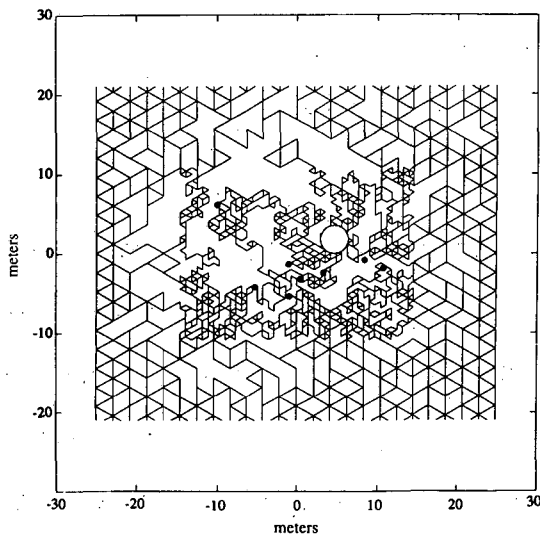
Figure 7.8d.   The fourth of five solutions which have similar geometries, case 4.
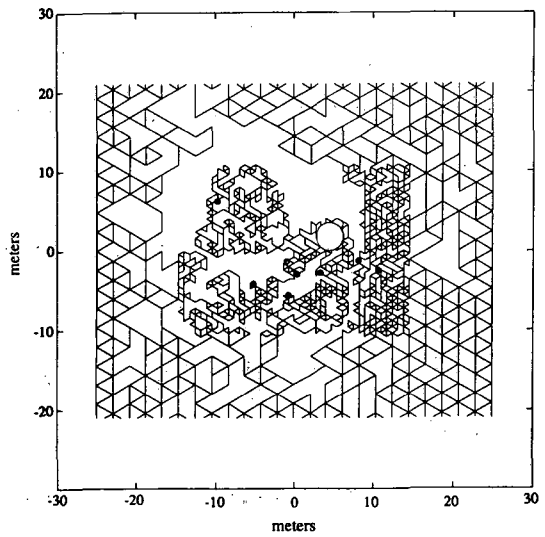
Figure 7.8e.   The fifth of five solutions which have similar geometries, case 5.

The transient data was based on a pumping test from well 9. Annealing this data required that we construct an energy function which is the sum of differences in predicted and measured heads for a series of times and locations. Using transient data creates some difficulties and practical aspects that need to be addressed. These mainly concern problems in forward modeling of field hydraulic tests. For instance, when there are multiple measurement points, all the recorded data do not always have a common "good" portion. One of the gages may drift or pick up noise, or the pump may work erratically at times. The "bad" portion of the data induced by these causes should not be matched against the forward modeling result. The "goodness" of data should be determined by a hydrologist who is well-informed with the details of the field operation.

Also, different types of data carry different weights. In other words, "good" data may not always be crucial in the model. Conversely "bad" data may still contain important information. For example, an estimate of the inflow rate that is 50% off can often be more useful than a very accurate measurement of the pressure observed at a non-strategic observation point. Again, the discretion of a hydrologist is necessary. Furthermore, in some cases no field measurements exist that are essential input for the forward modeling. One such example is often the boundary conditions. A hydrologist may literally have to make up boundary conditions using expert reasoning. In summary the use of annealing is an iterative process that requires close integration of expertise with technique.

In the case of MI, the initial flow rate was very unstable and the flow rate was increased after a few minutes into the test. To forward-model this, we assumed the flow rate to be constant and adjusted the time duration such that the cumulative flow was the same. The pressure data observed at various intervals were also "noisy" in the early time. We did not use this portion of the data for energy calculation. To calculate the energy with equal weights in log time scale, and to smooth the data we used a window averaging scheme. One of the intervals had a pressure reading that virtually did not respond to the pumping. We assumed the pressure change to be absolute zero in this case. Also, data from different intervals had different "good" portions. Energy was

calculated for the time duration that corresponds to the "good" portion of each well test curve.

As for the boundary conditions, we assumed that the head at 100 m away from the laboratory tunnel to be constant. The head value was assumed to be 100 m. This was estimated from the measurements in the exploratory boreholes drilled prior to excavation of the laboratory tunnels. Through a sensitivity study it was found that the results are not very sensitive to the boundary conditions prescribed at over a certain distance.

Figure 7.9 shows the template that was chosen for the transient annealing case. Here, a larger region has been modeled in order to avoid problems with "seeing" the boundaries. The portions of the head records used for annealing are shown in Figure 7.10. Figure 7.11 shows the simulated well test data before annealing. Figure 7.12 shows the well test responses on the final annealed configuration at iteration number 15,510 shown in Figure 7.13.

Here we can see that the low head at well 11 has been taken care of by isolating this well from the rest of the network, a solution quite different from the steady state response. Another interesting feature of this network is that annealing was unable to match the response of well 7. Even though well 7 is physically close to the pumping well (9), it is hydraulically far away. Annealing is not able to find a tortuous enough path to account for this. This can be considered a problem of mesh refinement. However, it could also be that the real problem is quasi-three-dimensional and we have restricted this analysis to two-dimensions. Some of this difficulty might also be solved by allowing mesh elements to have different conductances.

7.4. Summary

The steady state results show that we can easily match the data and demonstrate the utility of multiple solutions to the inverse problem. The difference between the observed heads and those found numerically in each solution is very small. The annealing algorithm seems to 'smear' the nearby measured flow response over regions with no data available. However, unlike kriging, the nearby measurements are not linearly interpolated over these regions. The algorithm finds a random flow geometry which works; and this will vary in each solution.
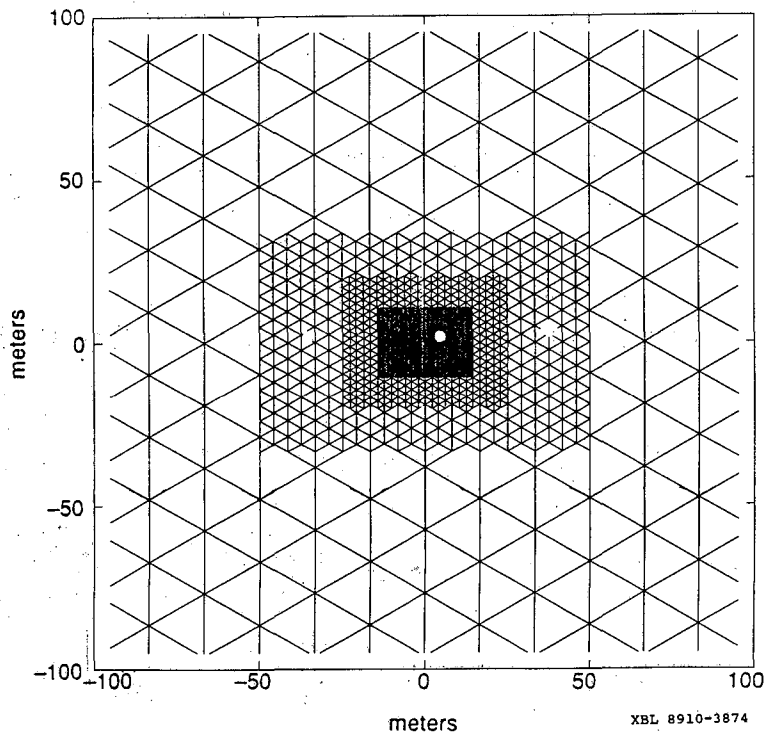
Figure 7.9. Template used for transient annealing of MI data.
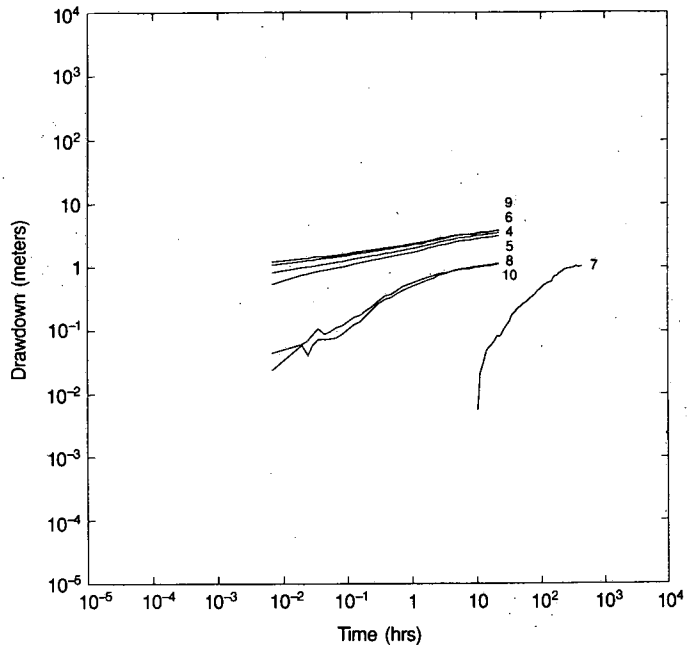
Figure 7.10.   The "good" portion of well test curves used to model the system.
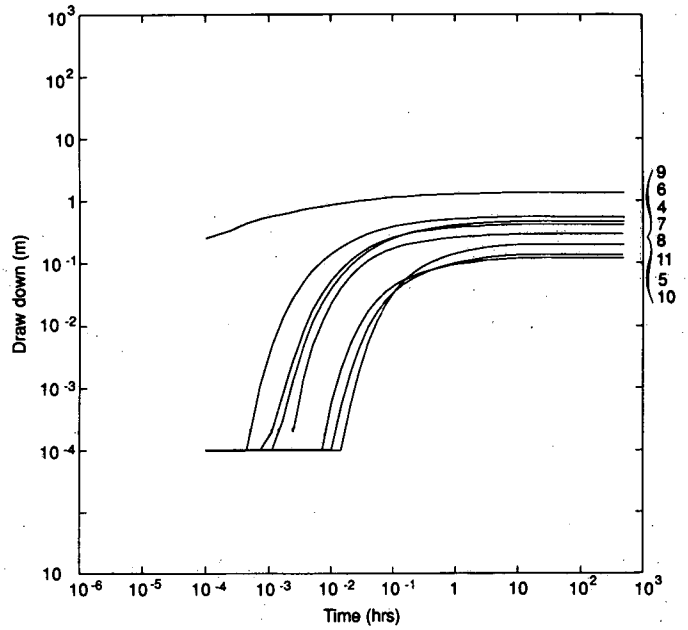
Figure 7.11.   Simulated well test response on the full template before annealing.
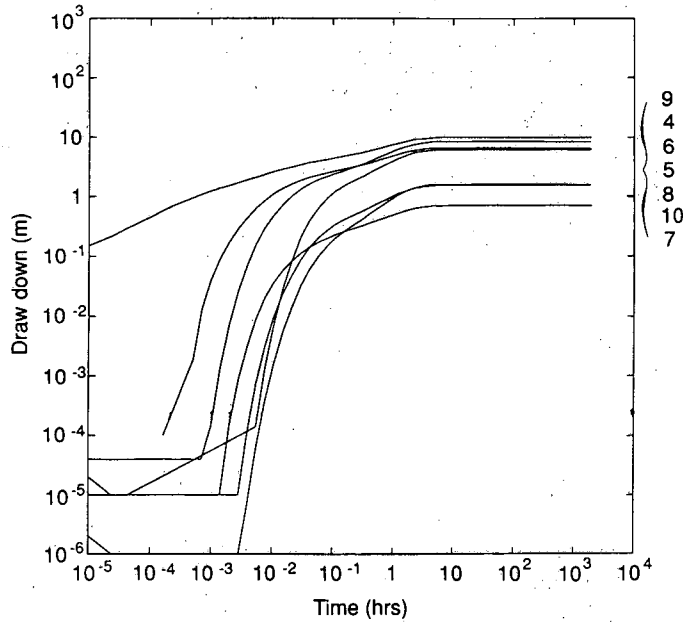
Figure 7.12. Simulated well test response on the annealed configuration.
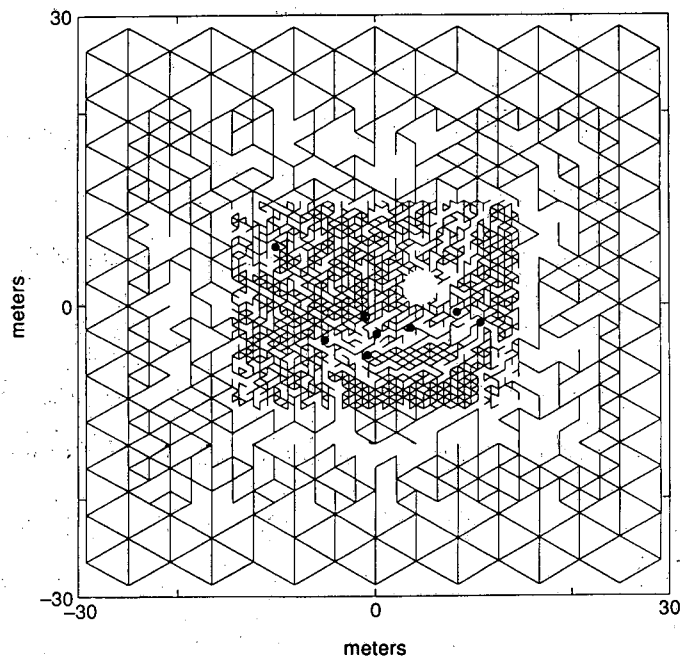
XBL 8910-3876

Figure 7.13. The annealed configuration at iteration number 15510.

The steady state and transient solutions are different. As mentioned before, the lack of continuity in some regions of the transient case flow geometry may indicate a low permeability zone. Similar regions in the steady state solution, such as the region between well 11 and the boundary, are harder to interpet. The large effect of the boundary conditions and the drift make one suspicious that this is a modelling artifact. However, both solutions clearly show a break between the region surrounding wells 7 and 11, and the region around wells 4, 6, and 9. The transient solution also shows that the region between well 9 and well 5 has low storativity relative to the rest of the modelled area.

The transient response of a system is more sensitive to the distribution of permeability than the steady state response. Theoretically, this makes transient annealing more attractive, but in the problems studied here we could not match the results from well 7, which is apparently in a low permeability zone. This is a significant result since it illustrates the limits of a model with uniform conductance for all channels. The model can not find a path long enough or tortuous enough to account for the delayed response at well 7. In the framework of this modelling technique, a long tortuous path or a short lower permeability path will have the same effect. However, a short low permeability path is easier to represent.

The problems we solve have many acceptable solutions with different flow geometries. If the same generalized geometry is found in a certain region for many solutions, we may believe that it is likely to be real. However, we must rely on expert opinion to tell us if the flow geometry is reasonable, or if it is an artifact of the process. An example of such an artifact may be the steady state solution around well 11 discussed above. However, it is important to keep in mind that we are fundamentally trying to build a model of hydrologic behavior, not fracture geometry. Therefore, the best way to assess the validity of the model is by estimating the error associated with using the model to make hydrologic predictions as discussed in Section 9.

8.0. APPROACHES WHICH INCORPORATE SCALING

Annealing is not the only possibility for finding networks of fractures which honor the hydrologic data. Another approach which holds promise is related to the fact that fracture networks may exhibit scaling behavior. We can find objects that exhibit self-similar properties which also behave like the well tests we observe. This approach has tremendous appeal for the simple reason that the self-similar properties provide a logical path for scaling up our understanding to larger regions.

Probably the simplest approach is to look for fractals which have the hydrologic behavior we require. Some work on this topic has begun and is discussed below. Fractals, however, are really a subset of a larger class of objects that can be generated with "iterated function systems", or IFS. Some new ideas for inverse techniques based on IFS are also briefly described.

8.1. Fractal Approach

It is not hard to believe that some fracture networks might form a type of fractal. In fact, the name "fractal" is derived from "fracture." We can consider that fluid flow in a fracture network is equivalent to the problem of percolation on a lattice Hestir and Long (1990). Then the network is characterized by clusters of conductors which form at scales which exhibit self-similar geometry (Orbach, 1986). Thus, the structure of such networks can be characterized by a fractal dimension (Mandlebrot, 1982).

Barker (1988) has provided a technique for determining the fractional flow dimension of a network through a well test. He solved the generalized equation of flow to a well by letting the flow dimension be a variable (Figure 8.1). Thereby, the flow dimension is allowed to be fractional, say, a dimension of 1.6 or 1.8 (as opposed to integral dimension, i.e.; two or three-dimension space).
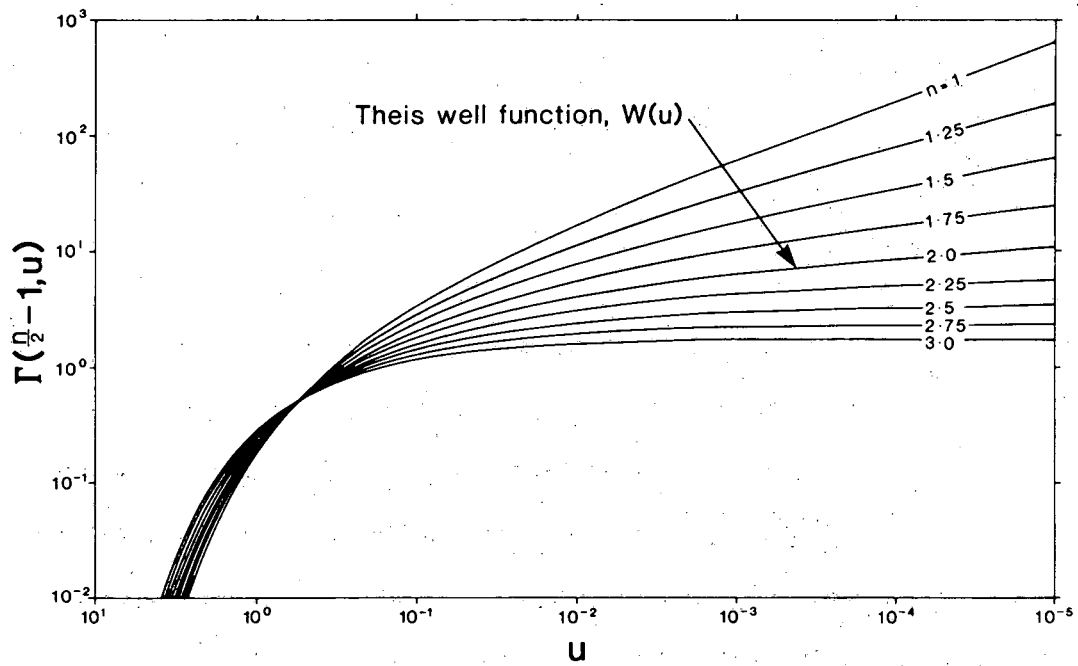
Figure 8.1. Drawdown curves for systems of partial dimension (after Barker, 1988).

The notion of this fractional dimension flow can be easily understood by a simple illustration. Let us consider two points in a space connected by lines representing fractures (Figure 8.2). Figure 8.2a shows a simple one-dimensional connection between A and B. Figure 8.2b shows a two-dimensional connection between the two points. This is the case when fractures are dense and well connected. However, in reality, fractures are generally irregular and disconnected. Therefore, Figure 8.2c is more likely a better representation of the connection between two points. The flow dimension between these two points must lie between one and two. The case can be considered an extension of the discrete composite media cases studied by Karasaki (1986) to a gradually changing media.

The concept of fractional dimension flow can be summarized by saying that the area available to flow, $A(r)$ is not necessarily proportional to a integral power of the Euclidian distance r from the well. In one-dimension, the area available to flow is constant; $A(r) \propto r^0$, in two-dimension; $A(r) \propto r^1$, and in three-dimension; $A(r) \propto r^2$. However, the geometry of the fracture network may be such that $A(r) \propto r^{1.7}$, for example. We believe that the geometry in the fractional dimension flow theory proposed by Barker is a subset of the fractal geometry.

In order to investigate well test behavior in a fractal network, we have generated a simple fracture mesh that has a fractal geometry (Figure 8.3). Note the self-similarity of the pattern at different scales. At each scale, five out of nine blocks have fractures of similar pattern. Because each block is divided into 1/3 and five blocks are chosen at each level, the fractal dimension of the mesh is $\ln 5/\ln 3 = 1.465$. These five blocks can be chosen symmetrically, but in Figure 8.3a they are chosen randomly. The finite element flow simulator, TRINET, was used to simulate well tests in these mesh.

Figures 8.2b and 8.3b show the pressure vs. time curves at the pumped well as well as at several locations in the corresponding mesh. In a regular orthogonal lattice, the curves will be identical to those in an isotropic porous medium. However, as can be seen in the figures, this is not the case. There is a straight line portion in the curves. The slope of the straight line is consistent for both the symmetric and the random case. For the random case, all of the several dif-
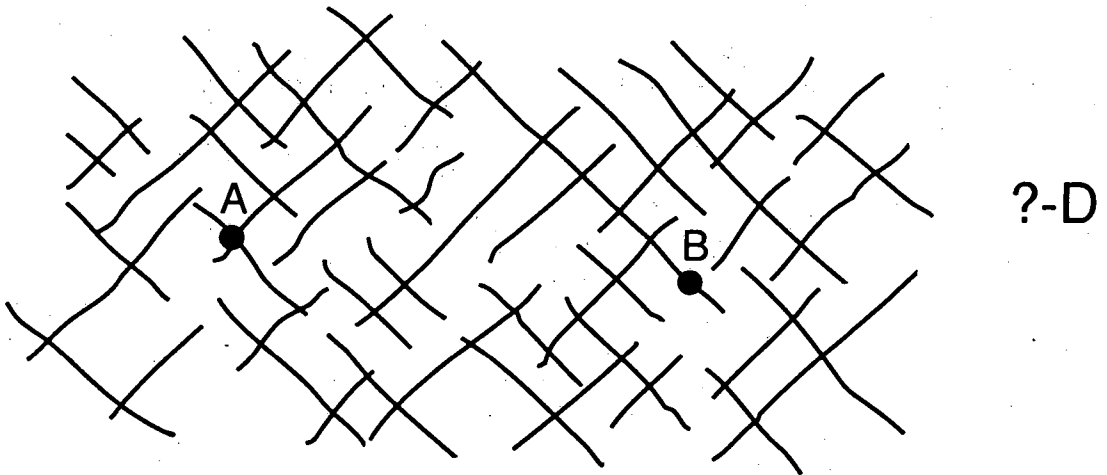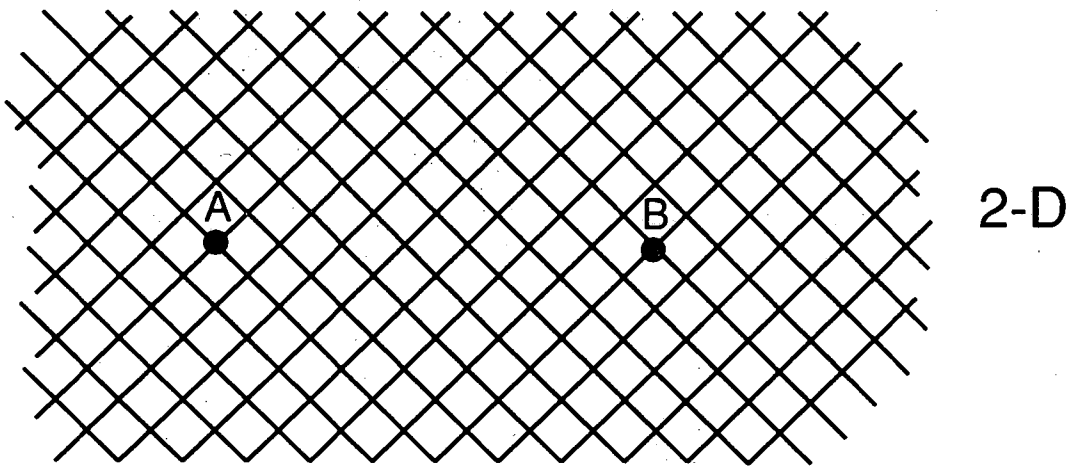
Figure 8.2. Physical systems where flow between wells A and B would be one-dimensional, two-dimensional, and of partial dimension respectively.
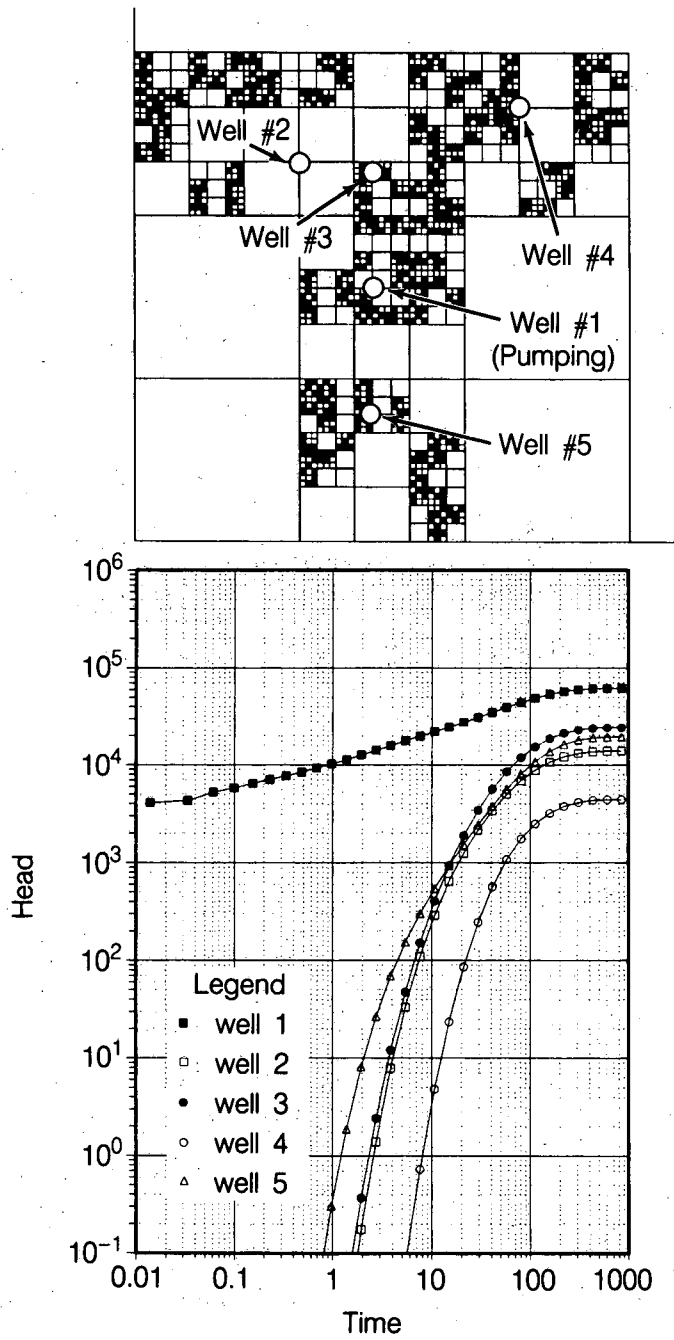
XBL908-6762

Figure 8.3. A random fractal mesh and the response curves for a well test on this mesh.

ferent realizations produced consistent slopes. Next, by choosing 3, 4, and 6 blocks instead of 5, different meshes with different fractal dimension were constructed. Again, several realizations were made for each case. It was found that the slope of the straight line portion of the curves is consistent among the realizations and was clearly a function of the fractal dimension (Table 8.1). Therefore, the slopes are diagnostic of fractal geometry. This is consistent with Barker's theory except for a small difference in the actual number for the slopes predicted by his theory.

Certain fracture systems may have fractal geometry (Barton et al. 1987). Therefore, use of fractal geometry for representing fracture system may be quite plausible. Flow to wells in such geometry differs from that in Euclidian geometry. One should be able to calculate the corresponding fractal dimension from the well test results if the straight line portion is present. This may be important information about the structure of the system. It is also impractical to represent all the fractures explicitly in a numerical model. Fractal representation of fracture geometry may provide another way to find equivalent discontinuous models.

Table 8.1. Slope of drawdown curves for networks
of different fractal dimension

Number of Fractured Squares	Fractal Dimension	Average Slope
3	$ln3/ln3 = 1.000$	0.411
4	$ln4/ln3 = 1.262$	0.363
5	$ln5/ln3 = 1.465$	0.323
6	$ln5/ln3 = 1.631$	0.246

8.2. The Use of IFS Models in Fracture Network Problems

An iterated function system (IFS) is a standard way to model self similar geometrical structures (Barnsley, 1988). To create an IFS one first specifies a function f, which maps sets to sets:

$$f(A_0) = A_1 \qquad (8.1)$$

where A_0 and A_1 are (compact) subsets of two (or three) dimensional space. A set A_∞ can then be

defined by

$$A_{n+1} = f(A_n) \quad n = 0, 1, \dots \qquad (8.2)$$
$$A_\infty = \lim_{n \to \infty} A_n \ .$$

Given certain restrictions on the set function f, one can show (Barnsley 1988) that A_∞ exists, is independent of the starting set A_0, and generally has a fractional Hausdorff dimension (eg., A_∞ is a fractal). Hence f determines a fractal, A_∞.

If we have a function f that is easily parameterized then the fractal A_∞ is parameterized as well. This leads to a nice setup for modeling real world problems because a small number of parameters can characterize a complex geometry. One important example of a parameterized f used extensively by Barnsley (1988) is:

$$f(A) = g_1(A) \cup g_2(A) \cup \dots g_k(A) \ . \qquad (8.3)$$

Here the g_i's are so called affine transforms:

$$g_i(A) = \bigcup_{\vec{x} \in A} g_i(\vec{x}) \qquad (8.4)$$
$$g_i(\vec{x}) = B_i \vec{x} + \vec{b_i}$$

where B_i is a matrix and $\vec{b_i}$ a vector. The parameters characterizing f are the entries in the B_i's and $\vec{b_i}$'s. An example pattern generated using k = 3 affine transformations which results in a fractal called a Serpinski's gasket shown in Figure 8.4. Another example pattern generated using k = 4 affine transforms with entries chosen randomly appears in Figure 8.5. In this figure, the beginning set was one horizontal line segment and the pattern shown resulted from 6 iterations of f.

One can exploit the IFS idea to generate sequences of fracture patterns that have self similar properties and the complex geometries observed in the field. We have developed a way to do this with an iterative first order growth scheme. To build a fracture pattern with this scheme we can define a beginning set A_0, to be a given existing set of fractures in a mostly unfractured rock. The function f applied to a set A of fractures is defined to be a rule that grows new fractures from each of the existing fractures in A. This is done by looking at each fracture in A in its own local coordinate system (Figure 8.6a, the solid line) and growing one fracture from it using rules defined in
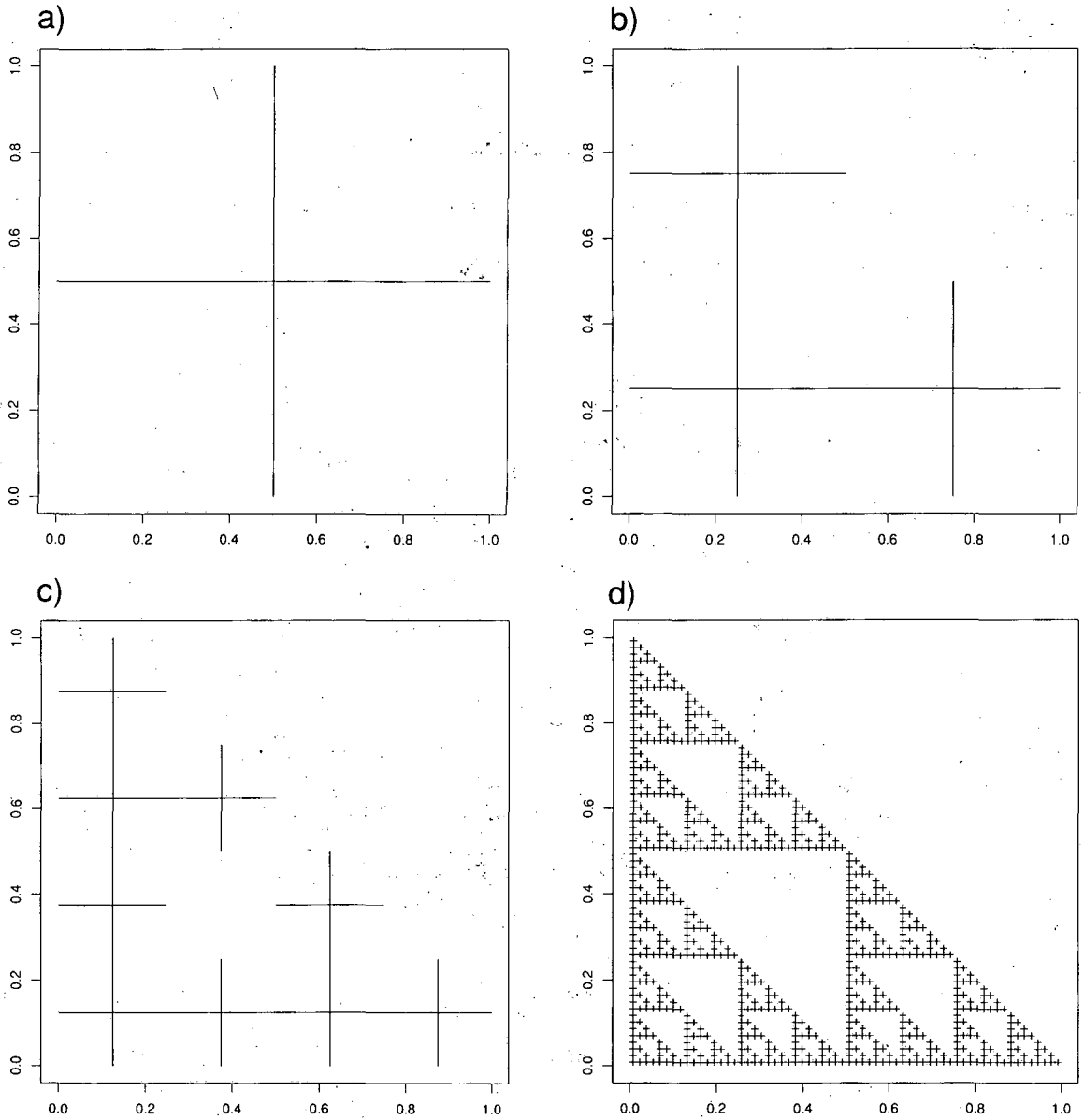
Figure 8.4. Generation of a Serpinski's gasket using the affine transformations given in the inset, lower right figure.
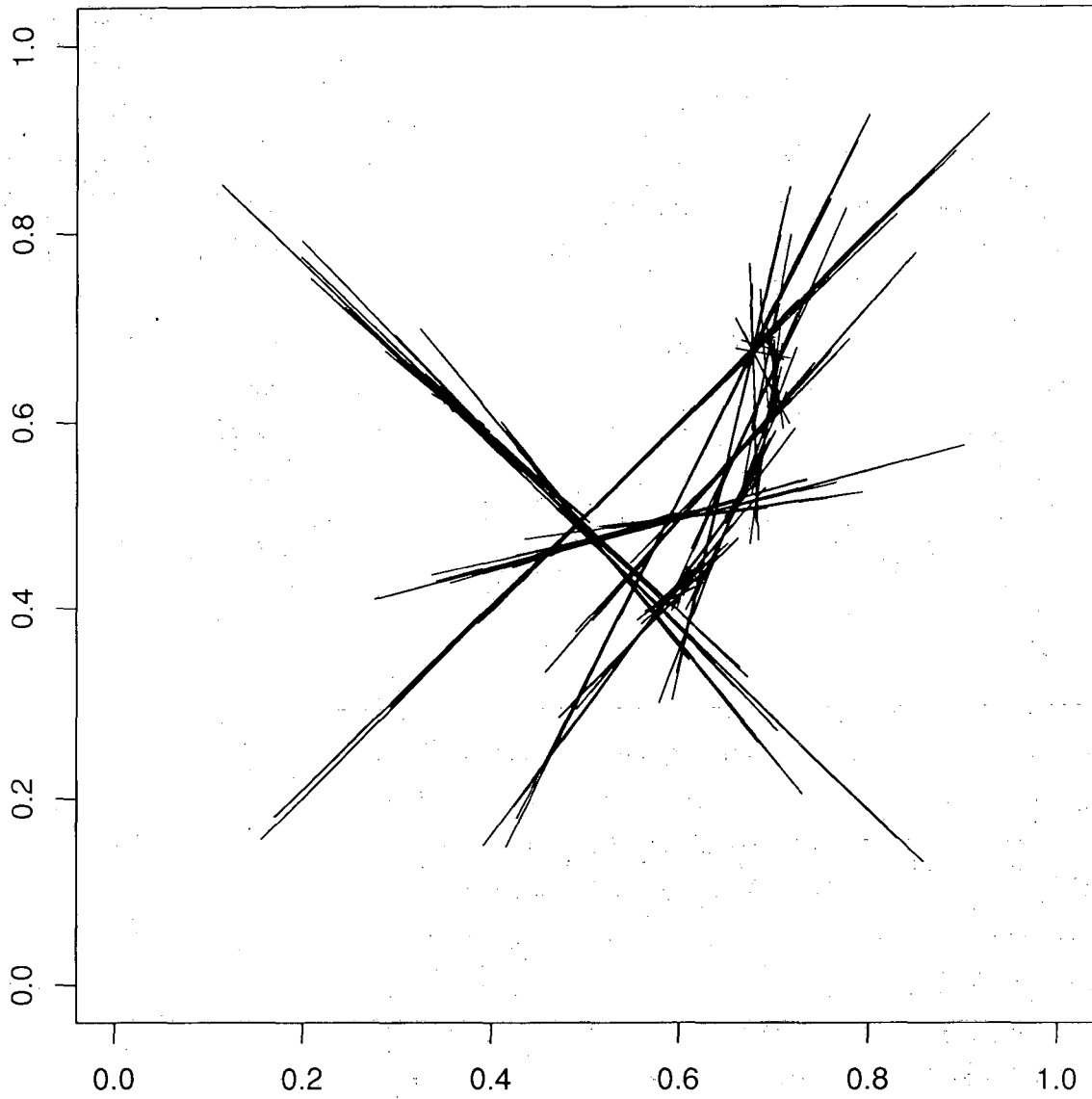
XBL 911-5208

Figure 8.5. A pattern generated using an IFS defined by 4 affine transforms with 6 iterations and a beginning set which is one horizontal line.

XBL 911-5206

(a)　　　　　　　　　　　　　　(b)
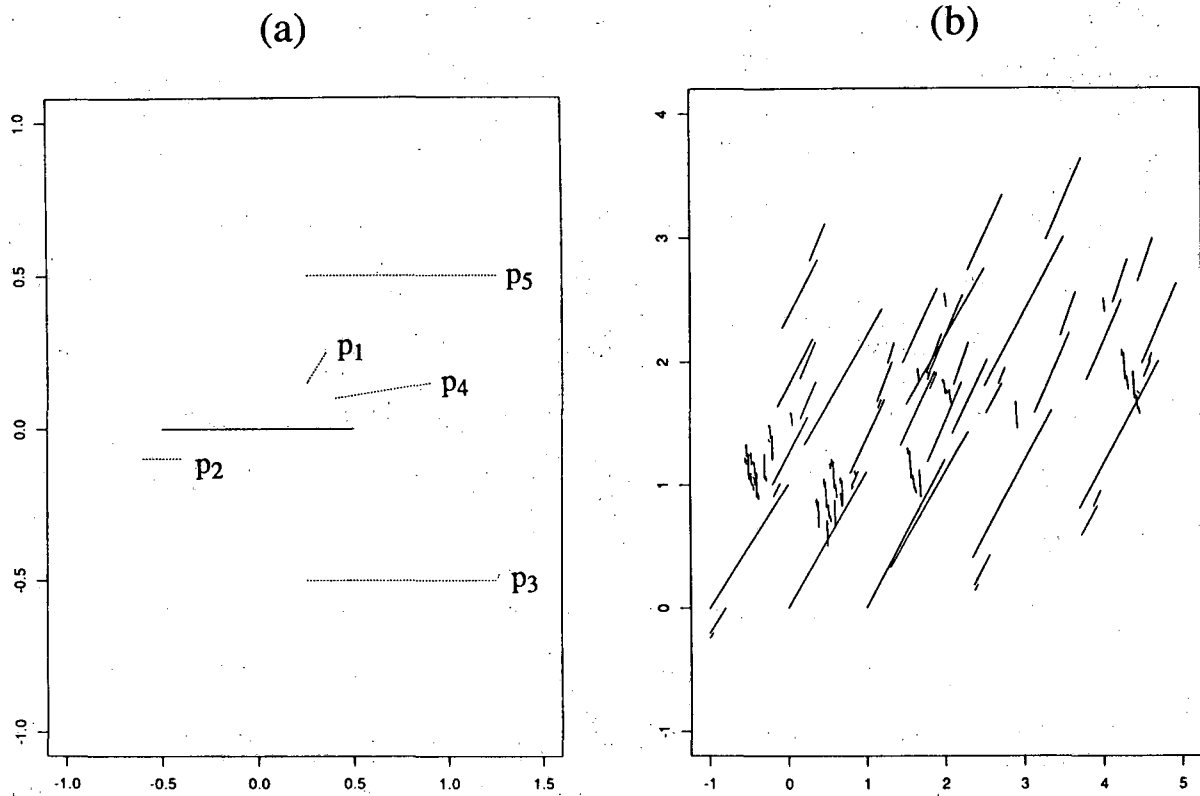
Figure 8.6. (a) A fracture (solid line) shown in its own coordinate system has the possibility of growing according to the dashed lines at each iteration. (b) Application of this growth scheme results in this fracture pattern.

that local coordinate system. The method is called first order because we grow new fractures without accounting for interaction between existing fractures. The new fracture growth is chosen at random from a finite number of possibilities, (the dashed lines in Figure 8.6a) each with a given probability of occurring. The growth possibilities (with probability $p_1 p_2$ . . .) shown in Figure 8.6a result in a fracture pattern given in Figure 8.6b. The rules governing fracture growth can be based on fracture mechanics. For example, the probabilities for growth are scaled to the size of the fracture, and the growth positions are approximately located where stress concentrations would be in the absence of interactions. So far, we have been able to use this method to produce realistic sequences of two dimensional fracture network patterns.

One can also use the geometries given by the IFS technique to define patterns of high and low permeability in a flow system. If there are hydrologic measurements on a system which can be numerically modeled, then inverse modeling techniques can be used to find an IFS for the system. This can be applied in porous media as well as fracture networks. In the fracture network case, this is an exciting idea because we have a hydrologic model which is coupled to a mechanically based model for fracture growth.

An example of the possibilities of using IFS for hydrologic inversion is given in Figures 8.7. Figure 8.7a shows a grid of points that are connected by equal conductance elements (not shown). A heterogeneous field is obtained by superimposing an attraction (Figure 8.7b) on the grid and increasing the conductance of those elements which are in the vicinity of points on the attractor. We then use a conjugate gradient technique to change the parameters of the attraction (Figure 8.7c,d) such that we find an attractor (Figure 8.7d) that matches the observed well test behavior (Figure 8.7e). Clearly this inversion could be refined to better match the early time data, but the example as is illustrates the possibilities for using IFS to characterize heterogeneous hydrology.
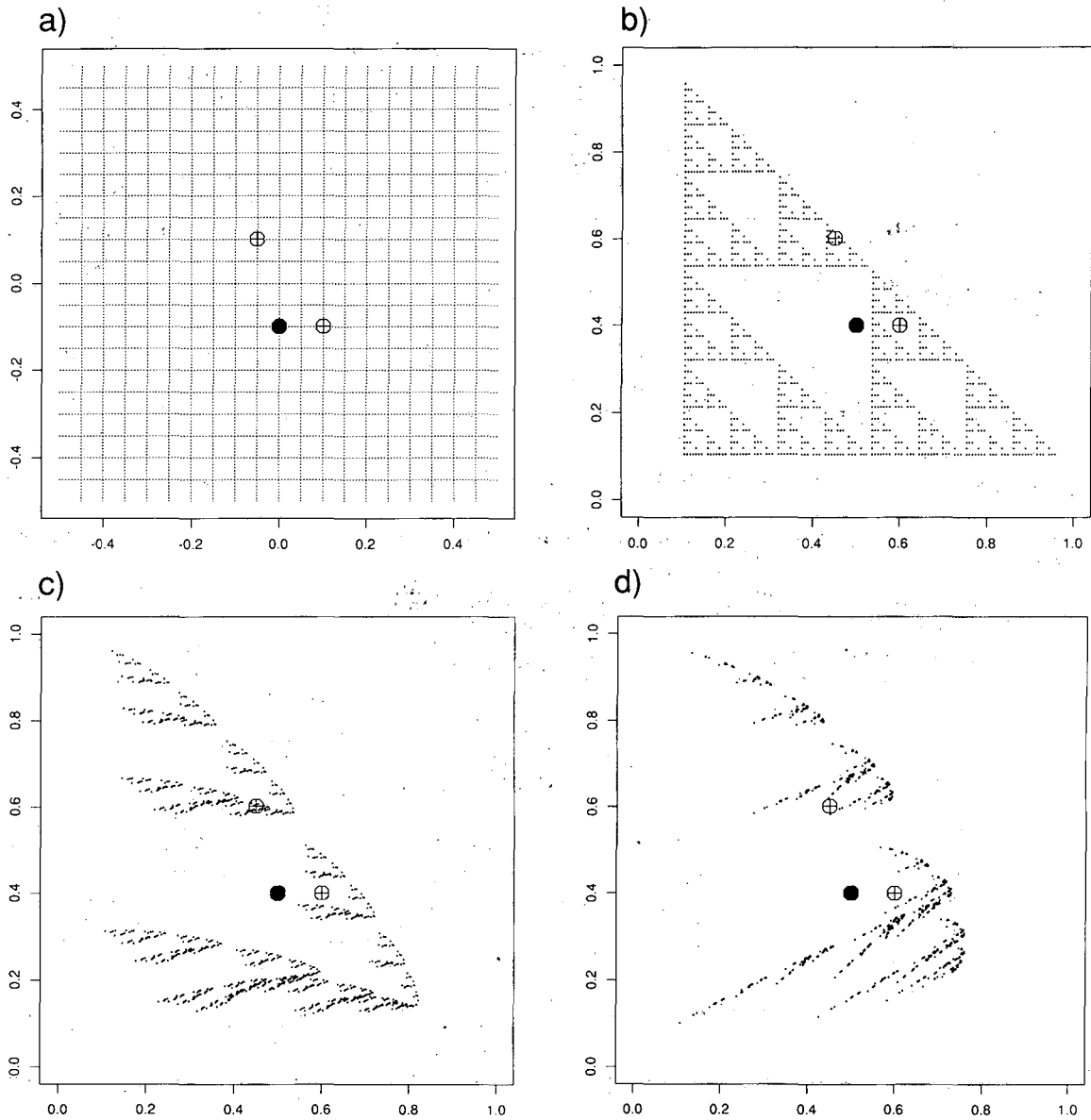
Figure 8.7. (a) A grid of equal conductance elements with 3 wells. The solid mark is the pumping well.
(b) The conductance of elements which are near points in this attractor is increased.
(c) An intermediate and (d) the final configuration of attractor.
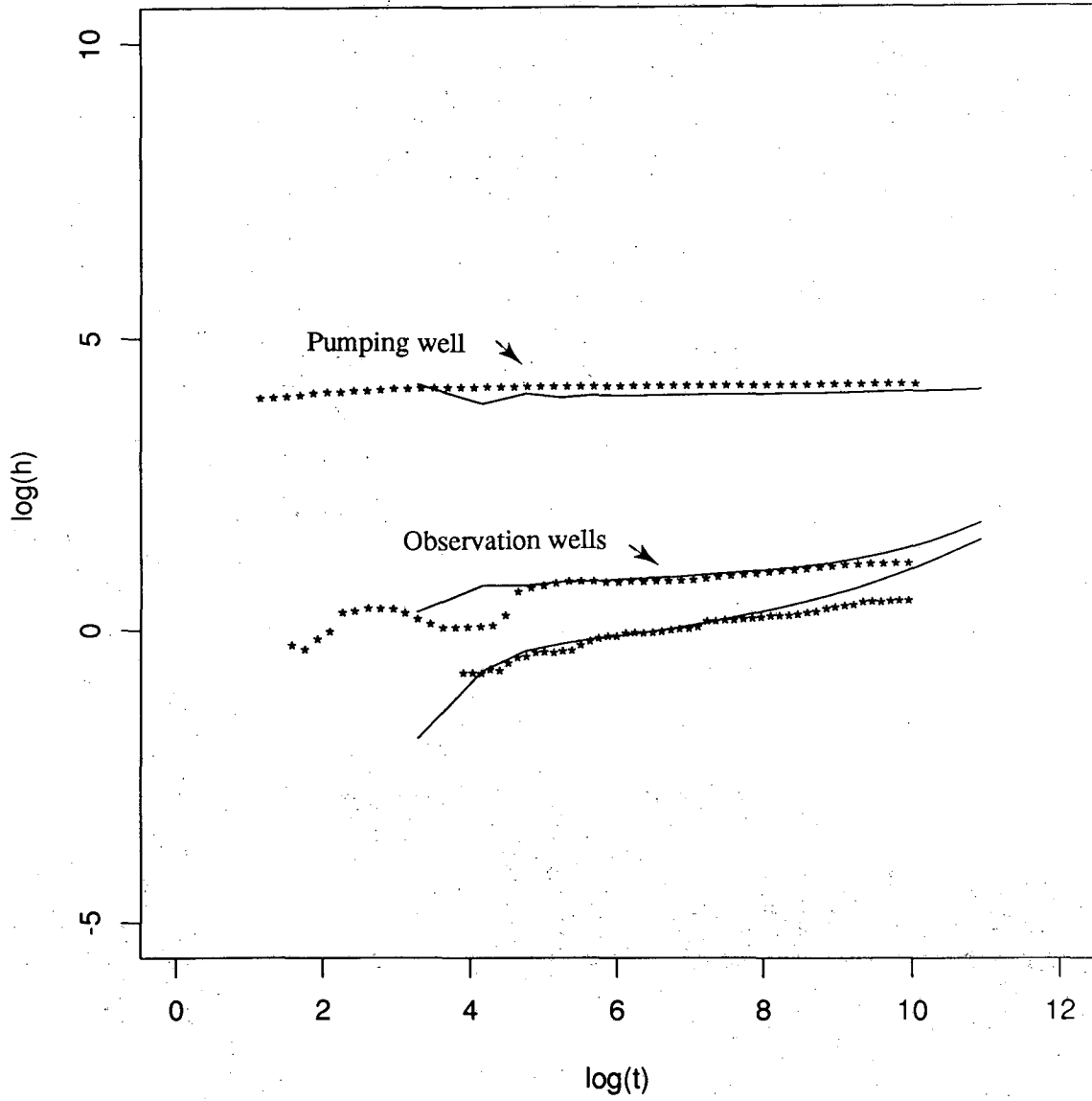
XBL 911-5209

XBL 911-5207

Figure 8.7. The final configuration matches the well test data as shown in (e). Stars are data, solid line is the simulation.

9.0. QUANTIFICATION OF UNCERTAINTY IN MODEL PREDICTIONS

Once a model has been built we will wish to use the model to make predictions. At this point we will want to know how good the model predictions are. A given model can be "wrong" for two reasons. There may be errors caused by incomplete and unreliable data. More difficult are errors in the basic modeling assumptions i.e., the conceptual model.

For the earth systems we model, the data available is always insufficient to completely characterize the system. As an alternative to obtaining one deterministic model with large error based on incomplete and unreliable data, one could view the data as determining a probability distribution on the set of possible models. We may be able to find many models in this distribution which fit the data. Incomplete and unreliable data increases the number of possible solutions. We can quantify some of this uncertainty by considering a range of predictions.

For an equivalent discontinuum model, there are several ways which we could choose different configurations of conductors to compare. The simplest is to use a series of configurations defined at the end of an annealing process. These configurations are easily available, but they will probably be very similar to each other. Another way to find different configurations is a Monte Carlo approach where we perform annealing several times, each time starting with a different initial configuration.

Errors caused by modeling assumptions are harder to define. We know that our model is a simplification, and only one of a large number of possible conceptual models. We have to decide if the model is appropriate for our purposes. The only way to approach this problem is through "peer review" or "confidence building". In the peer review, the approach to modeling is what is scrutinized. What assumptions were made? Do they make sense? What is the evidence supporting these assumptions? What data were used? What is the sensitivity of the calculation to poor assumptions or inaccuracies in data? Which are the parameters that control the result?

This is an iterative and a subjective process. Some of the assumptions cannot be checked easily for the simple reason that it would take infinite time to test all possible cases: i.e., one can prove a model is wrong, but you cannot prove it is right. We can only ask if the model is consistent with observations of all types that were made on the rock mass. Is the model consistent with the geologic observations, the geophysical measurements, the hydraulic measurements, etc.? For example, although a primary prediction may be aimed at flux, we can also check to see if the calculated head distribution are consistent with the observed head distribution. The approach to fracture flow modeling presented here tries to build in these observations a priori and thus is prepared to face peer review.

The main function of the model is to make predictions about the behavior of the system, so the model should be judged by its ability to accurately predict the system response. Thus, we wish to estimate how much error is associated with the model predictions. This "prediction error" is a lump measure of error caused by incomplete data and model assumptions. The calculation of prediction error is made by using the model to make a series of different predictions. For each prediction we obtain a prediction error by comparing the calculated result to the measured result. The root mean square of these errors is called the prediction error. Thus for this purpose, the model is a "black" prediction box and we validate the model by measuring how well it makes predictions. For example, we could use the model to predict the inflow into ten different boreholes for which the inflow had been measured. By comparing the measurements of inflow to the predicted values, we can calculate a prediction error. Now, we can use the model to predict the flow into an eleventh hole for which the inflow is not known. The prediction error then provides an estimate of how good this prediction is, i.e. how "validated" the model is.

This approach is straight forward. The more numerous and diverse types of predictions that can be included in the estimate of prediction error, the more stringently "validated" the model can be. If the model works well to predict flow under one boundary conditions, it may not predict well for a different set of boundary conditions. However, if it predicts well for two sets, then it is more likely to predict well under the third, even better for three, etc., etc.

A limitation of this approach is that one is unlikely to have such an extensive set of insitu tests to compare models against. Thus, one rarely has a good statistical sample of prediction errors. Further, we often must extend the use of the models to classes of physical conditions, phenomena or time scales which we have not been able to test in the field. For example, one may wish to use a model which worked well for a local flow problem to predict large scale regional flow, or we may want to use the flow model as the basis for a transport prediction. Here the prediction error we can calculate does not apply to the problem at hand. Although, there is an expectation that building a model for a given flow case is the first step in building a model for other flow conditions or transport, a model which works for in one case is not necessarily a valid model for radically different boundary conditions or different phenomena.

Finally, we are also concerned with about the robustness of our model: is it insensitive to small deviations from the assumptions? According to Huber (1981), slight deviations from the model assumptions should impair model performance only slightly, and larger deviations should not be catastrophic. Sensitivity analysis is one way to examine the robustness of the model.

The measures of uncertainty we use are prediction error and sensitivity studies. Both of these incorporate the effect of incomplete and unreliable data by using a range of possible solutions. Sensitivity analysis measures errors caused by basic assumptions in the model which are wrong, or change. And the prediction error is a measure which lumps together all sources of error.

9.1. Prediction Error

One way science has advanced is through the development of theories or models. A theory or model is useful if it successfully predicts behavior. The pure truth of the theory or model is not always relevant, for instance, there are two parallel theories often used to predict the behavior of light. One theory holds that light is a wave and the other theory holds that light is a particle. Physicists have known for some time that neither theory is strictly true. However, both models are useful, since under different conditions they do predict the behavior of light.

In the same sense, our hydrologic model is not a true representation of the fracture flow system. We are justified in using the model if it can accurately predict behavior. One measure of model goodness is the prediction error. We define the prediction error as the error between some independent quantity we predict using our model, and the measured value of that quantity.

To make a good prediction of a certain type of response, you need to use appropriate data to build the model. For example, if one built a model using pressure measurements, and tried to predict flow, the model may not predict accurately. Also, a prediction error estimated for one kind of response should not be used to estimate the prediction error for a different response.

The best possible way to evaluate prediction error is to make a prediction for a known quantity, that hasn't been used to build the model. Unfortunately, one usually needs all the available data to build a good model. One way around this problem is to set aside one data point, construct a model using the rest of the data, predict the value left out, and calculate a prediction error. If we do this for each data point in turn, we have a distribution of prediction errors we may use to estimate the prediction error for a model using all the data. This process is called cross-validation. Cross-validation may be extended to calculate multiple solutions for each data point we set aside. For example, in the MI study discussed in Section 7, we have steady state head values at 8 wells. If we leave out one well at a time and anneal, we can calculate a range of prediction errors for pressure measurements. We can use this range of errors to estimate the prediction error for the full model.

When multiple solutions are available, we may decide to use cross-validation to choose a good predictor. Suppose we had five annealing solutions used to predict each measured data point value we used in a cross-validation study. We would expect that using a mean or median of the five possible predicted values would give a lower prediction error than using a value from one annealing solution.

We may wish to minimize a function of the prediction error which expresses the loss we suffer when our predictions are off the true value. Often this loss is not a linear function of the error. One commonly used loss function is the squared error loss function,

$$L(y,\hat{y}) = (y - \hat{y})^{2.}$$

The observed value is y, and the predicted value is $\hat{y}$. For hydrologic data, we believe the percent difference is a good measure of the loss incurred. Hydrologic data often covers a few orders of magnitude, and it is most important that predictions should be of the same order. By using this loss function, we normalize all the data points so they can be compared. Otherwise, a small prediction error for a large value would count as much as an order of magnitude error for a small value.

$$L(y,\hat{y}) = \frac{|(y - \hat{y})|}{y} .$$

We use empirical evidence and our loss function to decide how to make a prediction given a range of solutions. The loss function for each well will be computed using the mean and the median of the solutions as predictors. The predictor which gives the lowest sum of loss functions will be used. This sum is a measure of the goodness of fit for the composite model.

In this way, we squeeze as much as we can from the data dry by using it to construct models, to chose a predictor, and to calculate an estimated prediction error.

9.2. Sensitivity Analysis

The reliability of our model depends on certain parameters, such as boundary conditions which change over time. We also need to consider the sensitivity of the model to change in these parameters. We have essentially three kinds of parameters: boundary conditions, the value of the conductance assigned to each conductor, and the geometry of the template. Given a range of possible models, we could change the boundary conditions and calculate new well test curves for the observation wells. A study of the sensitivity to boundary conditions can be done by trying different scenarios such as a free surface boundary or adding various constant head boundaries.

In the annealing examples using lattice models with constant conductance As for the conductances, any prediction of steady flow rate will be directly proportional to the conductance assigned to the elements, so the sensitivity of steady flow rate to conductance is known *a priori*

for constant conductance. We might want to consider the sensitivity of the model to the assumption of constant conductance. Our experience has lead us to believe that our model would be improved by using a range of conductances. Since we think we are capturing the mean behavior of the system, we could replace the constant values with a distribution of values. For example, we might believe that a certain region of the system had lower permeability than the rest. We might want to replace constant conductivity with two different conductances. The mean conductance would remain the same.

9.3. Example Calculation of Prediction Error from Stripa

The template model described in Section 6 was annealed using a synthetic cross-hole test which was produced based on a variety of data available for the SCV site. Synthetic data was used because there were no formal, well controlled cross-hole well tests available to use in annealing. This data consisted of ad hoc cross-hole tests performed by British Geologic Survey (BGS) and the record of heads in the boreholes as they responded to various openings and closing of holes (Holmes, 1989). The annealed model was used to produce a preliminary estimate of the flow into a new set of holes, the D-holes.

The synthetic data was based on three ad hoc cross-hole tests conducted by opening W2 and monitoring sections in N3, N4, and W1. Some zones did not respond and some responded very quickly. The test durations were too short to achieve steady-state conditions and the transient data was poorly controlled. However, these tests offer valuable information about the major hydrologic features in comparison to the single hole tests, because the scale of these cross-hole tests is much more representative of the overall size of the SCV site and the large hydrologic features.

Based on the transient results plus the record of hydraulic heads in the holes, the steady flow rate from W2 was extrapolated to estimate the steady-state flow rate of 10 (l/min). The corresponding estimation of steady state head in N3, N4, and W1 was found by extrapolating the head values in those holes during the period when W2 was opened for prolonged period of time.

Table 9.1 gives the heads that were calculated with the final configuration resulting from

annealing. We see that the annealing routine has managed to match the observed heads very well. At the end of the annealing process, we have determined several configurations of conductors within the zones, all of which result in matching the observed head data extremely well. The match has been achieved solely by arranging the conductors. As all the channels have the same conductance, k_A, any value of k_A will result in the same head distribution.

So, at this point we must calibrate the conductance of the channels such that the model will predict the correct value of flow from W2. To do this, we use the annealed model to calculate the flow from W2. Then we take the ratio of measured flow to calculated flow to find the conductance of the channels, which would produce the correct amount of flow into W2.

Now we rearrange the numerical model, closing the hole W2, adding the open D- holes and calculating the outflow from the D-holes. We repeat this for seven different configurations of the model. The resulting calculations of inflow to the D-holes are all between 8.8 and 9.1 (l/min). It is clear from these results that the prediction of inflow to the D-holes is largely governed by the measurement of flow from the W2 hole. In fact, the flow into the D-holes is directly proportional to the flow from W2. This indicates that the prediction of D-hole inflow is extremely sensitive to the measurement of flows and we suspect that this measurement is anomalous in that the transmissivity of W2 is much higher than the other holes.

One additional set of data is available to aid in the prediction of inflow to the D-holes. This data was also collected on an ad hoc basis, by BGS (Holmes, 1989), and consists of measurements of outflows from the other N- and W-holes ranging from 0.45 to 2.55 (l/min).

Now, we can use the final annealed configuration of channels with conductance, to calculate the inflow into each of these holes, Q_{iM}. To do this this we simply close W2 by making the nodes at W2 internal nodes, then sequentially open each of the other holes by assigning their nodes zero head. In each case, we calibrate the channel conductance in the same manner as previously described such that the model correctly predicts the measured flow. This results in five different predictions of channel conductance, which in turn results in five different predictions of D-hole inflow. These predictions are given below in Table 9.2. Therefore our best prediction of inflow

to the D-holes is 3.1 (l/min).

To calculate the error associated with this prediction we can also use the five different measurements of inflow. We anneal with the head data alone to get a channel configuration. Then we develop five different models by calculating channel conductance with only four of the inflows at a time. Thus, we average the conductances, k_i, from Table 9.2 leaving out one value (the ith value) at a time to get $<k_{io}>$. We then use this value to compute the flow into the hole we left out of the average. The root mean square of the differences between predicted and observed flux for each case is the estimated prediction error. These values are given below in Table 9.3.

In summary, our prediction of inflow to the D-holes has mean 3.1 (l/min) and a coefficient of variation (standard deviation divided by the mean) equal to about one. We estimate the error in this prediction to be about 4.6 (l/min). Actual measurement of inflow into the D-holes was about 1.7 (l/min) well within the prediction plus or minus the prediction error.

9.4. Example Cross Validation from the Migration Site

A cross-validation study was done with the MI data to choose a good predictor for head and estimate the prediction error. The prediction error for steady state head response is calculated using cross-validation. At the MI site, we have 8 wells and a drift. We use the steady state observed pressure response H_{obs}^i, at each well, i, under conditions of steady flow to the drift. We would like to know the prediction error associated with using our annealing model to predict the steady state head response at a ninth nearby well. We do the following:

(1)   Leave the steady state head value for well i out of the energy function.

(2)   Five annealing configurations were found starting from the five configurations with initial configurations having 60%, 70%, 80%, 90%, and 100% of the elements. We will refer to these solutions as cases 1 through case 5.

(3)   For each end configuration, $C_1^i \cdots C_5^i$, calculate a predicted steady state value for well i. These predicted head values are $H_1^i \cdots H_5^i$.

Table 9.1. Annealing results at the final iteration = 3749

Hole	Zone	Observed Heads	Predicted Heads
N2	B,B´,C	90	90
N3	A,B	80	79
	B´	none	65
	C	none	65
N4	B´	55	55
	C	none	83
	B	none	49
	A	none	49
W1	H_a,C	65	65
	H_b	none	65
	B´	none	65
	B	none	65

Table 9.2. Predictions of D-hole inflow based on annealing and
measured N- and W-hole inflows

Hole	Measured Flow (l/min)	Adjusted Flow (l/min)	k_i/k_A $\left[\dfrac{1/m}{m^3/S}\right]$	Predicted D-hole inflow (l/min)
N2	0.60	0.50	0.16	1.3
N3	0.45	0.37	0.12	0.6
N4	2.6	2.1	0.67	3.4
W1	1.3	1.1	0.35	1.3
W2	12.0	10.0	3.2	8.9
Mean	3.4	2.8	.89	3.1
Standard Deviation	4.9	4.1	1.3	3.1

(4)   Calculate the mean squared prediction error for well i:

$$PE^2(i) = \frac{\sum\limits_{j=1}^{5} |H_j^{-i} - H_{obs}^i|}{5}$$

The estimated prediction error is:

$$\hat{PE} = \left[\frac{\sum\limits_{i=1}^{8} PE(i)}{8}\right]$$

$\hat{PE}$ is then an estimate of the error involved in using one annealing model to predict the head response of any other well in the vicinity.

Similarly, we can compute $\hat{PE}$ for the mean or median predicted head response of the five solutions for each well left out. We used the loss function to compare the mean and median predicted value of the five solutions and found that the median was a slightly better predictor of steady state pressure at a given point on the grid. We then compared $\hat{PE}$ for predictions made using each solution independently with $\hat{PE}$ for predictions made by generating five solutions and using the median value as the prediction. The estimated prediction error found using a single solution was 4.3 m, and the estimated prediction error for using the median of five solutions was 3.3 m (Table 9.4). The prediction error for well 11 was very large, and tends to have a big effect on the prediction error (see Table 9.4). If we ignore well 11, the estimated prediction error using the median is 2.3 m. The estimated density of prediction error for the median of five solutions also shows the median is expected to give a lower prediction error. Therefore, we can make better predictions if we base them on multiple solutions instead of a single solution.

Table 9.3. Prediction error

Hole left out	$<k_{io}>$	Predicted Q_i (l/min)	Observed Q_i (l/min)	Error (l/min)
N2	1.1	3.4	.5	2.9
N3	1.1	3.4	.37	3.0
N4	.96	3.0	2.1	.90
W1	1.0	3.3	1.1	2.2
W2	.33	1.0	10.	9.
Estimated Prediction Error				4.6

Table 9.4. The observed steady state head values at each well and the predicted head values found using the median value for five annealing solutions. In each case the steady state head at the indicated well was left out of the energy function.

Well Left Out	Obs. Head	Median ($\hat{h}$) (m)	PE (i) (m)	PE (i,$\hat{h}$) (m)
4	9.97	6.64	3.8	3.3
5	10.95	5.95	5.0	5.0
6	10.22	7.72	4.0	2.5
7	0.64	0.988	3.2	0.3
8	3.37	0.96	2.5	2.4
9	8.07	9.99	2.1	1.9
10	4.0	5.07	2.8	1.1
11	1.04	11.37	11.1	10.3

10.0. CONCLUSIONS

This report represents a compilation of a significant amount of research which took place over several years and involved many people. Even so, it is by no means a complete reference for fracture characterization. We have attempted to follow a line of reasoning which could be applied at a fractured site to achieve a model for the hydrologic behavior of the system. The main point we have tried to emphasize is that interdisciplinary interaction is a critical part of maximizing understanding and reducing uncertainty. We hope we have described how the elements of different efforts can be linked and related to a final product.

Clearly, this is not a solved problem and there is much more to be done. Probably the most important progress will be made simply by trying to create predictive models for an increasing number of sites. Only in this way will we find out what works and what does not: hydrogeology is in many ways a heuristic science. We have a lot of experience in porous materials and as such we have theories that are useful for these cases. To know that the heuristics we develop for fractured rock are valid, we will simply have to try them out. If we are to build confidence in the theories we must also continue to work on developing a useful physical basis to explain the behavior we see.

11.0. REFERENCES

Aydin, A. and A. M. Johnson, 1978. Development of faults as zones of deformation bands and as slip surfaces in sandstone, *Pure and Applied Geophysics, 116,* 931-942.

Barker, J., 1988. A generalized radial-flow model for pumping tests in fractured rock, *Water Resources Research, 24,* (10) 1796-1804.

Barnsley, M., 1988. *Fractals Everywhere,* Academic Press, Inc. San Diego, CA.

Barton, C. C., T. A. Schutter, W. R. Page and J. K. Samuel, 1987. Computer generation of synthetic fracture networks for hydrologic-flow modeling, *Trans., American Geophysical Union, 68,* (44).

Beall, J. J. and W. T. Box, Jr., 1989. The nature of steam bearing fracture in the S. Geysers Reservoir, Proc. The Geysers - Three Decades of Achievement: A Window on the Future, Geothermal Resources Council 1989 Meeting, Geothermal Resources Council, Davis, Ca.

Berthé, D., P. Choukrone and P. Jegouzo, 1979. Orthogneiss, mylonite, and non coaxial deformation of granites: the example of the South American shear zone, *Journal of Structural Geology, 1,* 31-42.

Billaux, D., J. P. Chiles, K. Hestir and J. Long, 1989. Three-dimensional statistical modelling of a fractured rock mass -- an example from the Fanay-Augeres mine, *International Journal of Rock Mechanics and Mining Sciences and Geomechanics Abstracts, 26,* 281-299.

Bodvarsson, G. S., K. Pruess and M. J. Sullivan, 1985. Injection and energy recovery in fractured geothermal reservoirs, *Soc. Pet. Engr. Jour., 25,* (2) 303-312.

Bois, P., M. LaPorte, M. Lavergne and G. Thomas, 1972. Well to well seismic measurements, *Geophysics, 37,* 471-480.

Bossart, P., 1989 oral communication.

Bossart, P. and Martel, S. J., 1990. Hydrologic implications of ductile and brittle deformation in the Grimsel Crystalline, Upper Aare Valley, Switzerland, Nagra Internal Report 90-19.

Carlsten, S., O. Olsson, O. Persson and M. Sehlstedt, 1988. Site characterization and validation - monitoring of head in the Stripa mine during 1987, SKB Report 88-02, Stockholm, Sweden.

Carslaw, H. S. and J. C. Jaeger, 1946. *Conduction of Heat in Solids,* Clarendon Press, Oxford.

Carrera, J. and S. P. Neuman, 1986. Estimation of aquifer parameters under transient and steady state conditions: 2, *Water Resources Research, 22* (2).

Crampin, S., 1978. Seismic-wave propagation through a cracked solid: Polarization as a possible dilatancy diagnostic, *Geophys. J. Roy. Astron. Soc., 53,* 467-496.

Crampin, S., 1981. A review of wave motion in anisotropic and cracked elastic-media, *Wave Motion, 3* 343-391.

Crampin, S., 1984a. Effective anisotropic propagation through a cracked solid, in Crampin, S., R. G. Hipkin and E. M. Chesnokov (eds.), Proc. of the First International Workshop on Seismic Anisotropy, *Geophys. J. Roy. Astron. Soc., 76*, 135-145.

Crampin, S., 1984b. Anisotropy in exploration seismics, *First Break, 2*, 19-21.

Crampin, S., 1985. Evaluation of anisotropy by shear wave splitting, *Geophysics, 50*, (1) 142-152.

Daley, T. M., T. V. McEvilly and E. L. Majer, 1988a. Analysis of P- and S-wave data from the Salton Sea scientific drilling project, *Journal of Geophysical Research, 93*, (B11), 13025-13036.

Daley, T. M., T. V. McEvilly and E. L. Majer, 1988b. Multiply polarized shear-wave VSP's from the Cajon Pass drill-hole, *Geophys. Research Letters, 15*, (9) 1001-1004.

Davey, A. K. Karasaki, J. C. S. Long, M. Landsfeld, A. Mensch and S. J. Martel, 1990. Analysis of hydraulic data from the MI fracture zone at the Grimsel Rock Laboratory, Report No. NDC-15, LBL 27864, Lawrence Berkeley Laboratory, Berkeley, Ca.

Davey, A. and J. C. S. Long, 1990. An examination of geological problems in fracture network modeling, in preparation.

Delaney, P. T., D. D. Pollard, J. I. Ziony, E. H. McKee, 1986. Field relations between dikes and joints: emplacement processes and paleostress analysis, *Journal of Geophysical Research, 91*, 4920-4938.

Dershowitz, W. S., 1984. Rock Joint Systems, Ph.D. Dissertation, M. I. T., Cambridge, Mass., 764 pp.

Douma, J. (1988). Crack-induced anisotropy and its effect on vertical seismic profiling, No. 54, Geologica Ultraiectina, Mededelingen van het Instituut voor Aardwetenschappender Rijksuniversiteit te Utrecht, The Netherlands.

De Prat, G., H. Cinco-Ley and H. J. Ramey, Jr., 1981. Decline curve analysis using type curves for two-porosity systems, *Society of Petroleum Engineers Journal*, Society of Petroleum Engineers of AIME,

Devaney, A. J., 1984. Geophysical diffraction tomography, *IEEE Transactions on Geoscience and Remote Sensing*, GE-22 (1) 3-13.

Dines, K. A. and R. J. Lytle, 1979. Computerized geophysical tomography, *Proceedings of the IEEE, 67*, (7) 1065-1073.

Donath, F. A., 1961. Experimental study of shear failure in anisotropic rocks, *Geological Society of America Bulletin, 72*, 985-990.

Dyer, J. R., 1983. Jointing in sandstones, Arches National Park, Utah, Ph.D. Thesis, Stanford University, Stanford, California, 202 p.

Ehlig-Economides, C. A., 1979. Well Test Analysis for Wells Produced at a Constant Pressure, Ph.D. Thesis, Stanford University, Stanford, California.

Foxall, W. and T. V. McEvilly 1988. The microearthquake process as seen in high resolution with the Parkfield network, *Seismol. Res. L., 59*, (1).

Gelbke, C., 1988. Seismische durchschallungstomographie, NAGRA Technical Report 88-06.

Hajek, B., 1988. Cooling schedules for optimal annealing, *Mathematics of Operations Research, 13,* (2), 311-329.

Halfman, S. E., M. J. Lippmann, R. Zelwer and J. H. Howard, 1984. Geologic interpretation of geothermal fluid movement in Cerro Prieto Field, Baja California, Mexico, *The American Association of Petroleum Geologists Bulletin, 68, (1) 18-30.*

Hestir, K. and J. C. S. Long, 1990. Analytical expressions for the permeability of random two-dimensional Poisson fracture networks based on regular lattice percolation and equivalent media theories, *Journal of Geophysical Research,* (in press).

Huber, P. J., 1981. *Robust Statistics,* John Wiley and Sons, New York, NY, 308 p.

Hudson, J. A. and P. R. La Pointe, 1980. Printed circuits for studying rock mass permeability, *International Journal of Rock Mechanics and Mining Science and Geomechanics Abstracts, 17,* 297-301.

Huesman, R. H., G. T. Gullberg, W. L. Greenberg, T. F. Budinger, 1977. Users manual: Donner algorithms for reconstruction tomography, Lawrence Berkeley Laboratory, University of California, Report PUB-214, 285 p.

Ingraffea, A. R., 1981. Mixed-mode fracture initiation in Indiana limestone and Westerly granite, U. S. Symposium on Rock Mechanics, 22nd, Massachusetts Institute of Technology, Proceedings, 186-191.

Ito, H., J. Devilbiliss and A. Nur, 1979. Compressional and shear waves in saturated rock during water-stream transition, Report, Stanford University, California, U.S.A.

Johnson, L. R. and J. E. Peterson, 1986. Analysis of ultrasonic velocities in Kouros, LBL Report LBID-1175.

Karasaki, K., 1986. Well Test Analysis in Fractured Media, Ph.D. Thesis, Dept. of Materials Science and Mineral Engineering, University of California, Berkeley.

Karasaki, K., 1989. Prematurely terminated slug tests, paper submitted to *Water Resources Research Journal.*

Kirkpatrick, S., D. C. Gelatt and M. P. Vecchi, 1983. Optimization by simulated annealing, *Science, 220,* 671-680.

Keusen, H. R., J. Ganguin, P. Shuler, M. Buletti, 1989. Grimsel Test Site Geology, Nagra Technical Report 87-14E, Nagra, Baden, Switzerland, 120 p.

Kucuk, F. and W. E. Brigham, 1979. Transient flow in elliptical systems, *Soc. Pet. Eng. J.,* 401-410.

Laky, C., M. J. Lippmann, G. S. Bodvarsson, M. Retana, G. Cuellar, 1989. Hydrogeologic model of the Ahuachapan Geothermal Field, El Salvador, paper presented at the Fourteenth Workshop on Geothermal Reservoir Engineering, Stanford, Ca, Lawrence Berkeley Laboratory Report No 26869.

Lawn, B. R. and T. R. Wilshaw, 1975. *Fracture of Brittle Solids,* New York, Cambridge University Press, 204 p.

Leary, P. C. and T. L. Henyey, 1985. Anisotropy and fracture zones about a geothermal well from P-wave velocity profiles, *Geophysics, 50,* (1) 25-36.

Lisle, R. J., 1989. Paleostress analysis from sheared dike sets, *Geological Society of America Bulletin, 101,* 968-972.

Long, J. C. S., J. S. Remer, C. R. Wilson and P. A. Witherspoon, 1982. Porous media equivalents for networks of discontinuous fractures, *Water Resources Journal, 18,* (3), 645-658.

Long, J. C. S., 1983. Investigation of Equivalent Porous Medium Permeability in Networks of Discontinuous Fractures, Ph.D. Thesis, University of California, Berkeley.

Long, J. C. S. and P. A. Witherspoon, 1985. The relationship of the degree of interconnection to permeability in fracture networks, *Journal of Geophysical Research, 90,* (B4) 3087-3097.

Long, J. C. S., K. Karasaki, A. Davey, J. E. Peterson, M. Landsfeld, J. Kemeny and S. J. Martel, 1989. Preliminary Prediction of Inflow into the D-Holes at the Stripa Mine, Lawrence Berkeley Laboratory Report 27182, in preparation.

Majer, E. L., L. R. Myer, J. E. Peterson, Jr., K. Karasaki, J. C. S. Long, Stephen J. Martel, P. Blümling and S. Vomvoris, 1990. Joint seismic, hydrogeological, and geomechanical investigations of a fracture zone in the Grimsel Rock Laboratory, Switzerland, Report No. NDC-14, LBL 27913, Lawrence Berkeley Laboratory, Berkeley, Ca.

Majer, E. L., T. V. McEvilly, F. S. Eastwood and L. R. Myer, 1988a. Fracture detection using P- and S-wave VSP's at The Geysers Geothermal Field, *Geophysics, 53,* (1) 76-84.

Majer, E. L., J. E. Peterson, T. V. McEvilly, L. R. Myer, P. Blumling and G. Sattel, 1988b. VSP/tomographic imaging for fracture detection and characterization, *Earthquake Notes, 59,* (1) 41.

Majer, E. L., J. E. Peterson, T. V. McEvilly, L. R. Myer, P. Blumling and G. Sattel, 1988c. Cross-hole seismic measurements for fracture characterization, *EOS,* Abstract AGU Annual Fall Meeting, 69 (64).

Mandelbrot, B. B., 1982. *The Fractal Geometry of Nature,* W. H. Freeman and Company, New York, 468 pp.

Martel, S. J., D. D. Pollard and P. Segall, 1988. Development of simple strike-slip fault zones, Mount Abbot quadrangle, Sierra Nevada, California, *Geol. Soc. Am. Bulletin, 100,* 1451-1465.

Martel, S. J., 1989. Formation of segmented strike-slip fault zones, Mount Abbot quadrangle, California, in D. Schwartz, (ed.), Proceedings of U.S. Geological Survey Workshop on Fault Segmentation and Controls of Rupture Initiation and Termination, U.S. Geological Survey Open-File Report, in press.

Martel, S. J., 1990. Formation of compound strike-slip fault zones, Mount Abbot quadrangle, Sierra Nevada, California, *Journal of Structural Geology, 12,* (7) 869-882.

Martel, S. J. and J. E. Peterson, Jr., 1990. Fracture-zone structure at the US/BK site, Grimsel Rock Laboratory, Switzerland, Earth Sciences Division Annual Report, Lawrence Berkeley Laboratory Report No. LBL-26362, 89-92.

Martin, C. D., C. C. Davison and E. T. Kozak, 1990. Characterizing normal stiffness and hydraulic conductivity of a major shear zone in granite, *Rock Joints,* N. Barton and O. Stephansson, eds., Proceedings of the International Symposium on rock Joints, A. A. Balkema, Rotterdam.

Mersereau, R. M. and A. Oppenheim, 1974. Digital reconstruction of multidimensional signals from their projections, *Proceedings of the IEEE, 62,* (10) 1319-1338.

Metropolis, N., A. Rosenbluth, M. Rosenbluth, A. Teller and M. Teller, 1953. Equation of state calculations by fast computing machines, *J. Chemical Phys, 21*. 1087-1092.

Mochizuki, S., 1982. Attenuation in partially saturated rock, *Journal of Geophysical Research, 87,* (B10) 8598-8604.

Muehlberger, W. R., 1986. Different slip senses of major faults during different orogenies: The rule?, in Proceedings, International Conference on Basement Tectonics, 6th, Sante Fe, September, 1985, Salt Lake City, Utah, International Basement Tectonics Association, p. 76-81.

Niva, B. and O. Olsson, 1987. FLG Radar Crosshole Tomography Results from Phase 1, Nagra Internal Report 88-30, Nagra, Baden, Switzerland, April.

Niva, B. and O. Olsson, 1988a. FLG Radar Crosshole Tomography Results from Phase 2, Nagra Internal Report 88-31, Nagra, Baden, Switzerland, January.

Niva, B. and O. Olsson, 1988b. FLG Radar Crosshole Tomography Results from Phase 3, Nagra Internal Report 88-57, Nagra, Baden, Switzerland, April.

Orbach, R., 1986. Dynamics of fractal networks, *Science, 231,* 814-819.

Olsson, O., J. H. Black, J. E. Gale and D. C. Holmes, 1988a. Site Characterization and Validation, Stage 2 - Preliminary Predictions, Swedish Geological Co. Report ID No. 88.

Olsson, O., J. Eriksson, L. Falk and E. Sandberg, 1988b. Site Characterization and Validation - Borehole Radar Investigations, Stage I, SKB Report 88-03, Stockholm, Sweden.

Olson, J. and D. D. Pollard, 1989. Inferring paleostresses from natural fracture patterns: A new method, *Geology, 17,* 345-348.

Orbach, R., 1986. Dynamics of fractal networks, *Science, 231,* 814-819.

Peng, S. and A. M. Johnson, 1972. Crack growth and faulting in cylindrical specimens of Chelmsford Granite, *International Journal of Rock Mechanics and Mining Science and Geomechanics Abstracts, 9,* 37-86.

Peterson, J. E. Jr., 1986. The Application of Algebraic Reconstruction Techniques to Geophysical Problems, Ph.D. Thesis, University of California, Berkeley, 188 p.

Peterson, J., 1989. Personal communication.

Pike, G. E. and C. H. Seager, 1974. Percolation and conductivity: A computer study, *Physical Review, B, 10* (4), 1421-1446.

Pollard, D. D. and P. Segall, 1987. Theoretical displacements and stresses near fractures in rock: With applications to faults, joints, veins, dikes, and solution surfaces, in B. K. Atkinson (ed.), *Fracture Mechanics of Rock,* Academic Press, San Diego, 534 p.

Press, W. H., B. P. Flannery, S. A. Teukolsky and W. T. Vetterling, 1986. *Numerical Recipes,* Cambridge University Press.

Pyrak-Nolte, L. J., L. R. Myer and N. G. W. Cook, 1990. Anisotropy in seismic velocities and amplitudes from multiple parallel fractures, *J. Geophys. Res.,* (in press).

Ramsay, J., 1967. *Folding and Fracturing of Rocks,* McGraw-Hill, San Francisco, 568 p.

Robertson, J. D. and D. A. Fisher, 1988. Coupled seismic trace attributes, *The Leading Edge, 7* (6) 22-26.

Robinson, P., 1984. Connectivity, Flow and Transport in Network Models of Fractured Media, Ph.D. Thesis, St. Catherine's College, Oxford.

Schoenberg, M., 1980. Elastic wave behavior across linear slip interfaces, *J. Acoust. Soc. Am., 68,* (5) 1516-1521.

Schoenberg, M., 1983. Reflection of elastic waves from periodically stratified media with interfacial slip, *Geophys. Prosp., 31,* 265-292.

Segall, P. and D. D. Pollard, 1983. Nucleation and growth of strike slip faults in granite, *J. Geophys. Res., 88,* 555-568.

Segall, P. and C. Simpson, 1986. Nucleation of ductile shear zones on dilatant fractures, *Geology, 14,* 56-59.

Sen, P. N., C. Scala and M. H. Cohen, 1981. A self similar model for sedimentary rocks with application to the dielectric constant of fused glass beads, *Geophysics, 46,* (5) 781-795.

Sibson, R. H., 1977. Fault rocks and fault mechanisms, *Journal of the Geological Society of London, 133,* 191-213.

Sibson, R. H., 1981. Fluid flow accompanying faulting: Field evidence and models, in D. W. Simpson and P. G. Richards (eds.), *Earthquake Prediction,* AGU, Washington, D. C., 593-603.

Sibson, R. H., 1986. Brecciation processes in fault zones: Inferences from earthquake rupturing, *PAGEOPH, 124,* 159-175.

Slaney, M. and A. C. Kak, 1985. Imaging with Diffraction Tomography. School of Electrical Engineering, Purdue University, Report TR-EE 85-5, 211 p.

Smith, R. B., 1975. Unified theory of the onset of folding, boudinage, and mullion structure, *Geological Society of America Bulletin, 86,* 1601-1609.

Smith, R. B., 1977. Formation of folds, boudinage and mullions in non-Newtonian materials, *Geological Society of America Bulletin, 88,* 312-320.

Stauffer, D., 1985. *Introduction to Percolation Theory,* Taylor and Francis Ltd, London, England, p. 52.

Stewart, R. R., R. M. Turpening and M. N. Toksoz, 1981. Study of a subsurface fracture zone by vertical seismic profiling, *Geophysical Research Letters, 8,* 1132-1135.

SKB (Swedish Nuclear Fuel an Waste Mangement Co.), 1987. Program for the Stripa Project Phase 3 1986-1991, SKB report 87-09, Stockholm, Sweden.

Swanson, M. T., 1988. Pseudotachylyte-bearing strike-slip duplex structures in the Fort Foster Brittle Zone, S. Maine, *Journal of Structural Geology, 10,* 813-828.

Sylvester, A. G., 1988. Strike-slip faults, *Geological Society of America Bulletin, 100,* 1666-1703.

Tarantola, A., 1987. *Inverse Problem Theory,* Elsevier Science Publishing Company Inc., New York, N. Y.

Telford, W. M., L. P. Geldart, R. E. Sheriff and D. A. Keys, 1976. *Applied Geophysics*, Cambridge University Press, Cambridge, 860 p.

Tura, A., 1990. Acoustic and Elastic Diffraction Tomography and its Application to Fracture Detection, Ph.D. Dissertation, University of California, Berkeley.

Terzaghi, R. D., 1965. Sources of error in joint surveys, *Geotechnique, 15,* 287-304.

van Everdingen, A. F. and W. Hurst, 1949. The application of the Laplace Transformation to flow problems in reservers, *Trans., AIME, 186,* 305-324.

Wallace, R. E. and H. T. Morris, 1986. Characteristics of faults and shear zones in deep mines, *Pure and Applied Geophysics, 124,* 107-125.

Wyss, E., 1988. Kurzbericht Zu Den Ersten Hydrogelogischen Untersuchungen Im Rahmen Des Versuches FRI, 616, NAGRA, Internal Data Report.

Wu, R. and M. N. Toksoz, 1987. Diffraction tomography and multisource holography applied to seismic imaging, *Geophysics, 52,* (1) 11-25.

Zallen, R., 1983. *Physics of Amorphous Solids,* Wiley, New York, 135-204.

Zhou, Q. and F. Morrison, 1988. Cross borehole audio frequency electromagnetic tomography, The Ninth Workshop on Electromagnetic Induction in the Earth and Moon, USSR, 24-31 October.